"Multi-dimensional radio channel models for indoor distributed communications"

Vinogradov, Evgenii

Abstract

Single- and multi-antenna indoor systems have been designed and used for various applications for some years now, but still there is a room for improvements. Channel modeling is one of the aspects where researchers and engineers face many challenges. Since indoor environments consist of many scatterers, mobility of the nodes introduces non-stationarity in the propagation channel. To enable successful design of communication systems, such an important issue must be taken into account. With that perspective, dedicated measurement campaigns and realistic radio propagation channel models are required in order to exploit fully the improvement potential. The main contributions and findings of this thesis can be summarized as follows: - Three measurement campaigns of indoor-to-indoor radio propagation channels were conducted at 3.8 GHz. - The stationarity period duration varies between 0.8-1.5 s for different investigated cases depending on the environment. - It turns out that small-scale f...

Document type : *Thèse (Dissertation)*

UNIVESITÉ CATHOLIQUE DE LOUVAIN
ECOLE POLYTECHNIQUE DE LOUVAIN
ICTEAM ELECTRICAL ENGINEERING

MULTI-DIMENSIONAL RADIO CHANNEL MODELS FOR DISTRIBUTED COMMUNICATION

PAR
EVGENII VINOGRADOV

Thèse présentée en vue de l'obtention du grade de docteur en sciences de l'ingénieur

Composition du Jury

Prof. Claude Oestges (Supervisor)	UCL, Belgium
Prof. Wout Joseph (Supervisor)	UGent, Belgium
Prof. Luc Vandendorpe	UCL, Belgium
Prof. Martine Liénard	Université de Lille I, France
Prof. David Bol (Chair)	UCL, Belgium
Prof. Jérôme Louveaux (Secretary)	UCL, Belgium

Louvain-la-Neuve
2017

Acknowledgments

Four years ago I enthusiastically started a long journey. It is one of the best decisions I have ever made. Here, in Belgium, I have met so many amazing people who transfused their enthusiasm and passion for research to me. In the following, I will attempt to thank all of them for their kindness and support. I take this opportunity to express my gratitude to as many individuals as possible who have been most helpful in the successful completion of this thesis, I wish very much to be excused by those whose names I may fail to present within the following few paragraphs.

First of all, I would like to express my sincere gratitude to my promoters Prof. Claude Oestges and Prof. Wout Joseph for their inspirational ideas and continuous support throughout my PhD study and related research. Claude, thank you for your patience, leading by example, profound knowledge in the vast field of wireless communication in particular channel modeling and always having the time for discussions. I am extremely thankful and indebted to Wout for sharing his creative ideas, constant encouragement and valuable guidance. His view of the research helped me to enhance my thesis and skills. I could not have imagined having better advisors and mentors for my PhD. I would also like to thank them for the efforts they put into finding financial support that made this thesis possible.

I would like to sincerely thank the thesis jury, Prof. David Bol, Prof. Luc Vandendorpe, Prof. Martine Liénard, and Prof. Jérôme Louveaux for accepting to be member of this jury. I also thank them for their time, valuable advices, comments and corrections that they proposed during my private defense. Their precious remarks and advices were greatly useful to improve the quality of this thesis.

Through it all I would like to express my gratitude to my colleagues (Olivier, Babak, Alberto, Yang, Quentin, Husnain, Pierre-Antoine, Brecht, Mohieddine, Gloria) for their help and for always being there. I should mention many fruitful discussions in an informal setting with Sergei, Hans-Ulrich, Dmitry and Carlos. They helped to develop my research as well as my personality. I would like to thank Nizabat, Ferran and Loïc for interesting conversations and sharing opinions on various topics which have enriched my mind with knowledge. I am grateful to Aliou for his help during the measurement campaigns.

Many thanks go to the technical and administrative staff at the ICTEAM institute, especially to David Spôte for his excellent mechanical solutions, Pascal Simon for his logistical assistance, Brigitte Dupont and Francois Hubin for helping me out with computer matters, Isabelle Dargent and Marie-Christine for their administrative help and prompt responses.

Finally, none of this would have been possible without the love, continuous en-

couragement, and unwavering support of my family: my parents, my sister, all my uncles, aunts, grandparents and cousins. If I mention all of you this thesis will be too long, but I will be eternally grateful, for everything you have done for me since my childhood. Additionally, I am grateful to Evgenii Sergeevitch and Zoya Mikhailovna for cultivating my passion to radio and programming since my early age.

I would not have finished this thesis without the support, encouragement and help of my wife Arianna. Thank you for always being there, for your unconditional love, care and support, but in the future you will need a lot of patience for being married with a researcher.

Abstract

Single- and multi-antenna indoor systems have been designed and used for various applications for some years now, but still there is a room for improvements. Channel modeling is one of the aspects where researchers and engineers face many challenges.

Since indoor environments consist of many scatterers, mobility of the nodes introduces non-stationarity in the propagation channel. To enable successful design of communication systems, such an important issue must be taken into account. With that perspective, dedicated measurement campaigns and realistic radio propagation channel models are required in order to exploit fully the improvement potential.

The main contributions and findings of this thesis can be summarized as follows:

- Three measurement campaigns of indoor-to-indoor radio propagation channels were conducted at 3.8 GHz.
- The stationarity period duration varies between $0.8 - 1.5$ s for different investigated cases depending on the environment.
- It turns out that small-scale fading within one stationarity period follows a weighted combination of different known distributions. This mixed type of fading can be described by a Second Order Scattering Fading (SOSF) distribution which reflects any combination of Rician, Rayleigh, and double-Rayleigh fading.
- New double-ring geometry-based reference and simulation models for narrowband single- and multi-antenna SOSF channels are proposed. Next, second order-statistics of these channels are derived and analyzed.
- New model for temporal evolution of angular statistics is proposed.
- It is shown that a Hidden Markov Model based approach can be used to reproduce time-variant statistics of small-scale fading. It can be parameterized from measurements: empirical estimation and transition matrices were extracted for the three investigated environments. We observed that predominant fading mechanism can be described by a mixture of Rayleigh and Double Rayleigh distributions. Distributions of the parameter α (corresponding to the impact of Double Rayleigh fading) for the Rayleigh-double Rayleigh and Δ (joint impact of the Line-of-Sight (LOS) term and Double Rayleigh fading) for the double-Rayleigh-LOS subsets can be well approximated by the Beta distribution; the K-Factor (derived from parameter β of SOSF distribution) of Rician fading is Extreme Value distributed.

- A methodology of time-variant power delay profiles has been designed in the room-to-room dynamic scenario.
- Normal distribution with zero-mean and the variance extracted from measurements can be used for mean large-scale fading modeling and dynamic large-scale fading follows a t-location scale distribution.

Contents

List of Figures

List of Tables

Acronyms

AFD Average Fade Duration

AoA Angle of Arrival

AoD Angle of Departure

APS Angular Power Spectrum

BER Bit Error Rate

CDF Cumulative Distribution Function

CKA Clock Keep Alive

CLT Central Limit Theorem

CMD Correlation Matrix Distance

DoA Direction of Arrival

DoD Direction of Departure

DR Double Rayleigh

DRLOS Double Rayleigh and Line-of-Sight

F-to-M Fixed-to-Mobile

H Homogeneous

IR Impulse Response

ISIS Initialization and Search Improved SAGE

LCR Level Crossing Rate

LOS Line-of-Sight

LS fading Large-Scale Fading

LSF Local Scattering Function

M-to-M Mobile-to-Mobile

MIMO Multiple-Input Multiple-Output

MPC MultiPath Component

MS Mobile Station

NLOS Non-Line-of-Sight

PDF Probability Density Function

PDP Power Delay Profile

PN Pseudo Noise

RDR Rayleigh - Double Rayleigh

REM Room Electromagnetics

RF Radio Frequency

RMS Root Mean Square

RS Radio Signal

Rx receiver

SAGE Space-Alternating Generalized Expectation-maximization

SIMO Single-Input Multiple-Output

SISO Single-Input Single-Output

SOSF Second Order Scattering Fading

SS fading Small-Scale Fading

TF Transfer Function

TvM Tikhonov-von Mises

Tx transmitter

UCA Uniform Circular Antenna

US Uncorrelated Scattering

WSS Wide Sense Stationarity

Chapter 1

Introduction to Wireless Channel Modeling

The demand for flexible mobile multimedia services continues to grow. The recently published white paper [1] reports that in 2015 the monthly mobile traffic was 3.7 Exabytes and Cisco forecasts 30.6 Exabytes per month of mobile data traffic by 2020. It was pointed out that traditional cellular solutions are coming under the increasing pressure from various indoor communication systems: much mobile data activity takes place within users homes and/or offices. For users with fixed broadband and Wi-Fi access points at home, or for users served by operator-owned femtocells and picocells, a sizable proportion of traffic generated by mobile and portable devices is offloaded from the mobile network onto the fixed network. In 2015, users generated 51 percent of traffic indoor and the increase of this impact became a recognized trend (see Figure 1.1). Many other growing trends such as home and office security and automation, smart metering and utilities, maintenance, building automation, automotive, health-care and consumer electronics were also mentioned.

An important factor is the emergence of wearable devices, a category with high growth potential. Wearable devices, as the name suggests, are devices that can be

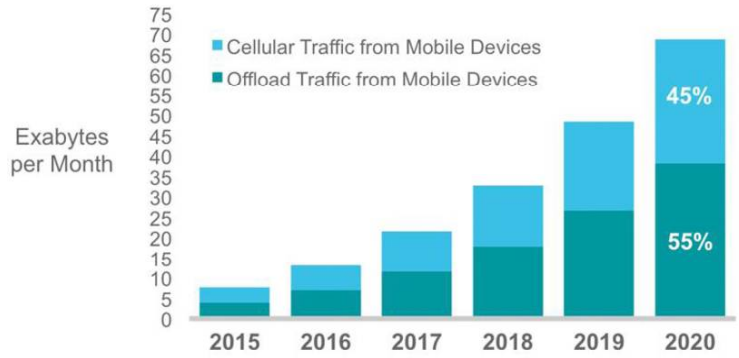

Figure 1.1: Cellular offload forecast [1]

worn on a person and have the capability to connect and communicate to the network either directly through embedded cellular connectivity or through another device using different communication technologies. These devices come in various shapes and forms, ranging from smart watches, smart glasses, heads-up displays, health and fitness trackers, health monitors, wearable scanners and navigation devices, smart clothing, etc. Technical development is being combined with fashion to match personal styles, especially in the consumer electronics segment, along with network improvements and the growth of applications, such as location-based services and augmented reality. Although there have been vast technological improvements to make wearables possible as a significant device category, wide-scale availability of embedded cellular connectivity still has some barriers to overcome for some applications such as technology limitations, regulatory constraints, and health concerns.

In other words, wireless technologies have become closer to users, entered their homes and offices. Many methods were introduced to make this possible. Underlying radio channels influence the performance of all of these schemes. As one can notice, the technologies and applications are becoming more and more complex. Conventionally, stationary Rayleigh fading between the nodes was assumed. However, it is not the case in indoor peer-to-peer channels. Here, we observe a strong dependence on the nodes' mobility and on the scattering scenario [3]. For this reason, the non-stationary radio channel must be measured and modeled, as time-variant fading statistics may be exploited by algorithms used in the network, for example by incentive mechanisms based on repeated games that force nodes to help disadvantaged ones in view of a future exchange of roles, along the lines of [4].

Naturally, indoor radio propagation channels have been investigated in the past. Deterministic approaches such as ray tracing methods are used in [5, 6, 7, 8, 9, 10] to predict the characteristics of the radio channels in indoor environments. Although good agreement can be obtained with such numerical approaches, high computational cost makes them less attractive. This cost increases as well when the room dimensions and/or frequency increase. Indoor wireless channel modeling has been empirically addressed in [11, 12, 13]. These studies investigated indoor path loss and/or fading models around 1.8 and 5.2 GHz. In particular, path-loss predictions rely on the simple one-slope log-distance model.

Empirical path loss models for in-room, room-to-corridor, and room-to-room scenarios have also been investigated [14]. The one-slope log-distance, dual-slope log-distance and attenuation factor model are used to estimate the path loss in in-room, room-to-corridor, and room-to-room scenarios, respectively. In [15], various properties of indoor peer-to-peer channels have been analyzed, but for static nodes only: fading was modeled for single-antenna links by a generalized gamma distribution.

It was shown in [16] that non-stationarity is an important issue for indoor channels. Hence, the effects brought by nodes' mobility must be considered in the channel modeling. Some previous works e.g., [17, 18] have modeled indoor channels for so-called nomadic scenarios (fixed nodes, moving obstacles). In [17] the shadowing, K-factor, and delay spread are found to be correlated lognormal variables, whereas in [18] fading is found to be SOSF (Second Order Scattering Fading [19]) distributed. Single mobile links between the nodes located in the same room (or adjacent rooms) under LOS and non-LOS conditions were investigated in [20]: fading was found to be Weibull distributed. In [3], peer-to-peer channels were empirically modeled in

a typical cubicle-style office environment. The same environment was also used in [21] to investigate the multi-user separation in dual-link multiple-input and multiple-output (MIMO) indoor scenarios. Dynamic models of indoor wireless channels were proposed in [22, 3], where the motion of communication nodes and obstacles (such as people) is taken into account. Whereas models in [18, 3] are narrowband, the method in [22] predicts the time-varying PDP as a weighted sum of cluster functions.

This chapter provides an overview of basic propagation phenomena, different approaches to model the wireless channel and existing channel models relevant to a single wireless link as well as Multiple-Input Multiple-Output (MIMO) channels. The remainder of this Chapter is structured as follows: Section 1.1 describes the basic aspects of propagation. Large- and small-scale fading mechanisms are presented in Section 1.2. The second order scattering fading distribution is described in Section 1.3. Reference models for narrowband fading channels are presented in Sections 1.4 and 1.5 for single- and double mobile scenarios, respectively. Section 1.6 is dedicated to the wideband channel modeling and several popular simulation models of fast fading are presented in Section 1.7

1.1 Wireless Channel Modeling

In wireless communication networks, the propagation channel is the medium between the transmitter (Tx) and the receiver (Rx). It is obvious that its properties influence the performance of wireless networks. Next generation wireless networks design (i.e., algorithms development) is impossible without the knowledge of wireless channel. The behavior of the channel can significantly change with choice of the nodes architecture, Radio Signal (RS) specificities etc. Consequently, radio channel characterization and modeling in such innovative architectures becomes crucial to evaluate the achievable network performance.

1.1.1 Aspects of Multipath Propagation

The Tx radiates a signal in the form of electromagnetic waves in several directions. Waves interact with the surrounding environment through various propagation phenomena, before it reaches the Rx. As illustrated in Figure 1.2, different phenomena such as specular reflections, diffraction, scattering, wave-guiding, penetration or any combination of these can be involved in propagation [23]. Therefore, multiple realizations of the transmitted signal, often termed as MultiPath Component (MPC) arrive to the Rx with different amplitudes, delays and directions. The instantaneous Impulse Response (IR) of a wireless propagation channel can be written as

$$h(t,\tau) = \sum_{i=1}^{N} \alpha_i \delta(t - \tau_i), \tag{1.1}$$

where δ is the Dirac delta function, N is the number of MPCs, and $\alpha_i(t)$are complex amplitudes at respective delays τ_i. Resulting IR is the linear coherent superposition of all MPCs, which can be constructive or destructive depending upon their respective random phases. So that, fading caused by IR may also deteriorate considerably the quality of the received signal. If the IR has an extent in the delay domain, then different

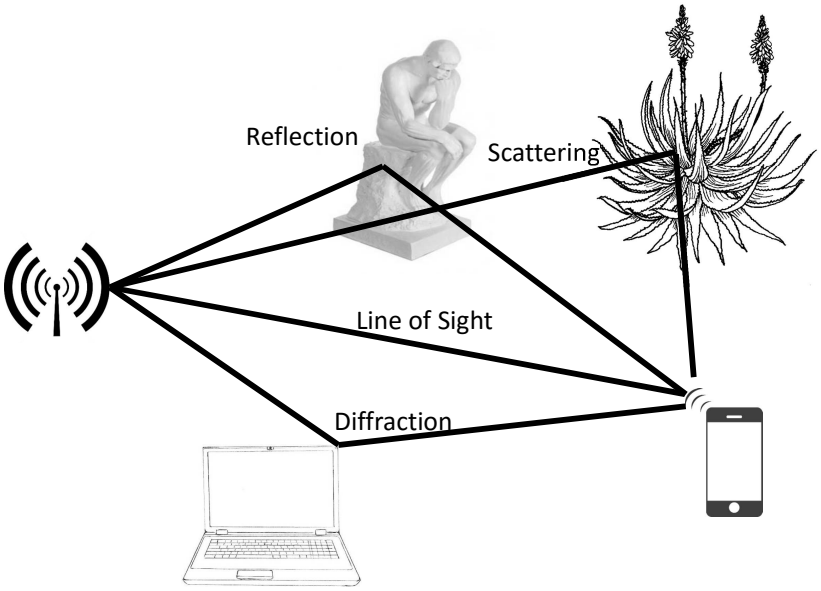

Figure 1.2: An illustration of multipath propagation

frequency components of the transmitted signal fade differently. This fading is said to be frequency selective. Furthermore, due to movements of the Tx and/or the Rx and scatterers present in the vicinity, the propagation channel varies over time. Finally, the propagation channel is time selective if each MPC experiences a unique frequency shift.

For a given link between the Tx and the Rx, the propagation channel is usually described by its IR, $h(t, \tau)$ [23, 24]. It links the input signal at the Tx with the output signal at the Rx through the following well known relation,

$$y(t) = h(t, \tau) * x(t) + n(t), \tag{1.2}$$

where $x(t)$ and $y(t)$ are the transmitted and the received signal respectively, $n(t)$ denotes the additive noise at the Rx, and the operator $*$ represents the convolution operator. Figure 1.3 shows an example of measured channel IRs where several propagation paths to generate IRs can be noticed. Note that each propagation path is influenced by the following:

- the Tx antenna in the direction of transmission of the propagation path
- the radio channel on the propagation path
- the Rx antenna in the direction of arrival of the propagation path.

A block diagram of the measurement system illustrating the wireless propagation channel with the Tx and Rx antennas and associated Radio Frequency (RF) cables is shown in Figure 1.4. Thus derived channel models will be very specific to antennas utilized during measurements.

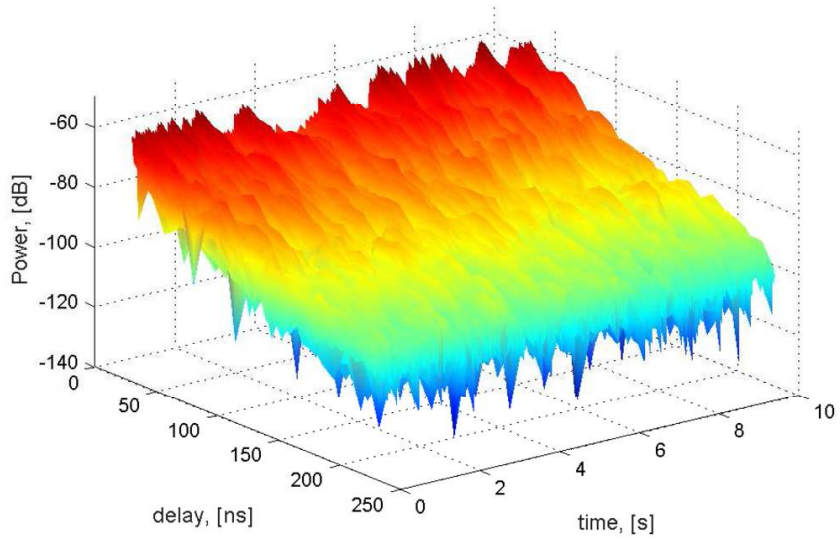

Figure 1.3: An example of measured channel IR

Similarly, the frequency-dependent transfer function can be described by applying a Fourier transform on (1.2),

$$Y(f) = H(t, f)X(f) + N(f), \tag{1.3}$$

where Y, H, X and N are the Fourier transforms of y, h, x and n, respectively.

1.1.2 Narrowband and Wideband Channels

Wireless channels are generally categorized into narrowband and wideband channels based on the relationship between the transmission bandwidth and the coherence bandwidth [24]. Narrowband channels have a small bandwidth (transmission bandwidth is less than the coherence bandwidth) such that the Rx is not able to resolve multiple MPCs. The frequency response of such channels is invariant over the transmission bandwidth, therefore named as frequency flat fading channels. The IR of narrowband channels can be described by a single tap, i.e., a delta function with a time-varying attenuation

$$h(t, \tau) = \alpha(t)\delta(\tau) \tag{1.4}$$

In contrast, in wideband channels the transmission bandwidth larger than the coherence bandwidth, this means that a frequency-dependent channel behavior can be distinguished. The frequency response of such channels varies over the transmission bandwidth, therefore also said to be frequency-selective fading channels. Moreover, more precise temporal resolution is peculiar to such channels and the Rx has the ability to resolve the MPCs based on their respective delay. The directional properties (for

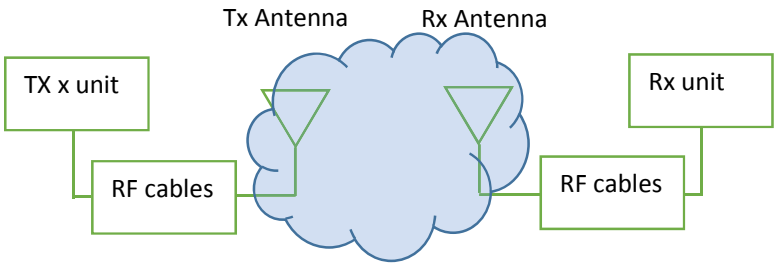

Figure 1.4: Block diagram of the measurement system

both types of channels) at the Tx and at the Rx define the autocorrelation function of the IR when a mobile receiver moves in space. If multiple antennas are used at both sides, the correlation is defined by directional characteristics of the channel.

1.1.3 Multidimensional Radio Propagation Channels

Double-directional SISO Radio Propagation Channels

In a three-dimensional environment, the directional IR of the radio propagation channel can be expressed as the linear (coherent) time-variant superposition of N multipath components, such that [23]

$$h(\tau; t; \Omega_{Tx}; \Omega_{Rx}) = \sum_{n=0}^{N} e^{j2\pi f_d^n t} g_{Rx}(\Omega_{Rx,n}) a_n g_{Tx}(\Omega_{Tx,n}) \delta(\tau - \tau_n), \qquad (1.5)$$

where $\tau_n, a_n, f_d, \Omega_{Tx,n}$ and $\Omega_{Rx,n}$ denote the time-variant delay, complex amplitude, Doppler shift, Direction of Departure (DoD) and Direction of Arrival (DoA) of the $n-$th multipath component, respectively. The DoD is determined by the azimuth angle $\phi_{Tx,n}$ and the elevation angle $\theta_{Tx,n}$ (the DoA being defined in a similar manner). Moreover, $g_{Tx}(\Omega_{Tx,n})$ and $g_{Rx}(\Omega_{Rx,n})$ are the complex field patterns of the Tx and Rx antennas in the directions $\Omega_{Tx,n}$ and $\Omega_{Rx,n}$, respectively. Hence, the amplitude a_n of the $n-$th multipath component does not depend on the kind of antenna arrays that are used at both link ends. Moreover, the total number N of multipath components can vary over time, as some interactions may appear or disappear owing to the motion of the Tx, Rx or scatterers.

Multidimensional modeling

The double-directional IR is a function of four different parameters, namely time, delay, DoD and DoA. The radio propagation channel can equivalently be described

by several other functions, which are all related one to another through the Fourier transform:

$$\begin{array}{llll} \text{Time :} & t & \xrightarrow{\mathcal{F}} & \text{Doppler frequency :} \quad \nu(\text{or} f_d) \\ \text{Delay :} & \tau & \xrightarrow{\mathcal{F}} & \text{Frequency :} \quad f \\ \text{DoD-DoA :} & \Omega_{Tx-Rx} & \xrightarrow{\mathcal{F}} & \text{Space :} \quad a_{Tx-Rx} \end{array}$$

where a_{Tx-Rx} denotes the vectorized spatial domain (in terms of azimuth and elevation) at the Tx and Rx sides.

It is naturally not realistic to characterize the time-variant channel with an infinite precision: the precise location of the transmitter, receiver and scatterers are not known, so that correspondent phase shift can be considered as a random variable. On a larger scale, the same holds true for $\Omega_{Tx-Rx,n}, \alpha_n$ and τ_n [23]. As a consequence, the multidimensional functions are all stochastic. These functions were first introduced as parts of a system for the characterization of wideband time-varying linear radio propagation channels by Bello in [25]. These Bello's system functions were then generalized to the case of double-directional radio propagation channels [23]. These functions are all related one to another through Fourier transforms, so the double-directional radio propagation channel can be completely characterized even if just one of the mentioned functions is known. For example, the time-varying Tx-Rx angular-resolved Transfer Function (TF) can be expressed as

$$G(f; t; \Omega_{Tx}; \Omega_{Rx}) = \mathcal{F}_{\tau \to f}\{h(\tau; t; \Omega_{Tx}; \Omega_{Rx})\} \tag{1.6}$$

Similarly, $S(\tau; \nu; \Omega_{Tx}; \Omega_{Rx})$ denotes the Doppler-varying Tx-Rx angular resolved Impulse Response, which can be obtained by taking the one-dimensional Fourier transform of $h(\tau; t; \Omega_{Tx}; \Omega_{Rx})$ in the time domain.

However, statistical description of these Bello's system functions practically cannot be done, since it would require the exact knowledge (or, at least, an accurate estimate) of their joint multidimensional Probability Density Function (PDF). It is indeed unrealistic, given the large number of parameters on which they depend. As a consequence, an often used approximation of these generalized Bello's system functions can be obtained by means of their second order statistics, namely their autocorrelation functions (assuming that they are zero-mean) [23, 25]. For example, the time-varying delay- and Tx-Rx angular-resolved correlation functions can be expressed as

$$\begin{aligned} R(\tau, \tau'; t, t'; \Omega_{Tx}, \Omega'_{Tx}; \Omega_{Rx}, \Omega'_{Rx}) = \\ \mathbb{E}\{h(\tau; t; \Omega_{Tx}; \Omega_{Rx}) h^*(\tau'; t'; \Omega'_{Tx}; \Omega'_{Rx})\}, \end{aligned} \tag{1.7}$$

where $(\cdot)^*$ and $\mathbb{E}\{\cdot\}$ denote the conjugate operator and expectation of the random variable.

These multidimensional correlation functions are all related one to another through double Fourier transforms. As a result, the knowledge of one of these system correlation functions is sufficient for the complete characterization of the double-directional radio propagation channel.

Wide-sense stationarity uncorrelated scattering homogeneity

In practice, the multidimensional correlation functions are still very complex for analyzing. Hence, further simplifications are widely used in order to provide simpler

models for the correlation functions, e.g.[16]

1. The Wide Sense Stationarity (WSS) assumption, stating that the first and second order statistics of the radio propagation channel do not change over time. Hence, its mean is constant, while the time correlation only depends on the time difference $\Delta t = t - t'$. Equivalently, in the frequency domain, multipath components undergoing different Doppler shifts are uncorrelated,

2. The Uncorrelated Scattering (US) assumption, stating that the first and second order statistics of the radio propagation channel do not change over frequency. Hence, the frequency correlation only depends on the frequency difference $\Delta f = f - f'$. Equivalently, in the delay domain, multipath components arriving with different delays are uncorrelated,

3. The Homogeneous (H) assumption, stating that the first and second order statistics of the radio propagation channel do not change over space at the Tx and Rx sides. Hence, the antenna correlation only depends on the differences in the spatial domain $\Delta a_{Tx/Rx} = n'_{Tx/Rx} - a_{Tx/Rx}$. Equivalently, in the angular domain, multipath components with different AoDs and AoAs are uncorrelated.

When the three aforementioned assumptions are simultaneously fulfilled, the radio propagation channel is therefore said to be WSS-US-H. The Doppler varying delay- and Tx-Rx angular-resolved correlation function of the radio propagation channel is therefore white in all dimensions, such that (1.7) can be rewritten as

$$\begin{aligned} &R(\tau, \tau'; t, t'; \Omega_{Tx}, \Omega'_{Tx}; \Omega_{Rx}, \Omega'_{Rx}) = \\ &\qquad R(\Delta\tau; \Delta\nu; \Delta\Omega_{Tx}; \Delta\Omega_{Rx})\delta(\Delta\tau)\delta(\Delta\nu)\delta(\Delta\Omega_{Tx})\delta(\Delta\Omega_{Rx}) \end{aligned} \tag{1.8}$$

In other words, the statistics of the radio propagation channel do not change over neither time, nor frequency, nor space.

Time, frequency and space selectivity

The dispersion of the multipath components over time, frequency and space can affect significantly the performances of wireless communication systems. When the WSS-US-H assumption is fulfilled, different metrics have been introduced in order to quantify the frequency and space selectivities of the radio propagation channel, namely

1. The Root Mean Square (RMS) delay spread, as a measure of the frequency selectivity of the radio propagation channel. Introducing the Power Delay Profile (PDP)

$$PDP(\tau) = \mathbb{E}\left\{ \left| \int\int\int h(\tau; t; \Omega_{Tx}; \Omega_{Rx}) dt d\Omega_{Tx} d\Omega_{Rx} \right|^2 \right\} \tag{1.9}$$

the mean delay $\bar{\tau}$ and RMS delay spread τ_{rms} are then defined as [24]

$$\bar{\tau} = \frac{\int \tau PDP(\tau) d\tau}{\int PDP(\tau) d\tau} \tag{1.10}$$

$$\tau_{rms} = \sqrt{\frac{\int (\tau - \bar{\tau})^2 PDP(\tau) d\tau}{\int PDP(\tau) d\tau}} \tag{1.11}$$

The RMS delay spread has been extensively investigated in a number of research papers. In [26] distributed and centralized communication systems with a carrier frequency of 3.53 GHz were investigated in an open space office, depending on the scenario RMS delay spread and mean delay were estimated between 40-51 ns and 120-175 ns, respectively. RMS delay spread of 25-30 ns was reported for MIMO channels measured at 2, 4 and 6 GHz in a conference hall in [27]. A comparison of two communication systems working at 2.9 and 29 GHz was presented in [28], where RMS delay and maximum excess delay were estimated to be 20-45 ns and 300-700 ns for different frequencies. Propagation in a corridor was studied in [29], RMS delay spread of 60 ns and mean delay of 165 ns were reported.

The large fluctuations in these measured RMS delay spread values are due to the fact that they strongly depend on the nature of the scattering environment around the Tx and Rx,

2. The RMS angular spread, as a measure of the spatial selectivity of the radio propagation channel. Introducing, for example, the Angular Power Spectrum (APS) at the Rx side

$$APS(\Omega_{Rx}) = \mathbb{E}\left\{ \left| \int \int \int h(\tau; t; \Omega_{Tx}; \Omega_{Rx}) dt d\tau d\Omega_{Tx} \right|^2 \right\} \tag{1.12}$$

the mean Rx angle $\overline{\Omega_{Rx}}$ and RMS Rx angular spread $\Omega_{Rx,rms}$ are then defined as

$$\overline{\Omega_{Rx}} = \frac{\int \Omega_{Rx} APS(\Omega_{Rx}) d\Omega_{Rx}}{\int APS(\Omega_{Rx}) d\Omega_{Rx}} \tag{1.13}$$

$$\Omega_{Rx,rms} = \sqrt{\frac{\int (\Omega_{Rx} - \overline{\Omega_{Rx}})^2 APS(\Omega_{Rx}) d\Omega_{Rx}}{\int APS(\Omega_{Rx}) d\Omega_{Rx}}} \tag{1.14}$$

Note that $\overline{\Omega_{Rx}}$ is a vector with the mean Tx azimuth and elevation angles $\overline{\theta_{Rx}}$ and $\overline{\phi_{Rx}}$, respectively. The vector $\Omega_{Rx,rms}$ contains the corresponding RMS values $\theta_{Rx,rms}$ and $\phi_{Rx,rms}$. The angular spread at the Tx side can be characterized in a similar manner. Note, that in some papers (for example in [30]) values of RMS azimuth spread change over $[0 \ldots 1]$ where 0 implies that signal arrives from a single direction and 1 corresponds to the signal uniformly spread over all directions, respectively.

These spread parameters are important metrics in the design of communication systems, especially in time-varying environments. Indeed, large RMS delay spreads mean that the transmitted signal is smeared over time, owing to interactions with the scattering environment. Hence, different symbols may arrive at the same time at the Rx side, what yields to inter-symbol interference [24]. Moreover, the RMS angular spread can be used in adaptive beam-forming applications (when considering the Tx or/and Rx antenna directivity). Indeed, large RMS angular spreads imply that the transmitted

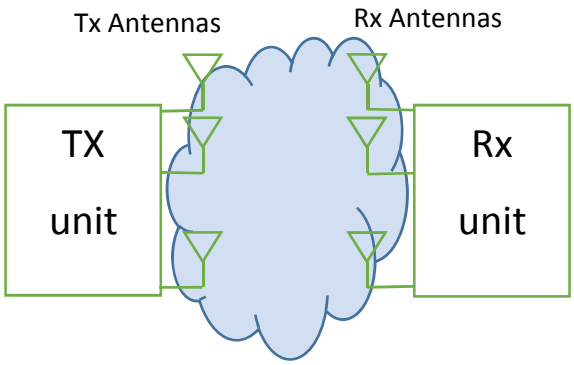

Figure 1.5: Block diagram of the multi-antenna measurement system

signal is smeared over a wide angular range (owing to either the Tx and Rx antennas or the scatterers), such that a large spatial diversity gain is possible. On the other hand, low RMS angular spreads indicate that the Tx or/and Rx antenna directivity can be narrowed, yielding therefore possible higher power gains.

1.1.4 From SISO to MIMO Radio Propagation Channels

Double-directional MIMO radio propagation channels

An advantage of MIMO communication systems with $\mathcal{A}_T$ and $\mathcal{A}_R$ closely-spaced antennas at the Tx and Rx sides respectively (as shown in Figure 1.5) is that they can exploit the double-directional structure of the radio propagation channel. For a narrowband radio propagation channel (or, equivalently, for each delay bin of a wideband one), each Tx-Rx antenna link can undergo a different realization of the radio propagation channel. As a consequence, if a link is affected by a deep fade (due to destructive interferences of the multipath components), then a reliable transmission of the transmit signal is still possible through the other Tx-Rx antenna links that would not be faded (since fading remains coherent only over a distance of the order of the wavelength, it can vary significantly from one element to another for a given antenna array). For a double-directional radio propagation channel,the MIMO channel matrix can be expressed as

$$\mathbf{H}(\tau;t) = \begin{bmatrix} h_{11}(\tau;t) & \cdots & h_{1\mathcal{A}_T}(\tau;t) \\ \vdots & \ddots & \vdots \\ h_{\mathcal{A}_R 1}(\tau;t) & \cdots & h_{\mathcal{A}_R\mathcal{A}_T}(\tau;t) \end{bmatrix} \tag{1.15}$$

where each entry corresponds to a given Tx-Rx antenna pair. The input-output relationship as given in (1.2) can in that case be rewritten as

$$\mathbf{y}(t) = \mathbf{H}(t,\tau) * \mathbf{x}(t) + \mathbf{n}(t), \tag{1.16}$$

where $\mathbf{x}$ denotes a $\mathcal{A}_T \times 1$ vector containing the transmitted samples, while $\mathbf{y}$ and $\mathbf{n}$ are $\mathcal{A}_R \times 1$ vectors containing the received samples and the receiver noise, respectively. Combining equations (1.5) and (1.15), the expression of the double-directional MIMO radio propagation channel can then be rewritten as

$$\mathbf{H}(\tau; t) = \sum_{n=0}^{N} e^{j2\pi f_d t} \mathbf{G}_{Rx}(\Omega_{Rx,n}) a_n \mathbf{G}_{Tx}^{H}(\Omega_{Tx,n}) \delta(\tau - \tau_n), \tag{1.17}$$

where $\mathbf{G}_{Rx}$ and $\mathbf{G}_{Tx}$ are $\mathcal{A}_T \times 1$ and $\mathcal{A}_R \times 1$ vectors including the antenna pattern effects and the steering vector of the Tx and Rx antenna arrays in directions $\Omega_{Rx,n}$ and $\Omega_{Tx,n}$, respectively.

1.1.5 Space-only characterization of MIMO radio propagation channels

Complete statistical characterization of MIMO radio propagation channels (under assumption that they can be fully described by their second-order statistics) by using the multidimensional modeling approach presented in Section 1.1.3. However, due to the large number of the correlation functions parameters, it is difficult to interpret them even in the case if the correlation functions can be estimated from the measurements, which is not a trivial task in itself. Since MIMO radio communication systems exploit the spatial diversity of the propagation channel, it is then reasonable to consider the space-only characterization of the underlying radio propagation channels. If both the frequency and time shifts are set to zero (i.e. $f = f'$ and $t = t'$), then (1.7) can be rewritten as the time-frequency dependent full spatial correlation matrix

$$R_{full}(t, f) = \mathbb{E}\{\mathbf{vec}[\mathbf{H}(t, f)]\mathbf{vec}[\mathbf{H}(t, f)]^H\} \tag{1.18}$$

where the operator $\mathbf{vec}[\cdot]$ stacks the matrix columns into a single column vector. For MIMO channels with a small relative bandwidth compared to the center frequency (in this thesis the relative bandwidth is below 5%), it can be expected that the spatial structure of the channel does not change significantly within the bandwidth. Then, it is possible to consider only the temporal variation of the spatial structure and use the frequency domain as additional realization domain. The corresponding correlation function is then the frequency averaged time-variant full spatial correlation matrix

$$R_{full}(t) = \mathbb{E}_f\{\mathbb{E}\{\mathbf{vec}[\mathbf{H}(t, f)]\mathbf{vec}[\mathbf{H}(t, f)]^H\}\}, \tag{1.19}$$

where $\mathbb{E}_f\{\cdot\}$ is the expectation with respect to frequency. Its $\mathcal{A}_R\mathcal{A}_T \times \mathcal{A}_R\mathcal{A}_T$ elements represent the correlation coefficients between all Tx-Rx antenna links, which can also be classified as

1. The Tx correlation coefficients, which are due to interactions at the Tx side. They can be expressed as the $\mathcal{A}_T \times \mathcal{A}_T$ spatial correlation matrix

$$R_{Tx}(t) = \mathbb{E}_f\{\mathbb{E}\{\mathbf{H}^T(t, f)\mathbf{H}(t, f)^*\}\}, \tag{1.20}$$

   where $(\cdot)^T$ is a transpose operator.

2. The Rx correlation coefficients, which are due to interactions at the Rx side. They can be expressed as the $\mathcal{A}_R \times \mathcal{A}_R$ spatial correlation matrix

$$R_{Rx}(t) = \mathbb{E}_f\{\mathbb{E}\{\mathbf{H}(t,f)\mathbf{H}^H(t,f)\}\}, \tag{1.21}$$

   where $(\cdot)^H$ is a conjugate transpose (Hermitian transpose) operator.

3. The cross-correlation (off-diagonal) coefficients, which are due to combined interactions at both Tx-Rx sides. Though, a number of these coefficients are difficult to be interpreted physically.

The dimension of the full spatial correlation matrices grows quadratically with the sizes of the MIMO antenna arrays used at the Tx and Rx sides. This draws important issues in terms of

- complexity; since they can be too large to be used as such in communication schemes,

- identifiability; since they may be ill-conditioned if they are estimated from an insufficient number of time instants.

Considering these issues, an estimation of full spatial correlation matrices is not often used in MIMO radio communication systems. Since Tx and Rx spatial correlation matrices are indeed simpler to estimate, they are much more popular in practice. Moreover, these matrices can be used in adaptive processing at the Tx and Rx sides separately, long-e.g. when term time-averaged spatial statistics are evaluated at the Rx side and feedback to the Tx one, so that this latter can optimize its transmission scheme. As a consequence, these spatial correlation matrices provide useful information on changes in the radio propagation channel as seen from one link's end.

Their structures can be analyzed by means of their respective eigenvalue decomposition, which is given by

$$\mathbf{R_{Tx}} = \mathbf{U_{Tx}}\mathbf{\Lambda_{Tx}}\mathbf{U_{Tx}^H} \tag{1.22}$$

$$\mathbf{R_{Rx}} = \mathbf{U_{Rx}}\mathbf{\Lambda_{Rx}}\mathbf{U_{Rx}^H} \tag{1.23}$$

where $\mathbf{U_{Tx}}$ (resp. $\mathbf{U_{Rx}}$) is a unitary matrix containing the eigenmodes of $\mathbf{R_{Tx}}$ (resp. $\mathbf{R_{Rx}}$) at their columns, whereas $\mathbf{\Lambda_{Tx}}$ (resp. $\mathbf{\Lambda_{Tx}}$) is a diagonal matrix containing the corresponding eigenvalues sorted in descending order, such that $\lambda_1 \geq \lambda_2 \geq \cdots \geq \lambda_{\mathcal{A}_{T/R}}$. The strongest eigenvalues (that exceed a certain threshold, which depends on the measurement system) characterize the signal subspace, i.e. the number of uncorrelated fading processes that contribute to the radio propagation channel (while the remaining ones are too weak and below the noise level, so that they can be associated to the noise subspace). Even though these strongest eigenvalues do not have any physical interpretation in the radio wave propagation (they indeed correspond to weighted sum of multipath components), they characterize the degree of spatial diversity in the radio propagation channel.

1.1.6 Measuring Non-Stationarity

It is obvious, that the WSS assumption is not realistic for real-world radio propagation channels since it implies that the statistics of the radio propagation channel do never change over infinite time.

The WSS assumption is not fulfilled since the channel statistics are time-varying, due to the mobility of the Tx and Rx nodes as well as of the scatterers. Some scatterers can indeed suddenly appear (or disappear) in the environment surrounding the Tx and Rx. The LOS component can also be intermittently be obstructed by various obstacles. All these effects result in a non-stationary behavior of the radio propagation channel over time.

However, the radio propagation channel statistics do not change instantaneously, so that it is possible to identify bounded time or traveled distance within which they remain constant (i.e. over which the WSS-US-H assumption is locally fulfilled) to still benefit from simplifications given by the assumptions. Reliable estimates of the radio propagation channel statistics can therefore be obtained only over those time intervals.

Different methods have been proposed in the literature to measure the non-stationarity of radio propagation channels and to identify stationarity regions.

The stationarity of Single-Input Single-Output (SISO) radio propagation channels was investigated in [31], where local regions of stationarity were identified based on the correlation between consecutive PDPs. For the definition of local stationarity, the instantaneous rower delay profile must be calculated and an average over several of them should be calculated in order to remove fading:

$$\overline{PDP(t_i,\tau)} = \frac{1}{N}\sum_{i}^{i+N-1} |h(t_i,\tau)|^2. \tag{1.24}$$

Next, the temporal correlation coefficient between averaged PDPs can be computed as

$$c_{i,j} = \frac{\int \overline{PDP(t_i,\tau)} \cdot \overline{PDP(t_j,\tau)} d\tau}{\max\left\{\int \overline{PDP(t_i,\tau)}^2 d\tau, \int \overline{PDP(t_j,\tau)}^2 d\tau\right\}} \tag{1.25}$$

The channel is considered stationary if the correlation coefficient does not undergo a certain threshold(0.9). This approach can be useful for systems where performance is highly dependent on an accurate knowledge of the PDPs and will be used in Chapter5.

Alternatively, a framework for the characterization of the non-stationary behavior of SISO radio propagation channels over time and frequency was proposed in [32]. The concept of Local Scattering Function (LSF) was first introduced as an extension of the scattering function to the non-stationary case. Stationarity regions in time and in frequency were then identified by applying similarity metrics (e.g. collinearity, spectral divergence, etc.) to the so-estimated LSFs. This approach has been used for the characterization of the non-stationary behavior of vehicular MIMO radio propagation channels and the identification of stationarity regions in [33, 34].

Regarding Single-Input Multiple-Output (SIMO) radio propagation channels, the F-eigen ratio was introduced in [35] to measure the discrepancy between spatial correlation matrices at the Rx side. It corresponds to the penalty that is undergone (in terms of power loss) when out-dated spatial statistics are used in beam-forming applications instead of the actual ones. Nonetheless, the F-eigen ratio is interesting only

when the transmission is done over a reduced number of eigen-modes, and hence loses of its interest when all the eigen-modes are considered (e.g. in MIMO communication systems). For MIMO radio propagation channels, statistical tests based on their evolutionary spectrum estimated at different time instants were used in [36, 37] to determine time intervals over which the WSS assumption does remain valid. Stationarity distances were also estimated, which were found to be larger in presence of the LoS component. However, none of these methods really takes advantage of the knowledge of the spatial structure of MIMO (or SIMO) radio propagation channels. For that purpose, the Correlation Matrix Distance (CMD) was introduced in [16, 38, 39, 40, 41] in order to determine the amount of change in the spatial structure of the underlying MIMO radio propagation channel over time.

The CMD was introduced as a metric for the characterization of the amount of change between two arbitrary time-dependent spatial correlation matrices. Let us consider two spacial correlation matrices R and $\hat{R}$, then the correlation matrix distance between the matrices can be expressed as

$$d_{corr} = 1 - \frac{\mathbf{tr}\{R\hat{R}\}}{\|R\|_F \|\hat{R}\|_F}, \tag{1.26}$$

where $\mathbf{tr}\{\cdot\}$ and $\|\cdot\|_F$ are the trace operator and the Frobenius norm, respectively. The CMD is based on the angle between the two spatial correlation matrices that are being compared and can be interpreted as the measure of their orthogonality, i.e. how much their respective signal subspaces overlap, independently on changes in the received power. The CMD ranges between zero when the compared spatial correlation matrices are identical (up to a scaling factor) and one when they are completely different (i.e. uncorrelated).

The non-stationarity of MIMO channels can be measured by applying the metric presented in (1.26) to the time-frequency variant spacial correlation matrices. It allows us to estimate stationarity regions in which the correlation distance is bellow a threshold (conventionally, the threshold of 0.2 is used in literature).

1.2 Propagation Modeling

Fading, in general, refers to the variation of the received signal power caused by changes in the transmission medium or path. Fading is usually classified as Large-Scale Fading (LS fading) or Small-Scale Fading (SS fading). Path-loss and large-scale fading are dominant when the receiver moves over distances greater than several tens of the carrier wavelength. Large-scale fading plays an important role in determining the node coverage area. On the other hand, small-scale fading is caused by multipath propagation. This effect plays an important role in determining link level performance in terms of Bit Error Rate (BER), Average Fade Duration (AFD), etc.

1.2.1 Path-Loss and Mean Large-Scale Fading

Path-loss is the attenuation in the transmitted signal as it propagates from the transmitter to the receiver. This attenuation may be caused by effects such as free-space loss, refraction, diffraction, reflection and absorption. Path-loss is also influenced by environment features such as walls, furniture, indoor vegetation, wall's materials etc.

The simplest path-loss model assumes a LOS link between the Tx and Rx and propagation in free space. Under these assumptions, the received signal power is given as [24]

$$P_R = P_T G_T G_R \frac{\lambda^2}{4\pi d^2} \tag{1.27}$$

where P_T is the transmitted power, G_T and G_R are the transmit and receive antenna gains, respectively, λ is the carrier wavelength, and d is the distance between the Tx and Rx. Note that the path-loss exponent (the power of the distance dependence) in this equation is 2 for free-space propagation.

However, the signals in wireless communications do not experience free space propagation. Therefore, several different models such as the Okumura-Hata, Lee, Walfish-Ikegami, etc., [24] have been proposed to model path-loss in different propagation environments such as urban, rural, and indoor areas. Conventionally, path-loss is modeled as [42]

$$\Lambda' = \Lambda_0 + \eta \cdot 10 \log_{10} \left(\frac{d}{d_0} \right), \tag{1.28}$$

where Λ_0 is the deterministic path-loss at the reference distance (It is typically 1 m for indoor environments). The path-loss exponent n denotes the relationship between the distance and the received power. Experiments indicate that the actual path-loss exponents are between 2.5-8.

The path-loss model described above assume that the path-loss is constant at a given distance. However, as an indoor environment typically is reach of various static objects such as furniture, desktops etc., all these static obstacles result in random variations of the received power at a given distance for different rooms. In [3, 43], this effect was called mean LS fading $\overline{S}$ and it was found to be normal with zero mean (when expressed in decibels) over the whole set of rooms/links. Considering the both components, the combined path-loss and mean LS fading $\Lambda = \Lambda' + \overline{S}$ can be defined as

$$\Lambda = \Lambda_0 + \eta \cdot 10 \log_{10} \left(\frac{d}{d_0} \right) + \overline{S}. \tag{1.29}$$

1.2.2 Dynamic Large-Scale Fading

When the deterministic path-loss and mean LS fading are removed, mean power, averaged over about 10-20 wavelengths, itself shows fluctuations over time. These random variations of locally averaged received power over large distances, typically on the order of a few tens or hundreds wavelengths, are known as large-scale fading, due to large obstacles such as building's structures, moving people, the user of the node(so-called body fading or shadowing) etc. The obstacles affecting the propagation of MPCs can be very different from each other, resulting in large-scale variations at different locations, while having approximately the same Tx-Rx distance. At any distance d, LS fading S measured in dB is usually modeled as a lognormal random variable, which takes into account random variations of the received power around the path-loss curve, with the PDF as

$$p(x) = \frac{1}{2\pi\sigma_S x} \exp^{\frac{(\ln x - \mu_S)^2}{2\sigma_S^2}} \tag{1.30}$$

where μ_S and σ_S^2 are the mean and the variance of the corresponding normal random variable respectively.

In [43] it is shown that the LS fading might be described by a t-location scale distribution

$$p\left(x \mid \nu, \mu, \sigma_{\tilde{s}}\right) = \frac{\Gamma\left(\frac{\nu+1}{2}\right)}{\Gamma\left(\frac{\nu}{2}\right)\sigma_{\tilde{s}}\sqrt{\pi\nu}}\left(1+\frac{1}{\nu}\left(\frac{x-\mu}{\sigma_{\tilde{s}}}\right)^2\right)^{-\frac{\nu+1}{2}} \tag{1.31}$$

with mean (μ), ν degrees of freedom and a scale parameter $\sigma_{\tilde{s}}$. This distribution results from compounding a normal distribution with mean μ and unknown variance, with an inverse gamma distribution placed over the variance with parameters $\alpha_\Gamma = \nu/2$ and $\beta_\Gamma = \nu\sigma_{\tilde{s}}^2/2$. In other words, the LS fading is assumed to have a Gaussian distribution with an unknown variance distributed as inverse gamma, and then the variance is marginalized out. Various mechanisms typical for different scenarios can lead to variations of the value of the scale parameter $\sigma_{\tilde{s}}$ depending on the type of mobility and the motion scale.

In multi-antenna systems, the transmitter and/or the receiver consist of arrays, i.e. they are made of several closely-spaced antennas. The fading channel between each transmit-receive antenna pair can be modeled as a SISO channel. Yet each SISO channel constituting of the MIMO channel may be characterized by a different shadowing (however, the size of the arrays is such that the path-loss is usually identical on all links). For uni-polarized transmissions and reduced inter-element spacings, this is nevertheless a not-so-common situation [23].

1.2.3 Small-Scale Fading

Small-scale fading describes the random fluctuations of the received power over short distances, typically a few wavelengths, due to constructive or destructive interference of MPCs impinging at the receiver. Different distributions are proposed to characterize the random fading behavior of the signal envelope, suitable for different wireless systems and propagation environments. The Rayleigh and Rice distributions, both based on a complex Gaussian distribution, are the most commonly used models. Considering a large number of MPCs with amplitudes and random phases, the signal envelope of small-scale fading thus follows a Rayleigh distribution with PDF [24]

$$p(x) = \frac{x}{\sigma_{SS}^2} e^{-\frac{x^2}{2\sigma_{SS}^2}}, x \geq 0, \tag{1.32}$$

where σ_{SS} is the scale parameter describing statistical dispersion of the probability distribution.

It stems from a signal that is zero-mean complex Gaussian with a standard deviation σ, as motivated by the Central Limit Theorem (CLT) [24]. The zero-mean makes this distribution useful for Non-Line-of-Sight (NLOS) conditions. However, if a strong coherent component dominates the others, then signal envelope of small-scale variations follows the Ricean distribution (the Rayleigh is a special case of the Ricean distribution) with PDF given by

$$p(x) = \frac{x}{\sigma_{SS}^2} e^{-\frac{x^2+A^2}{2\sigma_{SS}^2}} I_0\left(\frac{Ax}{\sigma_{SS}^2}\right), x \geq 0 \tag{1.33}$$

where I_0 is the zero-order modified Bessel function of the first kind and A is the amplitude of the dominant component. Usually, the Ricean distribution is described by the Ricean K-factor, defined as [24]

$$K = \frac{A^2}{2\sigma_{SS}^2} \tag{1.34}$$

Thus (1.33) can then be rearranged as

$$p(x) = \frac{x}{\sigma_{SS}^2} e^{-\left(K + \frac{x^2}{2\sigma_{SS}^2}\right)} I_0\left(\frac{\sqrt{2K}}{\sigma_{SS}^2} x\right), x \geq 0 \tag{1.35}$$

where the Rician K-factor determines the amount of SS fading. This important parameter of the Ricean distribution represents the ratio between the average power of the specular and diffuse components of the signal. In this case, the small-scale fading has unit average power when $2\sigma_{SS}^2 = \frac{1}{K+1}$. Conventionally in the literature, the Rician distribution is often associated with the presence of a LOS component [24], however it can also describe fading in the case of strong coherent specular reflections, e.g., a static scatterer located in the vicinity of the moving Rx [23]. Large values of the Rician K-factor correspond to weak fading conditions (or no fading), while $K = 0$ indicates that SS fading is Rayleigh distributed and there is no impact of the LOS term. The K-factor is a frequently studied parameter in channel modeling research; as illustrated in Chapter 5.

From a system design point of view, the type of fading distribution envelope is vital as it determines the fading margin [24] required to achieve coverage with a certain outage probability.

The combined effects of large-scale and small-scale fading can be illustrated through a joint distribution, e.g., the Suzuki distribution [44]. However, the more familiar approach is to provide separate PDFs for two fading types.

As it was shown in [3, 43], small-scale fading is rather described by a combination of several different distributions. The single distribution describing this type of fading is presented in [45] and called the Second Order Scattering Fading (SOSF) Distribution.

1.3 The SOSF Distribution

It is shown in [3] that, for indoor environments, small-scale fading can be described by a single distribution including a weighted combination of a line-of-sight component, a Rayleigh fading component and a Double Rayleigh fading component. Hence, any realization of the time-frequency channel can be expressed as

$$H = \omega_0 e^{j\theta} + \omega_1 H_1 + \omega_2 H_2 H_3 \tag{1.36}$$

where H_1, H_2, H_3 are i.i.d. complex normal random variables with zero mean and unit variance, and θ is a constant phase shift angle in [0, 2π]. The probability density function of $g = |H|$ is given, as shown in [45] and [3], by the so-called second order scattering fading (SOSF) distribution

$$p_{SOSF}(g) = \int_0^\infty \omega e^{-\omega_1^2 \omega^2/4} \frac{4 J_0(g\omega) J_0(\omega_0 \omega)}{4 + \omega_2^2 \omega^2} \, d\omega \tag{1.37}$$

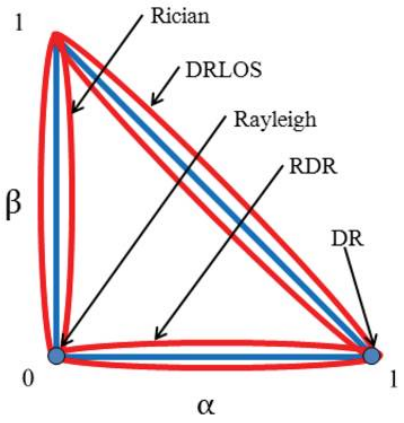

Figure 1.6: Triangle of the parameters of SOSF distribution

where J_0 is the Bessel function of the first kind and zeroth order.

It can be useful to derive simpler forms for distribution functions in special cases of the SOSF distribution. Probability density functions of Double Rayleigh (DR) and Rayleigh - Double Rayleigh (RDR) distributions can be found in [45] and [19], respectively. The distribution for a combination of Double Rayleigh and Line-of-Sight (DRLOS) can be derived by using the same concept as used in [45] and the standard integral [46, §6.541] as

$$p_{DRLOS}(g) = \frac{4g}{\omega_2^2} I_0\left(\frac{2a_1}{\omega_2}\right) K_0\left(\frac{2a_2}{\omega_2}\right) \tag{1.38}$$

where I_0 and K_0 are the modified Bessel functions of the first kind and zeroth order and the modified Bessel functions of the second kind and zeroth order, respectively, parameters a_1 and a_2 are given by

$$a_1 = \begin{cases} g & [g < \omega_0] \\ \omega_0 & [g \geq \omega_0] \end{cases}$$

$$a_2 = \begin{cases} \omega_0 & [g < \omega_0] \\ g & [g \geq \omega_0] \end{cases}$$

Since $\mathbb{E}\{g^2\} = 1$, we have that $\omega_0^2 + \omega_1^2 + \omega_2^2 = 1$ and the distribution can be specified by only two parameters [47]

$$\alpha = \frac{\omega_2^2}{\omega_0^2 + \omega_1^2 + \omega_2^2} \tag{1.39}$$

$$\beta = \frac{\omega_0^2}{\omega_0^2 + \omega_1^2 + \omega_2^2} \tag{1.40}$$

where (α, β) are constrained to the triangle $\alpha \geq 0$, $\beta \geq 0$, and $\alpha + \beta \leq 1$ shown in Figure 1.6. In specific cases of the triangle, the SOSF distribution reduces to Rician

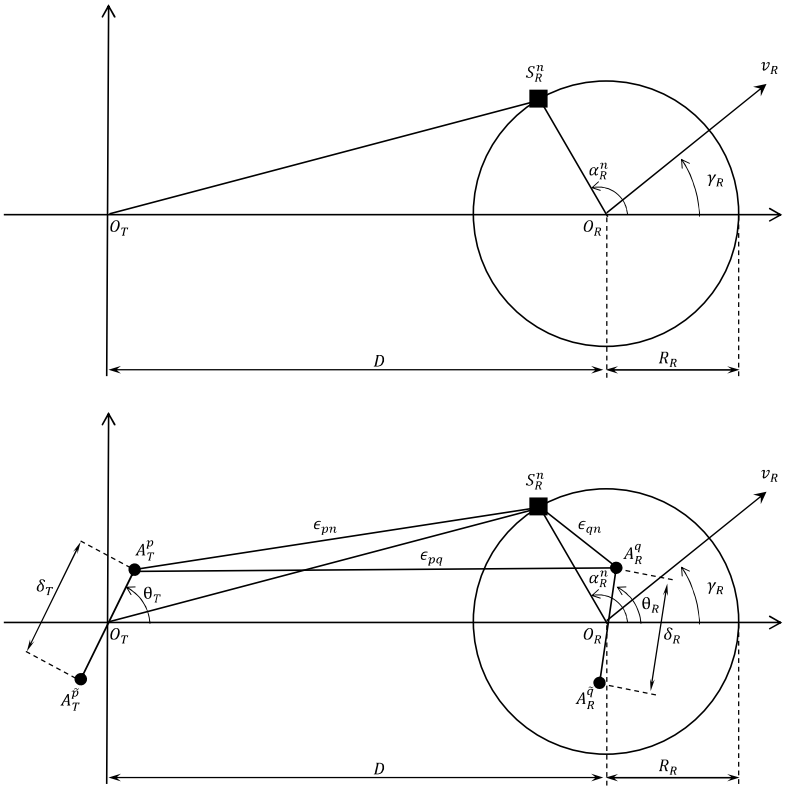

Figure 1.7: The geometrical single-ring model for the SISO (top) and MIMO (bottom) cases

($\alpha = 0, \beta > 0$, with K-Factor $K = \frac{\beta}{1-\beta}$), Rayleigh ($\alpha = 0, \beta = 0$), Double Rayleigh ($\alpha = 1, \beta = 0$), DRLOS ($\alpha + \beta = 1, \alpha < 1, \beta < 1$) and Rayleigh-Double-Rayleigh distribution ($0 < \alpha < 1, \beta = 0$). Based on previous studies [48, 3], we can expect that these distributions describe predominant fading mechanisms for our environment.

1.4 Single Mobile Channels

A single mobile (also known as Fixed-to-Mobile (F-to-M)) channel is a channel between a transmission node, which is stationary, and a Mobile Station (MS). A typical assumption is that the static node is relatively free of local scattering, whereas the mobile node is surrounded by objects acting as scatterers.

1.4.1 Reference Model for Single Mobile Fading Channels

In the past five decades, several modeling approaches for single mobile channels have been proposed. The pioneering work done by Clarke provides a theoretical reference model for SISO single mobile channels [49, 50].

Clarke assuming narrowband, frequency flat fading, and NLOS propagation proposed a reference model defining the complex faded envelope as

$$g(t) = \lim_{N\to\infty} \sum_{n=1}^{N} C_n e^{j\left(\frac{2\pi f_R^{max} t}{c}\cos\alpha_R^n + \phi_n\right)}, \tag{1.41}$$

where N is the number of propagation paths and ϕ_n is the random phase of the $n-$th multipath component, uniformly distributed on the interval $[-\pi, \pi)$. The maximum Doppler frequency $f_R^{max} = \frac{v_R}{\lambda}$ in Hertz, λ is the carrier wavelength, and v_R is the speed of the MS. The Angle of Arrival (AoA), α_R^n, depends on the scattering environment and the antenna radiation pattern. It is assumed that C_n, α_R^n and ϕ_n are mutually independent and that α_R^n is uniformly distributed on the interval $[-\pi, \pi)$. Invoking the CLT [24], the real part, $g_i(t) = \Re\{g(t)\}$, and the imaginary part, $g_q(t) = \Im\{g(t)\}$, of the complex faded envelope are Gaussian random processes as $N \to \infty$. Therefore, the envelope $|g(t)|$ is Rayleigh distributed and the phase $\theta_g(t)$ is uniformly distributed. The auto- and cross-correlation functions of the reference model, assuming a 2-D scattering environment, are summarized below [24]

$$R_{g_{i/q}g_{i/q}}(\tau) = \mathbb{E}[g_{i/q}(t)g_{i/q}(t+\tau)] = J_0\left(2\pi f_R^{max}\tau\right) \tag{1.42}$$

$$R_{g_i g_q}(\tau) = \mathbb{E}[g_{i/q}(t)g_{q/i}(t+\tau)] = 0 \tag{1.43}$$

where $\mathbb{E}[\cdot]$ is the statistical expectation operator and J_0 is the zeroth-order Bessel function of the first kind.

These statistical properties can be used to design a communication system, i.e. to choose modulation, interleaving, and coding schemes at the transmitting end and the type of channel estimator and decoder at the receiving end.

1.4.2 Reference Model for Single Mobile Multi-Antenna Fading Channels

The one-ring model was extended to the MIMO case in [51] and later generalized in [52] to include the impact of the LOS term and various models as special cases.

$$\begin{aligned} g^{pq}(t) &= \sqrt{\frac{1}{K_{pq}+1}} \\ &\times \lim_{N\to\infty} \frac{1}{\sqrt{N}} \sum_{n=1}^{N} C_n e^{j\psi - \frac{j2\pi}{\lambda}[\epsilon_{pn}(\phi_n)+\epsilon_{qn}(\phi_n)] + j2\pi f_R^{max} t\cos(\phi_n - \alpha_R^n)}, \end{aligned} \tag{1.44}$$

$$g_{LOS}^{pq}(t) = \sqrt{\frac{K_{pq}}{K_{pq}+1}} \times e^{-\frac{j2\pi}{\lambda}\epsilon_{pq} + j2\pi f_R^{max}\{\cos\phi_{LOS} - \gamma_R\}} \tag{1.45}$$

where ϵ_{pn} and ϵ_{qn} are the distances shown in Figure 1.7, which are functions of the AoA of the wave traveling from the $n-$th scatterer toward the user and K_{pq} is the Rician K-factor for the correspondent link. Note that $\mathbb{E}[|(g^{pq})^2| = 1]$.

Correlation functions are expressed as

$$
\begin{aligned}
R^{g_{pq}g_{\bar{p}\bar{q}}}(\tau) = & \frac{e^{jc_T\cos\theta_T}}{I_0(\kappa)} \\
& \times I_0\Bigg(\{\kappa^2 - a^2 - b_R^2 - b_T^2\Delta^2\sin^2\theta_T + 2ab_R\cos(\theta_R - \gamma_R) \\
& + 2b_T\Delta\sin(\theta_T)\times[a\sin\gamma_R - b_R\sin\theta_R] \\
& - j2\kappa\big[a\cos(\mu-\gamma_R) - b_R\cos(\mu-\theta_R) \\
& - b_T\Delta\sin(\theta_T)\sin\mu\big]\}^{\frac{1}{2}}\Bigg)
\end{aligned}
\tag{1.46}
$$

where $a = 2\pi f_R^{max}\tau$, $b_R = 2\pi\delta_R/\lambda$, $b_T = 2\pi\delta_T/\lambda$, $\tan(\Delta) = R_R/D$ and κ is a parameter of the Tikhonov-von Mises (TvM) distribution:

$$
p(\alpha) = \frac{e^{\kappa\cos(\alpha-\mu)}}{2\pi I_0(\kappa)} \qquad \alpha\in[-\pi,\pi) \tag{1.47}
$$

where is I_0 the zeroth-order modified Bessel function, $\mu\in[-\pi,\pi)$ accounts for the mean direction of AOA seen by the user, and $\kappa\geq 0$ controls the width of AOA. For $\kappa = 0$ (isotropic scattering) we have $f(\alpha) = 1/2\pi$, while for $\kappa = \infty$ (extremely non-isotropic scattering) the TvM PDF becomes a Dirac delta function, concentrated at $\alpha = \mu$.

Notice that the simplest special case of (1.46) is Clarkes temporal correlation model (1.42), obtained for $\delta_T = \delta_R = 0$ (single transmit−receive antennas) and $\kappa = 0$ (isotropic scattering around the user).

1.5 Double Mobile Channels

Double mobile (Mobile-to-Mobile (M-to-M)) channels have characteristics that are widely different from single mobile channels. In double mobile channels, both the Tx and Rx are in motion surrounded by local scatterers, as shown in Figures 1.8,1.9.

1.5.1 Reference Model for Double Mobile Fading Channels

Akki and Haber [53, 54] showed that for double mobile channels the fading envelope is Rayleigh distributed, but the second order statistics differ from single mobile channels. They were the first to propose a theoretical reference model for SISO double mobile channels based on the geometrical representation shown in Figure 1.8.

This model defines two rings of fixed scatterers, one around the Tx and another around the Rx. Around the transmitter, M omnidirectional scatterers S_T^m lie on a ring of radius R_T. Similarly, around the receiver, N omnidirectional scatterers lie on a ring of radius R_R and the $n-$th receive scatterer is denoted by S_R^n. The distance between the transmitter and the receiver is D. The Tx and Rx are moving with speeds v_T and v_R in directions described by angles γ_T and γ_R, respectively. The symbols α_T^m and α_R^n denote Angle of Departure (AoD) and AoA, respectively.

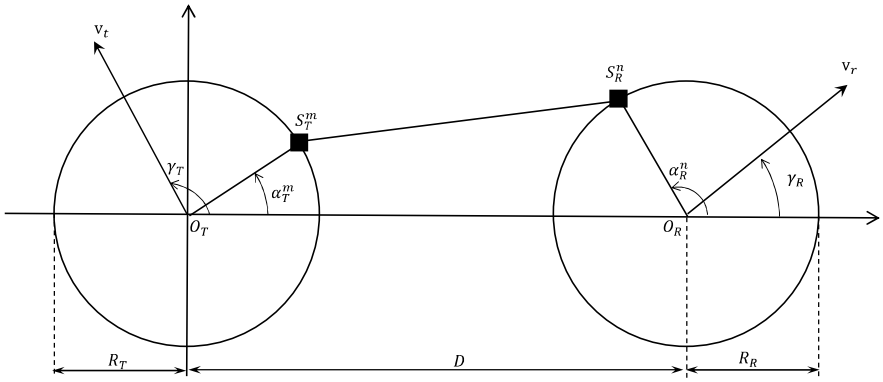

Figure 1.8: The geometrical double-ring model for the SISO case

Assuming narrowband, frequency flat fading, and NLOS propagation, Akki and Habers SISO double mobile reference model defines the complex faded envelope as [53]

$$g(t) = \lim_{N\to\infty} \sqrt{\frac{2}{N}} \sum_{n=1}^{N} e^{j\left(\frac{2\pi f_T^{max} t}{c} \cos\alpha_T^n + \frac{2\pi f_R^{max} t}{c} \cos\alpha_R^n + \phi_n\right)}, \tag{1.48}$$

where N is the number of propagation paths, f_T^{max} and f_R^{max} are the maximum Doppler frequencies, α_T^n and α_R^n are the AoD and the AoA of the $n-$th propagation path measured with respect to the Tx and Rx velocity vectors, respectively, and ϕ_n is the phase associated with the propagation path. It is assumed that α_T^n, α_R^n and ϕ_n are mutually independent random variables and that ϕ_n is uniformly distributed on the interval $[\pi, \pi)$. Since the Central Limit Theorem statements, the I component, $g_i(t) = \Re\{g(t)\}$, and the Q component, $g_q(t) = \Im\{g(t)\}$, of the complex faded envelope are Gaussian random processes as $N \to \infty$. Therefore, the envelope $|g(t)|$ is Rayleigh distributed and the phase $\theta_g(t)$ is uniformly distributed. The auto- and cross-correlation functions of the reference model, assuming omni-directional antennas and a 2-D isotropic scattering environment, are in the limit $N \to \infty$ [53, 54]

$$R_{g_{i/q}g_{i/q}}(\tau) = \mathbb{E}[g_{i/q}(t)g_{i/q}(t+\tau)] = J_0\left(2\pi f_T^{max}\tau\right) J_0\left(2\pi f_R^{max}\tau\right) \tag{1.49}$$

$$R_{g_i g_q}(\tau) = \mathbb{E}[g_{i/q}(t)g_{q/i}(t+\tau)] = 0 \tag{1.50}$$

Note that auto-correlation functions of double mobile channels are a product of two Bessel functions in contrast to single mobile channel, where the corresponding functions involve single Bessel functions (1.42).

1.5.2 Reference Model for Double Mobile Multi-Antenna Fading Channels

Pätzold et al. were the first to propose a reference model for MIMO double mobile channels [55, 56]. They used the double-ring model, proposed in [57], to derive their

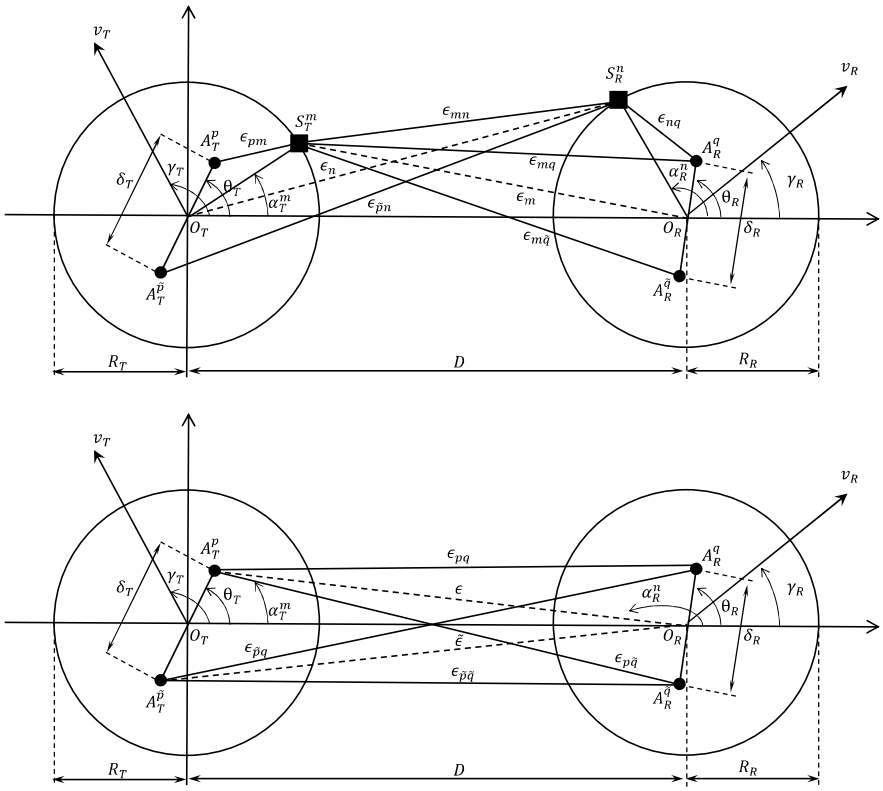

Figure 1.9: The geometrical double-ring model for the MIMO NLoS (top) and LoS (bottom) cases

reference model. However, the model proposed in [55, 56] included just so called double bounced waves i.e. waves scattered on both rings around the nodes. It is obvious that this approach is incomplete. In [58], Zajic and Stüber proposed a model considering the single bounced components as well. Figure 1.9 shows the double-ring model for MIMO double mobile channels with $\mathcal{A}_T = \mathcal{A}_R = 2$ antenna elements.

This model defines two rings of fixed scatterers, one around the Tx and another around the Rx. Around the transmitter, M omnidirectional scatterers lie on a ring of radius R_T, and the $m-$th transmit scatterer is denoted by S_T^m . Similarly, around the receiver, N omnidirectional scatterers lie on a ring of radius R_R and the $n-$th receive scatterer is denoted by S_R^n. The distance between the transmitter and the receiver is D. The spacing between two antenna elements at the Tx and Rx is denoted by δ_T and δ_R, respectively. Angles θ_T and θ_R describe the orientation of the Txs antenna array and the Rxs antenna array, respectively, relative to the x-axis.

Similarly to the SISO model, the Tx and Rx are moving with speeds v_T and v_R in directions described by angles γ_T and γ_R, respectively. The symbols α_T^m and α_R^n denote AoD and AoA, respectively. Finally, the symbols ϵ with various subscripts denote distances shown in Figure 1.9.

Using the double ring geometrical model, the reference model [58] defines the complex faded envelope of the link $A_T^p - A_R^q$ under narrowband, frequency flat fading propagation assumptions as

$$g_{DB}^{pq}(t) = \sqrt{\frac{\eta_{DB}}{K_{pq}+1}} \lim_{M\to\infty} \sqrt{\frac{1}{MN}} \sum_{m,n=1}^{M,N} e^{-j\frac{2\pi}{\lambda}(\epsilon_{pm}+\epsilon_{mn}+\epsilon_{nq})} \times e^{j2\pi t(f_T^{max}\cos(\alpha_T^m-\gamma_T)+f_R^{max}\cos(\alpha_R^n-\gamma_R))+\phi_{mn}}, \tag{1.51}$$

$$g_{SBT}^{pq}(t) = \sqrt{\frac{\eta_{SBT}}{K_{pq}+1}} \lim_{M\to\infty} \sqrt{\frac{1}{M}} \times \sum_{m=1}^{M} e^{j\left[-\frac{2\pi}{\lambda}(\epsilon_{pm}+\epsilon_{mq})+2\pi t(f_T^{max}\cos(\alpha_T^m-\gamma_T)+f_R^{max}\cos(\alpha_R^m-\gamma_R))+\phi_m\right]}, \tag{1.52}$$

$$g_{SBR}^{pq}(t) = \sqrt{\frac{\eta_{SBR}}{K_{pq}+1}} \lim_{N\to\infty} \sqrt{\frac{1}{N}} \times \sum_{n=1}^{N} e^{j\left[-\frac{2\pi}{\lambda}(\epsilon_{pn}+\epsilon_{nq})+2\pi t(f_T^{max}\cos(\alpha_T^n-\gamma_T)+f_R^{max}\cos(\alpha_R^n-\gamma_R))+\phi_n\right]}, \tag{1.53}$$

$$g_{LOS}^{pq}(t) = \sqrt{\frac{K_{pq}}{K_{pq}+1}} e^{j2\pi t f_T^{max}\cos(\pi-\alpha_{Rq}-\gamma_T)} \times e^{j2\pi t f_R^{max}\cos(\alpha_{Rq}-\gamma_R)-j\frac{2\pi}{\lambda}\epsilon_{pq}} \tag{1.54}$$

where the used distances are defined as

$$\epsilon_{pm} \approx R_T - (0.5\mathcal{A}_T + 0.5 - p)\delta_T \cos(\alpha_T^m - \theta_T) \tag{1.55}$$

$$\epsilon_{mq} \approx D - (0.5\mathcal{A}_R + 0.5 - q)\delta_R[\Delta_T \sin\theta_R \sin\alpha_T^m - \cos\theta_R] \tag{1.56}$$

$$\epsilon_{pn} \approx D - (0.5\mathcal{A}_T + 0.5 - p)\delta_T[\Delta_R \sin\theta_T \sin\alpha_R^n + \cos\theta_T] \tag{1.57}$$

$$\epsilon_{nq} \approx R_R - (0.5\mathcal{A}_R + 0.5 - q)\delta_R \cos(\alpha_R^n - \theta_R) \tag{1.58}$$

$$\epsilon_{mn} \approx \epsilon_{pq} \approx D \tag{1.59}$$

$$\epsilon_{mq} \approx D - (0.5\mathcal{A}_R + 0.5 - q)\delta_R \cos\alpha_{Rq}^{LOS}\theta_R - (0.5\mathcal{A}_T + 0.5 - q)\delta_T \cos\theta_T, \tag{1.60}$$

and parameters p and q take values from the sets $p \in \{1, \ldots, \mathcal{A}_T\}$ and $q \in \{1, \ldots, \mathcal{A}_R\}$, respectively. The weights $\eta_{SBT}, \eta_{SBR}, \eta_{DB}$ show how much the single- and double-bounced rays contribute in the total power, i.e. these parameters satisfy $\eta_{SBT} + \eta_{SBR} + \eta_{DB} = 1$. It is assumed that the AoD $\alpha_T^{n(m)}$ and the AoA $\alpha_R^{n(m)}$ are random variables. Note that double-bounced rays have the AoD, α_T^m , independent from the AoA, α_R^n whereas single-bounced rays have the AoA, α_R^m dependent on the AoD α_T^m, and the AoD α_T^n dependent on the AoA α_R^n. Frequencies $f_T^{max} = v_T/\lambda$ and $f_R^{max} = v_R/\lambda$ are the maximum Doppler frequencies of the Tx and Rx, respectively, and λ is the carrier wavelength. Finally, it is assumed that the phases $\phi_n, \phi_m, \phi_{nm}$ are random variables uniformly distributed on the interval $[\pi, \pi)$ and independent from the angles of departure and the angles of arrival.

From the geometrical model described above, the received complex faded envelope of the link $A_T^p - A_R^q$ is a superposition of the single-bounced transmit, single-bounced receive, the double-bounced rays, and the LoS and can be written as follows

$$g^{pq} = g_{SBT}^{pq} + g_{SBR}^{pq} + g_{DB}^{pq} + g_{LOS}^{pq} \tag{1.61}$$

Correlation functions of the components (1.51)–(1.54) can be expressed as [58]

$$R_{DB}^{pq,\tilde{p}\tilde{q}}(\delta_T, \delta_R, \tau) = \eta_{DB} \frac{I_0\left(\sqrt{x_{DB}^2 + y_{DB}^2}\right) I_0\left(\sqrt{z_{DB}^2 + w_{DB}^2}\right)}{I_0(k_T) I_0(k_R)} \tag{1.62}$$

$$\begin{aligned} R_{SBT}^{pq,\tilde{p}\tilde{q}}(\delta_T, \delta_R, \tau) &= \eta_{SBT} e^{-j\frac{2\pi}{\lambda}(\tilde{q}-q)\delta_R \cos\theta_R + j2\pi\tau f_R^{max}\cos\gamma_R} \\ &\times \frac{I_0\left(\sqrt{x_{SBT}^2 + y_{SBT}^2}\right)}{I_0(k_T)} \end{aligned} \tag{1.63}$$

$$\begin{aligned} R_{SBR}^{pq,\tilde{p}\tilde{q}}(\delta_T, \delta_R, \tau) &= \eta_{SBR} e^{-j\frac{2\pi}{\lambda}(\tilde{p}-p)\delta_T \cos\theta_T + j2\pi\tau f_T^{max}\cos\gamma_T} \\ &\times \frac{I_0\left(\sqrt{x_{SBR}^2 + y_{SBR}^2}\right)}{I_0(k_R)} \end{aligned} \tag{1.64}$$

$$\begin{aligned} R_{LOS}^{pq,\tilde{p}\tilde{q}}(\delta_T, \delta_R, \tau) &\approx \sqrt{K_{pq} K_{\tilde{p}\tilde{q}}} e^{j\frac{2\pi}{\lambda}\delta_T \cos\theta_T - j\frac{2\pi}{\lambda}\delta_R \cos\theta_R} \\ &\times e^{j2\pi\tau f_T^{max}\cos\gamma_T - j2\pi\tau f_R^{max}\cos\gamma_R} \end{aligned} \tag{1.65}$$

where

$$x_{DB} = j\frac{2\pi}{\lambda}(\tilde{p}-p)\delta_T \cos\theta_T - j2\pi\tau f_T^{max}\cos\gamma_T + k_T \cos\mu_T$$

$$y_{DB} = j\frac{2\pi}{\lambda}(\tilde{p}-p)\delta_T \sin\theta_T - j2\pi\tau f_T^{max}\sin\gamma_T + k_T \sin\mu_T$$

$$z_{DB} = j\frac{2\pi}{\lambda}(\tilde{q}-q)\delta_R \cos\theta_R - j2\pi\tau f_R^{max}\cos\gamma_R + k_R \cos\mu_R$$

$$w_{DB} = j\frac{2\pi}{\lambda}(\tilde{q}-q)\delta_R \sin\theta_R - j2\pi\tau f_R^{max}\sin\gamma_R + k_R \sin\mu_R$$

$$\begin{aligned} y_{SBT} &= j\frac{2\pi}{\lambda}((\tilde{p}-p)\delta_T \sin\theta_T + (\tilde{q}-q)\delta_R \Delta_T \sin\theta_R) \\ &- j2\pi\tau(f_T^{max}\sin\gamma_T + f_R^{max}\Delta_T \sin\gamma_R) + k_T \sin\mu_T \end{aligned}$$

$$\begin{aligned} y_{SBR} &= j\frac{2\pi}{\lambda}((\tilde{p}-p)\delta_T \Delta_R \sin\theta_T + (\tilde{q}-q)\delta_R \sin\theta_R) \\ &- j2\pi\tau(f_T^{max}\Delta_R \sin\gamma_T + f_R^{max}\sin\gamma_R) + k_R \sin\mu_R \end{aligned}$$

$$x_{SBT} = x_{DB}$$

$$x_{SBR} = z_{DB}$$

In [58] it is shown that the normalized space-time correlation function between two complex faded envelopes $g^{pq}(t)$ and $g^{\tilde{p}\tilde{q}}(t)$ is defined as

$$\begin{aligned} R^{pq,\tilde{p}\tilde{q}}(\delta_T,\delta_R,\tau) = R_{DB}^{pq,\tilde{p}\tilde{q}}(\delta_T,\delta_R,\tau) + R_{SBT}^{pq,\tilde{p}\tilde{q}}(\delta_T,\delta_R,\tau) \\ + R_{SBR}^{pq,\tilde{p}\tilde{q}}(\delta_T,\delta_R,\tau) + R_{LOS}^{pq,\tilde{p}\tilde{q}}(\delta_T,\delta_R,\tau). \end{aligned} \tag{1.66}$$

Many existing correlation functions are special cases of the MIMO space-time correlation function in (1.66) including all ones described previously in the chapter and published in [56, 59, 55, 60, 61].

1.6 Wideband Channel Modeling

The Room Electromagnetics (REM) theory has been developed in [62] in analogy with the well-known theory of room acoustics [63]. Here, we will briefly introduce some concepts of the room electromagnetic theory for room-to-room communication because Chapter 5 this scenario is investigated. Basically, the REM describes the PDP in indoor environments as a superposition of two parts: a LOS component (if present) and the rest, which is composed of the diffuse multipath components. It is supposed that the (weak) specular contributions are neglected in the dense multipath components. This assumption is supported by experimental observations where the contribution of the diffuse fields in the total power was 90% or more[64, 65].

Let us assume a transceiver located at a given position in an indoor environment. If a signal pulse is transmitted in the room and turned off after a short time $t > 0$, the receiver records first the strongest path, typically the line-of-sight (LOS) component if present. Afterwards, few specular paths due to reflections off the walls, ceiling, or floor arrive at the receiver. For a given position of the transceiver, the specular paths - LOS included - arrive at the receiver side with incident angles characterized by an elevation angle Θ_{Rx} and an azimuth ϕ_{Rx}, which are dependent on the transceiver's position and the room layout's. Since the specular paths arrive at the receiver within certain favored directions, they do not contribute to the establishment of the diffuse fields, but rather consists of what is called here the primary components. During this transient state, energy is not uniform in the room as the specular paths contribution in terms of energy density differs from one direction to another one [66]. Besides the specular reflections, there are also propagation phenomena such as scattering and/or diffraction that establish the diffuse fields. Few specular paths stemming from consecutive random reflections may also favor the rise of diffuse fields. The transient and the reverberant state are shown in Figure 1.10 and the corresponding powers are denoted as primary and reverberant components, respectively. τ_0 is the arrival delay of the first or strongest component and τ_l is the end (respectively beginning) of the primary (respectively reverberant) component. The power delay spectrum (or mean PDP) is the superposition of both the primary and reverberant component and is expressed as follows:

$$PDP = PDP_{pri} + PDP_{rev} \tag{1.67}$$

In dB-scale, the reverberant part is characterized by the slope of the PDP's tail (Figure 1.10), and is independent on the transceivers' location. However, the primary part depends of the location of the transceiver. For instance, for a short (resp. long) Tx-Rx

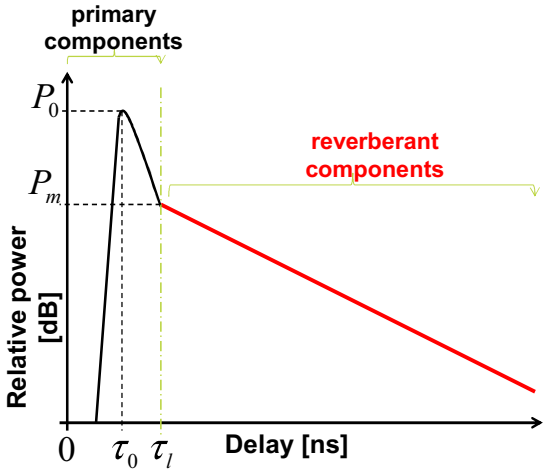

Figure 1.10: Modeling of the PDP in a reverberant environment.

separation, the transient state will last longer (resp. shorter) than if the Tx-Rx distance was longer (resp. shorter). Moreover, the transceiver's location will influence the power level of the primary components, which consists of the LOS if present and a number of specular reflections. Consequently, if the node is mobile, then the primary component's power fluctuates over time (i.e. it is influenced by different types of fading). However, when the PDP is averaged over the measurement's duration we obtain a static power level of the Primary components.

1.6.1 Modeling of the Primary Components

The existence of primary components in indoor environments is well acknowledged in the literature [67, 68, 69, 70]. However, the primary component is usually modeled as a delta function, i.e., only one specular component:

$$PDP_{pri}(\tau_0) = P_0(\tau_0)^{\eta}\delta(\tau - \tau_0) \tag{1.68}$$

where $P_0(\tau_0)$ is the power of the primary or strongest component arriving with a delay τ_0, and n is the path-loss exponent. Parameter η is determined by fitting the experimental path gain obtained at different Tx-Rx distances.

The delta function is an approximation of the primary component. This primary component model fits better for longer Tx-Rx separation, than shorter ones. This is confirmed by several experimental measurements in indoor environments [71, 72, 70] and simulations [73] where the contribution of the primary component in the total power becomes negligible for larger Tx-Rx separation. However, when the transience last longer, i.e., for shorter Tx-Rx separations, we model here the primary components with a set of delta functions:

$$PDP_{pri}(\tau_0) = \sum_{m=0}^{M} P_0(c_0\tau_0 + mc_0\tau_c)^{\eta}\delta(\tau - \tau_0 - m\tau_c), \tag{1.69}$$

where M and τ_c are respectively the reflection order and the characteristic time-delay that is required before a given ray makes one reflection in the room [74]. It has been shown that a ray undergoing m reflection(s) off the surfaces before arriving at the receiver has an arrival delay of $\tau = m\tau_c$, where τ_c depends only on the dimensions of the room and is expressed as [74]:

$$\tau_c = \frac{8V}{c_0 \mathcal{S}} \tag{1.70}$$

where V, $\mathcal{S}$, c_0 are the room volume, the total surface area of the room, and the speed of light in free space.

In the model we consider reflections up to the second order, i.e., the primary component consists of the LOS component, the first and second order reflected paths. The average power of a ray bouncing m time(s) ($m \in \{0, 1, 2\}$) is approximated by the free-space gain equation:

$$P_0(d_0 + mc_0\tau_c)^\eta = N\frac{a^m}{(d_0 + mc_0\tau_c)^\eta} \tag{1.71}$$

where N is a constant depending on antenna properties, frequency, and transmitted power, and a is the average reflection coefficient of the wall surfaces.

1.6.2 Modeling of the Reverberant Component

The modeling of the reverberant component is straightforward and based on the room electromagnetic theory [75], [69]. The reverberation time of the considered room, and the power corresponding to the beginning of the reverberant components (P_m in Figure 1.10) are the required parameters to model the reverberant component. An empirical formula to determine the reverberation time as a function of the frequency is derived in [75] and can be used to assess the reverberation time without resorting to measurements. However, in this thesis, we consider a room-to-room wideband scenario. The expressions of the reverberation time for in-room and room-to-room communications are derived in [72].
The power level P_m shown in Figure 1.10 is the same as the primary component at $\tau = \tau_l$, since there is no discontinuity in the PDP:

$$P_m = PDP_{pri}(\tau_l). \tag{1.72}$$

If we include the time-delay dependency in the model, the reverberant component is given by [67, 68, 69]:

$$\begin{aligned} PDP_{rev}(\tau) &= P_m e^{-\frac{(\tau-\tau_l)}{\tau_r}} \quad \text{if } \tau \geq \tau_l, \\ &= 0 \qquad\qquad\quad \text{otherwise} \end{aligned} \tag{1.73}$$

where τ_r is the reverberation time of the environment. The reverberation time is the decay rate of the diffuse energy and has been experimentally and numerically investigated in various studies [68, 73, 72, 69]. The reverberation time for an in-room

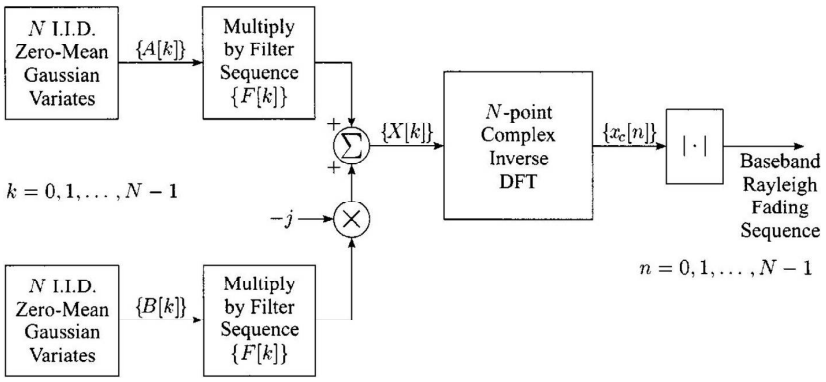

Figure 1.11: Young's model [78]

scenario can be determined via the following expression [75]:

$$\tau_r(f) = \frac{V}{2\pi f \mathcal{S}}\big(0.473f^3 - 24.9f^2 + 321f - 254\big), \tag{1.74}$$

$$= \frac{4V}{b(f)c_0\mathcal{S}} \tag{1.75}$$

where τ_r and $2 < f < 10$ are the reverberation time (ns) and the frequency (GHz), respectively; $b(f)$ is the average fraction of the energy absorbed by the surfaces in the room at the frequency f. Once the reverberation time for in-room scenario is determined, its value for the adjacent room scenario (room-to-room) is determined by [72]:

$$\tau_{r,ajc} = \frac{\tau_r}{1 - \frac{c_0\tau_r\mathcal{S}_{12}}{4V}}, \tag{1.76}$$

where $\tau_{r,ajc}$, τ_r, and $\mathcal{S}_{12}$ are the reverberation time in adjacent room (i.e., the Tx and the Rx are in adjacent rooms), the reverberation time when the transceivers are in the same room (in-room scenario), and the surface of the wall separating the adjacent rooms, respectively. The average fraction of absorbed energy (hence the average reflection coefficient, i.e., $a = 1 - b$) is further determined from (1.75).

1.7 Simulation Models for Fading Channels

Simulation of fading channels is commonly used as opposed to field trials, because it allows for less expensive and more reproducible system tests and evaluations. There are several different methods for channel simulation. The most widely accepted methods are filtered noise models [76, 77, 78] and sum-of-sinusoids (SoS) models [49, 50, 59, 54, 56, 58].

1.7.1 Filtered Noise Simulation Model

In [78] Young and Beaulieu proposed a method based on the inverse discrete Fourier transform (IDFT). It is a modification of the Smiths algorithm [76] which was widely

used for Rayleigh fading simulation. This method requires exactly one-half the number of IDFT operations and roughly two-thirds the computer memory of the original method.

Rayleigh Fading can be simulated by adding two Gaussian Random variables. The effect of Doppler shift is incorporated by modeling the Doppler effect as a frequency domain filter. The model proposed by Young et.al is shown in Figure 1.11[78].

The combined effect of Doppler shift and fading is simulated by multiplying the Gaussian Random variables and the Doppler Shifts Frequency domain representation. Then IDFT is performed to bring them into time domain representation. The Doppler Filter used to represent the Doppler Shift effect. The equation for the Doppler Filter is

$$F_M[k] = \begin{cases} 0, & k = 0 \\ \sqrt{\frac{1}{2\sqrt{1-(\frac{k}{Nf^{max}})^2}}}, & k = 1, 2, \ldots, k_m - 1 \\ \sqrt{\frac{k_m}{2}\left[\frac{\pi}{2} - \arctan\left(\frac{k_m - 1}{\sqrt{2k_m - 1}}\right)\right]}, & k = k_m \\ 0, & k = k_m + 1, \ldots, N - k_m - 1 \\ \sqrt{\frac{k_m}{2}\left[\frac{\pi}{2} - \arctan\left(\frac{k_m - 1}{\sqrt{2k_m - 1}}\right)\right]}, & k = N - k_m \\ \sqrt{\frac{1}{2\sqrt{1-(\frac{N-k}{Nf^{max}})^2}}}, & k = N - k_m + 1, \ldots, N - 2, N - 1 \end{cases} \tag{1.77}$$

1.7.2 Sum of Sinusoids Simulation Model

The reference model for MIMO double mobile channels described in Section 1.5.2 assumes an infinite number of scatterers, which prevents practical implementation. It is desirable to design simulation models with a finite number of scatterers, while still matching the statistical properties of the reference model. Hence, in [58] Zajic et. al proposed a simulation model where the complex faded envelope is designed as a superposition of the LoS, the single-bounced, and the double-bounced rays. Assuming 2-D isotropic scattering and using the reference model described in Section 1.5.2, the following function was proposed as a received complex faded envelope: $g^{pq}(t) = g_I^{pq}(t) + g_Q^{pq}(t) = \Re(g^{pq}(t)) + \Im(g^{pq}(t))$ where

$$
\begin{aligned}
g_I^{pq}(t) &= \sum_{m=1}^{M} \frac{2P_T}{\sqrt{M}} \cos\left[\beta_m - K_q \cos\theta_R - 2\pi t f_R^{max} \cos\gamma_R\right] \\
&\times \cos\Bigg[K_p \cos\left(\theta_T - \alpha_T^m\right) + 2\pi t f_T^{max} \cos\left(\alpha_T^m - \gamma_T\right) \\
&+ K_q \Delta_T \sin\theta_R \sin\alpha_T^m + 2\pi t f_R^{max} \Delta_T \sin\gamma_R \sin\alpha_T^m + \phi_m\Bigg] \\
&\sum_{n=1}^{N} \frac{2P_R}{\sqrt{N}} \cos\left[\beta_n + K_p \cos\theta_T - 2\pi t f_T^{max} \cos\gamma_T\right] \\
&\times \cos\Bigg[K_q \cos\left(\alpha_R^n - \theta_R\right) + 2\pi t f_R^{max} \cos\left(\alpha_R^n - \gamma_R\right) \\
&+ K_p \Delta_R \sin\theta_T \sin\alpha_R^n + 2\pi t f_T^{max} \Delta_R \sin\gamma_T \sin\alpha_R^n + \phi_n\Bigg] \\
&\sum_{m,n=1}^{MN} \frac{2P_{TR}}{\sqrt{MN}} \cos\Bigg[K_p \cos\left(\theta_T - \alpha_T^m\right) + 2\pi t f_T^{max} \cos\left(\alpha_T^m - \gamma_T\right)\Bigg] \\
&\times \cos\Bigg[K_q \cos\left(\alpha_R^n - \theta_R\right) + 2\pi t f_R^{max} \cos\left(\alpha_R^n - \gamma_R\right) + \phi_n\Bigg] \\
&+ P_{LOS} \cos\Bigg[K_p \cos\theta_T + K_q \cos\left(\alpha_{Rq}^{LOS} - \theta_R\right) + 2\pi t \left(f_t^{LOS} + f_R^{LOS}\right)\Bigg]
\end{aligned}
\tag{1.78}
$$

$$
\begin{aligned}
g_Q^{pq}(t) &= \sum_{m=1}^{M} \frac{2P_T}{\sqrt{M}} \sin\left[\beta_m - K_q \cos\theta_R - 2\pi t f_R^{max} \cos\gamma_R\right] \\
&\times \cos\Bigg[K_p \sin\left(\theta_T - \alpha_T^m\right) + 2\pi t f_T^{max} \sin\left(\alpha_T^m - \gamma_T\right) \\
&+ K_q \Delta_T \sin\theta_R \cos\alpha_T^m + 2\pi t f_R^{max} \Delta_T \sin\gamma_R \cos\alpha_T^m + \phi_m\Bigg] \\
&\sum_{n=1}^{N} \frac{2P_R}{\sqrt{N}} \sin\left[\beta_n + K_p \cos\theta_T - 2\pi t f_T^{max} \cos\gamma_T\right] \\
&\times \cos\Bigg[K_q \sin\left(\alpha_R^n - \theta_R\right) + 2\pi t f_R^{max} \sin\left(\alpha_R^n - \gamma_R\right) \\
&+ K_p \Delta_R \sin\theta_T \cos\alpha_R^n + 2\pi t f_T^{max} \Delta_R \sin\gamma_T \cos\alpha_R^n + \phi_n\Bigg] \\
&\sum_{m,n=1}^{MN} \frac{2P_{TR}}{\sqrt{MN}} \sin\left[K_p \cos\left(\theta_T - \alpha_T^m\right) + 2\pi t f_T^{max} \cos\left(\alpha_T^m - \gamma_T\right)\right] \\
&\times \sin\left[K_q \sin\left(\alpha_R^n - \theta_R\right) + 2\pi t f_R^{max} \sin\left(\alpha_R^n - \gamma_R\right) + \phi_{mn}\right] \\
&+ P_{LOS} \cos\left[K_p \sin\theta_T + K_q \cos\left(\alpha_{Rq}^{LOS} - \theta_R\right) + 2\pi t \left(f_t^{LOS} + f_R^{LOS}\right)\right]
\end{aligned}
\tag{1.79}
$$

By allowing amplitudes, phases, and Doppler frequencies to be random variables, the proposed deterministic model can be modified to match statistical properties of

the reference model over a wider range of normalized time delays, while at the same time requiring a smaller number of scatterers around the Tx and Rx. The statistical properties of this model vary for each simulation trial, but will converge to desired ensemble averaged properties when averaged over a sufficient number of simulation trials. The complex faded envelope is $g^{pq}(t) = g_I^{pq}(t) + g_Q^{pq}(t)$, where functions $g_I^{pq}(t)$ and $g_Q^{pq}(t)$ are defined as in in (1.78) and (1.79), respectively. The angles of departures and the angles of arrivals are chosen as follows:

$$\alpha_T^m = 0.5\left(\frac{2\pi m}{M} + \frac{\psi - \pi}{M}\right) \tag{1.80}$$

$$\alpha_R^n = \frac{2\pi n}{N} + \frac{\theta - \pi}{N} \tag{1.81}$$

for $m = 1, \ldots, M, n = 1, \ldots, N$, respectively. The parameters $\phi_{mn}, \beta_m, \beta_n, \theta$ and ψ are independent random variables uniformly distributed on the interval $[\pi, \pi)$.

1.8 Outline and Contributions

This thesis develops innovative modeling approaches for dynamic indoor radio channels. Given the complexity of the global channel, various aspects have been investigated separately, based on different measurement campaigns at 3.8 GHz. However, all these models share the same formalism and can be thought as extensions of a reference narrowband representation. The contributions address therefore

- the non-stationary dynamics of narrowband channels: the new methodology combines an accurate composite fading distribution with a new shadowing model and a Markov chain approach to account for non-stationarity,
- the MIMO channel dynamics, highlighting the temporal variations of the directional behavior of the channel, linking these with the narrowband fading statistics investigated earlier,
- the wideband channel dynamics, relying on an original hybrid model extending the narrowband model by means of the room electromagnetics theory.

Furthermore, all models have been experimentally validated.

These contributions are organized into several chapters. Chapter 2 describes the radio channel measurement system called Elektrobit Channel Sounder that was used in the thesis. The main function of the system and necessary procedures are described and explained. Next, popular high resolution algorithms used to estimate the channel are discussed. One of the most successful algorithms (Space-Alternating Generalized Expectation-maximization (SAGE)) is described in details. This chapter also contains a description of the used antennas.

Narrowband indoor peer-to-peer channels are investigated in Chapter 3 based on a wideband experimental campaign at 3.8 GHz in a typical office environment consisting of different rooms aligned along corridor and separated by walls of different types. Variations of small-scale fading statistics are analyzed and modeled using the

SOSF distribution. In addition, second-order statistics are derived using a double-ring model. The resulting implementation of a time-series generator of channel realizations is a combination of empirical first-order statistics and geometry-based channel dynamics. To model the sudden changes of fading statistics, we introduce a three-step approach: (i) for reflecting the sudden changes of the statistics, we define and parameterize a hidden Markov model [79], (ii) the parameters of the SOSF distribution are modeled according to a Beta or an Extreme Value distribution, fitting the measurements, (iii) fading realizations are generated [78]. Path-loss and Large-Scale fading models extracted from the measurements are also presented.

In Chapter 4, we investigate narrowband MIMO channels based on a wideband measurement campaign. The investigated environment is similar to the one described in the previous chapter, but the measurement campaign was performed in another building. This chapter contains a description of the procedure used to define the stationarity period, which later is used to extract SOSF parameters from measured MIMO channels as well as directional statistics. We analyze and model the variations of first order small-scale fading statistics using the HMM based approach presented in Chapter 3. A measurement-based model of Angular Power Spectra is proposed. Geometry based reference and simulation models for MIMO SOSF channels are presented and later used to derive appropriate spatial correlation functions. The chapter contains descriptions of the path-loss and large-scale simulation models.

A physical-statistical technique combining the Room Electromagnetic (REM) Theory for modeling deterministic channel components with a geometry based stochastic channel model with time-variant statistics for modeling stochastic channel components is proposed in Chapter 5. The model is based on a wideband measurement campaign where the nodes were located in two adjacent rooms. The method enables the reconstruction of the PDP in a room-to-room dynamic scenario, including effects introduced by the mobility of the communication nodes. The prediction of the specular reflections is improved since the motion of the transceivers is accounted for. The combination of extracted first- and second-order statistics enables to implement a channel impulse response (CIR) generator. To model the sudden changes of fading statistics, we use a three-step approach presented earlier in Chapters 3 and 4. A model for large scale variations of the CIR is proposed.

Chapter 2

Channel Sounding and Parameter Estimation

The measurement technique used to estimate the propagation channel properties is called channel sounding. The name stems from a transmitter that "sounds" (or excites) the channel, whereas the receiver records the channel output. The complexity of the channel sounders increases according to their applications and measured scenarios. On the one side, directional channel properties are of interest for multiple antenna systems while wideband wireless systems necessitate delay dispersion measurements of the channel. On the other side, applications of channel sounding have been evolving towards being able to measure the channel for more specific and complex environments such as as indoor, industrial (metallic objects) and inter-vehicular environments.

Stochastic channel models are based on measurements of the wireless propagation channel where parameters of the channel models are extracted from the measured data. The wireless propagation channel can be measured in the time or frequency domain. In time domain measurements, the channel is first excited with pulses or Pseudo Noise (PN) sequences generated deterministically and then the channel impulse response $h(t, \tau)$ is calculated. The PN sequence normally has a good time-bandwidth product and each element is named as chip. On the other hand, frequency domain measurements acquire the transfer function $H(t, f)$ by using a chirp signal (frequency increase or decrease with time) or a multi-tone signal (flat spectrum and low peak-average ratios) to sound the channel.

The synchronization between Tx and Rx units is crucial for channel measurements. Frequency offset between local oscillators can cause phase rotation. Consequently, the IR delay can be shifted. To overcome this issue, two units can be connected with coaxial or fiber-optic cables to send a synchronization signal. However, it is only possible for short range measurements, e.g., indoor scenario. Therefore, atomic clocks are usually employed in the sounding equipment to keep them synchronized for long range measurements. The synchronization of both units can be done at the beginning of the measurement campaign.

The band-limited time-invariant measurements can be performed by sampling channel at Nyquist rate such that:

- The period T_{rep}, with which the periodic pulses are sent by the Tx unit repeatedly, must be shorter than the coherence time of the channel

$$T_{rep} \leq \frac{1}{2\nu_{max}} \tag{2.1}$$

  where ν_{max} is the maximum Doppler frequency.

- T_{rep} should be greater than the maximum excess delay of the channel in order to avoid overlap between consecutive sounding signals

$$T_{rep} \geq \tau_{max} \tag{2.2}$$

These two conditions jointly give the equation for the two-dimensional Nyquist criterion

$$2\nu_{max}\tau_{max} \leq 1 \tag{2.3}$$

If this criterion is satisfied, the channel under investigation is said to be underspread.

Similarly, for MIMO channels measurements, some specific conditions needs to be fulfilled: the channel responses for all possible combinations of Tx and Rx antenna elements have to be measured in MIMO channels. For this purpose, following three techniques can be applied

- Real arrays: each array has its own RF chain, the channel can be measured simultaneously at different receiver elements. However, this costly approach requires a complex calibration procedure.

- Switched arrays: only requires one RF chain at the Rx. Fast RF switches control the switching between different Tx and Rx elements, such that only one antenna pair is measured at a time.

- Virtual arrays: a single antenna at each side of the link, MIMO measurements can be performed by mechanically moving the antenna to predetermined positions.

2.1 The Elektrobit Channel Sounder

The Elektrobit channel sounder is a radio channel measurement system operated at a carrier frequency range of 3.4 to 4.2 GHz and based on the switched array principle [2]. It mainly consists of two units, a Tx unit and a Rx unit, as shown in Figure 2.1. The Rx unit is further connected to the Data Acquisition (DAQ) module. A user controls the measurements and changes the settings at the Tx or Rx unit according to the goal by using Real Time Control Software (RTCS). It is accessed through a control notebook connected to each unit with a Local Area Network (LAN) cable. The Elektrobit channel sounder transmits and receives a PN sequence to determine the channel IR. The Tx generates a PN sequence, modulates and up-converts to the desired center frequency. Conversely, the received signal is down-converted at the Rx side and demodulated into I/Q format.

An important concept of the channel sounder is the timing, where a chip is basic unit represents one symbol of a code. The chip rate controls the timing such that

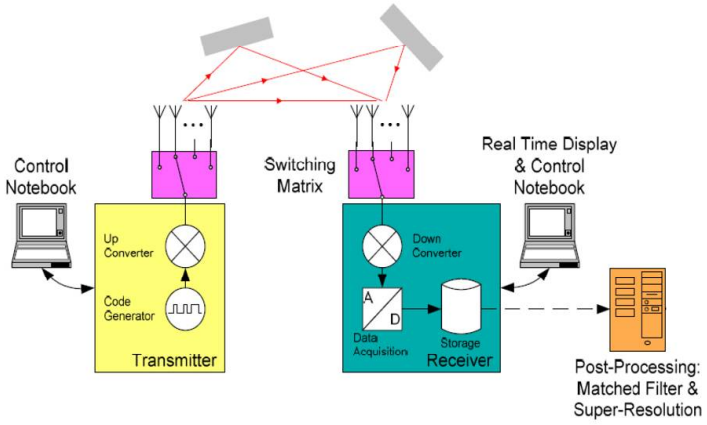

Figure 2.1: Block diagram of the Elektrobit channel sounder [2]

higher chip rate achieves better delay resolution of the IR. The delay resolution (τ_r) can be expressed as

$$\tau_r = \frac{1}{f_{ch} \cdot N_{sc}}, \tag{2.4}$$

where N_{sc} is the number of samples per chip and $f_{ch} = B/2$ (B is the bandwidth). A transmission code consisting of several chips must shorter than the time for which the channel can be considered static (i.e. the Doppler period) but longer than the maximum measurable delay in the propagation scenario. The dynamic range can be improved due to the fact that long codes provide processing gain. The measurable excess delay (τ_e) is

$$\tau_e = \frac{N_{ch}}{f_{ch}}, \tag{2.5}$$

where N_{ch} is the code length in chips. Each Tx antenna transmits a number of codes equal to the receive antennas and a guard code required for moving the Tx switch to the next antenna, thus total number of codes for each acquisition cycle are $N_{co} = \mathcal{A}_T(\mathcal{A}_R + 1)$. Figure 2.2 shows the described switching principle. The fast switches of each unit, connected to multiple antennas, enable the channel sounder for MIMO measurements. Once all the Tx and Rx antennas are scanned, the acquisition cycle is accomplished. In addition, Doppler frequency of the time-variant channel has to be sampled according to Nyquist criterion, therefore, the minimum channel sampling rate is expressed as

$$f_{cs} = \frac{v_m + 2v_s}{\lambda} N_\lambda, \tag{2.6}$$

where v_m is the maximum speed of the mobile terminal, v_s is the maximum speed of the scatterers and N_λ is the number of wished channels per wavelength. In a high Doppler frequency scenario, the cycles can be measured in bursts mode. In this mode, where cycles are measured for a certain time, and then data is stored on the disk for rest of the time, without taking measurements.

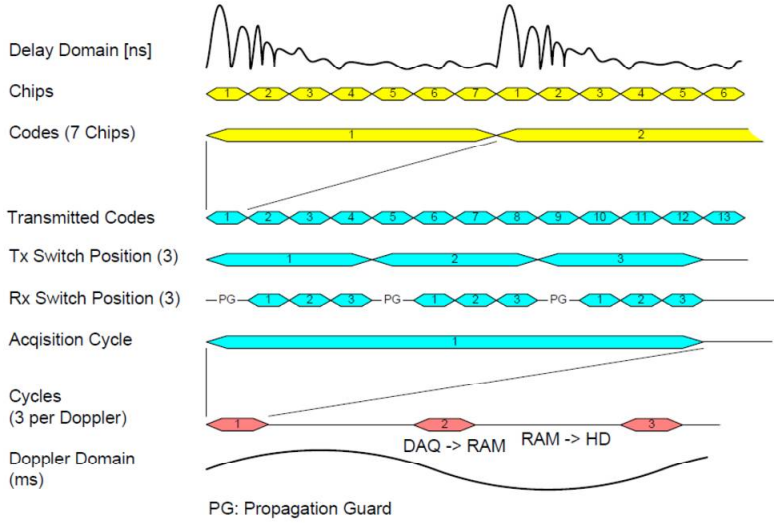

Figure 2.2: Timing concept[2]

The synchronization of local oscillators at the Tx and Rx employing Rubidium clocks is critical in measurement campaigns. Even a small frequency offset can lead to phase rotation (Doppler) and sliding of the delay. To synchronize the sounder the following two steps must be performed:

- the clock synchronization, where the relative phase rotation is minimized by tuning the Rubidium clocks,

- the time tag synchronization, where a common absolute time reference is allocated to both units.

In order to compensate the system and cable losses, a calibration measurement before the data acquisition is essential. Actually, it is measurement of a well-defined channel, usually an attenuator of a certain attenuation which is back-to-back connected to both units through RF cables. After successful synchronization and calibration measurement, two units can be moved without external power supply after putting on Clock Keep Alive (CKA) mode. Inputs parameters or sounder settings can be adjusted with the help of ”Setup Wizard” in the controlling laptop. The range of input parameters to be defined before measurements is provided in Table 2.1. While different methods can be used to identify measurement locations, the Elektrobit channel sounder has capability to store the location of the Rx by Global Positioning System (GPS) together with the measured data stream (time-tagged), when GPS coverage is available.

Table 2.1: The range of channel sounder parameters to be defined before a measurement campaign

Parameter	Range
Center frequency	3.4 to 4.2 GHz
Transmit power	23 dBm (default value)
Bandwidth	1.563 to 200 MHz
No of samples per chip	1 to 10
Max. path length	min.code length chips
Channel sampling rate	0.011 to 1358.911
Max. mobile speed	min.channel sampling rate
Tx antennas	1 to 8
Rx antennas	1 to 8

2.2 Parameter Estimation with High Resolution Algorithms

A detailed knowledge of delay, angle and Doppler characteristics of channels are necessary for the development of MIMO systems that employ diversity multiplexing techniques. For this reason, signal processing techniques have been developed or adapted to estimate those propagation parameters from measurement campaigns.

An important issue is that channel measurements need to yield enough resolution in the specific parameters of interest. The most interesting case concerns directional information, i.e. the employment of arrays of antennas. The following three array techniques mentioned above can be used [24]: (i) real arrays, (ii) multiplexed arrays and (iii) virtual arrays. If a system with N receiving antennas is considered, it is necessary that during the acquisition of N measurements the propagation environment could be considered static. In real arrays, measurements are done simultaneously, at the cost of a complex architecture. With virtual arrays only measurements in static environments are possible as the time employed to mechanically scan all the array positions is much larger than the coherence time of any time-variant channel. Multiplexing arrays are a trade-off between complexity and velocity of acquisition.

The most successful high resolution algorithm is probably SAGE [80], a maximum-likelihood based estimator which is able to extract from measurement the joint angular-delay-Doppler characteristics of propagation paths as well as their polarization matrix. Another advantage of this method is the capability to work also with contributions with small amplitude. The output information of SAGE high resolution algorithm for each ray are:(i) delay of arrival τ, (ii) azimuth of departure φ_d, (iii) azimuth of arrival φ_a.

RIMAX [81] is another maximum likelihood estimator with the advantage of jointly evaluating specular and diffuse component parameters and that is also able to inherently provide the variance of the parameters as measure of their reliability.

SAGE algorithm was later implemented by Elektrobit (so-called Initialization and Search Improved SAGE (ISIS)) [82]. In multi-antenna channel characterization the ISIS software enables the estimation of e.g. the following characteristics of the double-directional wideband radio channel:

1. Number of significant propagation paths

Figure 2.3: Elektrobit channel sounder

2. Doppler frequency
3. Propagation delays
4. Power delay profiles
5. Angle of arrival at the receiver in both elevation and azimuth
6. Angle of departure at the transmitter in both elevation and azimuth
7. Polarization matrix of the propagation paths
8. Rotation direction of polarization

2.2.1 SAGE Algorithm

Signal model

Let us assume a MIMO channel sounder measurement where the transmitted signal at each transmit antenna is the baseband signal $u(\tau)$. The contribution of the $l-$th MPC to the $\mathcal{A}_T \times \mathcal{A}_R$ samples from the transmit array to the receive array can be stacked in a $\mathcal{A}_R\mathcal{A}_T \times 1$ vector:

$$s(\tau, \Theta_l) = \mathbf{vec}\{C_r(\Omega_{r,l})\gamma_l C_t(\Omega_{t,l}^T)u(\tau - \tau_l)\} \tag{2.7}$$

where $\Theta_l = [\Omega_{r,l}, \Omega_{t,l}, \tau_l, \gamma_l]$ is a vector containing the parameters of the $l-$th propagation path (directions of arrival, directions of departure, propagation delay and polarization rotation matrix of the $l-$th MPC respectively. The matrix $C_r(\Omega_{r,l})$ is a $\mathcal{A}_R \times 2$ matrix, where each column represents the response of the receive array in the Θ and the ϕ polarization in direction $\Omega_{r,l}$, and matrix $C_t(\Omega_{t,l})$ is a $\mathcal{A}_T \times 2$ matrix, where each column represents the response of the receive array in the Θ and the ϕ polarization in direction $\Omega_{t,l}$. The contribution of L MPCs is then given by:

$$s(\tau, \Theta) = \sum_{l=1}^{L} s(\tau, \Theta_l) \tag{2.8}$$

If the channel is composed of L MPCs, the total measured channel (stacked in a $\mathcal{A}_T\mathcal{A}_R \times 1$ vector) can be written:

$$y(\tau) = \sum_{l=1}^{L} s(\tau, \Theta_l) + \sqrt{\frac{N_0}{2}}\mathbf{N}(\tau) \tag{2.9}$$

where N_0 is the noise power and $\mathbf{N}(\tau)$ denotes $\mathcal{A}_T\mathcal{A}_R$-dimensional zero-mean unit-variance complex Gaussian noise vector.

Expectation-Maximization algorithm

The problem at hand is the estimation of the L parameter vectors Θ_l, given an observation $y(\tau)$ [82]. In practice, the number of MPCs L is fixed large enough to capture all significant MPCs (for example 20 in [83]). The log-likelihood function of $\Theta = [\Theta_1 \dots \Theta_l]$, for a certain observation $y(\tau)$ over an observation span T_0 is given by:

$$\Lambda(\Theta, y) \propto 2\int_{T_0} \mathcal{R}\{s^H(\tau, \Theta)y(\tau)\}dt - \int_{T_0} \|s(\tau, \Theta)\|^2 dt \tag{2.10}$$

The maximum likelihood estimate (MLE) of Θ is the value for which the log-likelihood function is maximum:

$$\hat{\Theta}_{ML}(y) = \arg\max\{\Lambda(\Theta, y)\} \tag{2.11}$$

In the case of MIMO propagation channels, the computation of $\hat{\Theta}_{ML}(y)$ is an ill-conditioned $5L-$dimensional optimization problem (L MPCs with 5 parameters per MPC to estimate). This becomes computationally prohibitive when L increases. An alternative approach must be considered to resolve the MLE problem.

The Expectation-Maximization (EM) algorithm is an iterative procedure for solving ML problems in case where part of the data is missing or censored [82]. If the superimposed signals can be assumed to be independent, then it can be used to determine superimposed signals corrupted by additive noise. The EM algorithm is based on the notion of complete (unobservable) and incomplete (observable) data. Observable data for one propagation path is given by:

$$x_l(\tau) = s(\tau, \Theta_l) + \sqrt{\zeta_l}\sqrt{\frac{N_0}{2}}\mathbf{N}(\tau) \tag{2.12}$$

where $\mathbf{N}(\tau)$ is a zero-mean unit-variance complex Gaussian noise and ζ_l is a real coefficient between 0 and 1, chosen so that $\{\sqrt{\zeta_1}\mathbf{N}_1(\tau), \ldots, \sqrt{\zeta_L}\mathbf{N}_L(\tau)\}$ forms a decomposition of $\mathbf{N}(\tau)$. The complete data is related to the observable data by:

$$y(\tau) = \sum_{l=1}^{L} x_l(\tau) \tag{2.13}$$

if $x_1(\tau), \ldots, x_L(\tau)$ are independent, the components $x_{\tilde{l}}(\tau)$, $\tilde{l} \neq l$ are irrelevant for the estimation of Θ_l. The log-likelihood function of Θ_l for the observable data $x_l(\tau)$ is then similar to (2.10) and given by:

$$\Lambda(\Theta, x_l) \propto 2\int_{T_0} \mathcal{R}\{s^H(\tau,\Theta)x_l(\tau)\}dt - \int_{T_0} \|s(\tau,\Theta)\|^2 dt \tag{2.14}$$

It is shown in [82] that, when inserting (2.7) and (2.8) in (2.14), the value of any propagation parameter($\Omega_{r,l}, \Omega_{t,l}, \tau_l$ or γ_l) that maximizes $\Lambda(\Theta, x_l)$ can be derived in a closed form as a function of the other propagation parameters. When substituting this value in $\Lambda(\Theta, x_l)$,the ML estimate is obtained as follows

$$(\hat{\Theta}_l)_{ML}(x_l) = \arg\max\{z(\Theta_l, x)\} \tag{2.15}$$

In these equation, $z(\Theta_l, x) = f(\Theta_l)^H D(\Omega_{r,l}, \Omega_{t,l})^{-1} f(\Theta_l)$ is the cost function, where $f(\Theta_l)$ is the unnormalized double-directional beamformer applied on x_l:

$$f(\Theta_l) = \begin{bmatrix} c^H_{r,\Theta}(\Omega_{r,l})\mathbf{X}_l(\tau_l)c_{t,\Theta}(\Omega_{r,l}) \\ c^H_{r,\Theta}(\Omega_{r,l})\mathbf{X}_l(\tau_l)c_{t,\phi}(\Omega_{r,l}) \\ c^H_{r,\phi}(\Omega_{r,l})\mathbf{X}_l(\tau_l)c_{t,\Theta}(\Omega_{r,l}) \\ c^H_{r,\pi}(\Omega_{r,l})\mathbf{X}_l(\tau_l)c_{t,\phi}(\Omega_{r,l}) \end{bmatrix} \tag{2.16}$$

In the above expression, $\mathbf{X}_l(\tau_l)$ is a $\mathcal{A}_R \times \mathcal{A}_T$ matrix. Each element of the matrix is defined as follows:

$$\mathbf{X}_{l,q,p}(\tau_l) = \int_{T_0} u^*(\tau - \tau_l)x_{l,q,p}(\tau)d\tau \tag{2.17}$$

where $x_{l,q,p}(\tau)$ is the $[(p-1)\cdot\mathcal{A}_R + q]-$th element of x_l, in other words the element corresponding to transmit antenna p and receive antenna q. The factors $D(\Omega_{r,l}, \Omega_{t,l})$ and P are the double-directional beamformer's normalization factors defined as

$$D(\Omega_{r,l}, \Omega_{t,l}) = \left[C_{r,\Theta}(\Omega_{r,l})^H\, C_{r,\Theta}(\Omega_{r,l})\right] \otimes \left[C_{t,\Theta}(\Omega_{t,l})^H\, C_{t,\Theta}(\Omega_{t,l})\right] \tag{2.18}$$

$$P = \int_{T_0} u(\tau)d\tau \tag{2.19}$$

The $5L-$dimensional optimization problem is thus reduced to L different 5-dimensional optimization problems (2.10),(2.14).

The remaining question is how the observable data $x_l(\tau)$ can be successfully estimated, based on the observation $y(\tau)$. An estimate of $\hat{x}_l(\tau, \hat{\Theta}')$ can be given by [82]:

$$\hat{x}_l(\tau, \hat{\Theta}'_l) = y(\tau) - \sum_{l'=1, l'\neq l}^{L} s(\tau, \hat{\Theta}'_{l'}) \tag{2.20}$$

It is clear from (2.20) that the observable data $x_l(\tau)$ for each MPC l is estimated by removing the current estimate of all other MPC from the observation data $y(\tau)$.

Equations (2.20) is usually referred as the Expectation (E) step and (2.15) as the Maximization (M) step. At each iteration, the observable data is estimated using on the latest parameter estimates (E step), and then the parameter estimates are updated (M-step). The remarkable property of the EM-algorithm is that the log-likelihood function cannot decrease because of the particular form of $\Lambda(\Theta, y)$. It can also be shown that the parameter estimate sequence will converge to a stationarity point if the initial guess of the parameter estimates is not too bad.

SAGE algorithm

The Space-Alternating Generalized EM (SAGE) algorithm is a slightly modified version of the EM algorithm. In the SAGE algorithm, subsets of the parameter estimates Θ_l can be estimated separately as long as the different parameters of the parameter space can be considered as independent. This makes possible to reduce the L 5-dimensional optimization problems (2.15) to $5L$ one-dimensional optimization problems.

In the SAGE algorithm, the following E-step and M-step are repeated iteratively for each MPC l, where Θ_l' represent the parameter estimate for MPC l before the iteration and Θ_l'' represent the parameter estimate for MPC l after the iteration:

- $E-step$: In the E-step, an estimation of the observable data is performed (2.20).
- $M-step$: The procedure for updating the parameter estimate from Θ_l' to Θ_l'' are decomposed in 5 different optimization problems:

$$\begin{aligned}
\hat{\tau}_l'' &= \arg\max z(\hat{\phi}_{r,l}', \hat{\Theta}_{r,l}', \hat{\phi}_{t,l}', \hat{\Theta}_{t,l}', \tau_l; \hat{x}_l) \\
\hat{\Theta}_{r,l}'' &= \arg\max z(\hat{\phi}_{r,l}', \Theta_{r,l}, \hat{\phi}_{t,l}', \hat{\Theta}_{t,l}', \hat{\tau}_l''; \hat{x}_l) \\
\hat{\phi}_{r,l}'' &= \arg\max z(\phi_{r,l}, \hat{\Theta}_{r,l}'', \hat{\phi}_{t,l}', \hat{\Theta}_{t,l}', \hat{\tau}_l''; \hat{x}_l) \\
\hat{\Theta}_{t,l}'' &= \arg\max z(\hat{\phi}_{r,l}'', \hat{\Theta}_{r,l}'', \hat{\phi}_{t,l}', \Theta_{t,l}, \hat{\tau}_l''; \hat{x}_l) \\
\hat{\phi}_{t,l}'' &= \arg\max z(\hat{\phi}_{r,l}'', \hat{\Theta}_{r,l}'', \phi_{t,l}, \hat{\Theta}_{t,l}'', \hat{\tau}_l''; \hat{x}_l)
\end{aligned}$$

One SAGE iteration is defined as the combination of the E-step and the M-step for all L MPCs. Note that during the E-step of the $l-$th MPC, the new estimates of the first $l-1$ MPCs can be used for the computation of the observable data of the $l-$th MPC. Convergence of the algorithm is achieved when the difference in the parameter estimates between two consecutive iterations drops below a certain threshold. The initial value for the parameter estimates will be discussed in the next subsections.

2.2.2 Initialization Procedure for the SAGE Algorithm

The cost function $z(\Theta_l; x_l)$ in (2.15) that has to be maximized can have several local maximum in the 5-dimensional parameter space. As it was mentioned above, a good initial guess for the parameter estimates is necessary so that the algorithm converges toward a correct result. In this section, the initialization procedure for the SAGE algorithm that has been used in this thesis is described. It is based on Successive Interference Cancellation (SIC), where each estimate is used to redetermine the observable

data. The initialization E-step is a simplified version of (2.21). The observable data is estimated by removing the contribution of the already estimated MPCs:

$$\hat{y}_l(\tau) = y(\tau) - \sum_{l'=1}^{l-1} s(\tau, \hat{\Theta}'_{l'}) \tag{2.21}$$

The initialization M-step will perform a non-coherent estimation of the delay data on $y_l(\tau)$ (in propagation terms, this is finding the delay corresponding to the maximum of the power delay profile), followed by a joint non-coherent estimation of $(\hat{\Theta}_{t,l}, \hat{\phi}_{t,l})$ on $y_l(\tau)$:

$$\hat{\tau}_l^{(0)} = \arg\max\{\| \int_{T_0} u^*(\tau - \tau_l)\hat{y}_l(\tau)d\tau\|^2\} \tag{2.22}$$

$$(\hat{\Theta}_{t,l}^{(0)}, \hat{\phi}_{t,l}^{(0)}) = \arg\max\{\|\mathbf{Y}_l(\hat{\tau}_l^{(0)}) \cdot C_t(\Theta_{t,l}, \phi_{t,l})\|^2\} \tag{2.23}$$

where $\mathbf{Y}_l(\hat{\tau}_l^{(0)})$ is defined similarly to (2.17) with $y_l(\tau)$ instead of $x_l(\tau)$. Finally, a joint coherent estimation of $(\hat{\Theta}_{t,l}^{(0)}, \hat{\phi}_{t,l}^{(0)})$ on $y_l(\tau)$ is applied:

$$\begin{aligned}(\hat{\Theta}_{t,l}^{(0)}, \hat{\phi}_{t,l}^{(0)}) = \arg\max\{f\left(\hat{\tau}_l^{(0)}, \hat{\Theta}_{t,l}^{(0)}, \hat{\phi}_{t,l}^{(0)}\Theta_{r,l}, \phi_{r,l}\right)^H \\ D\left(\hat{\Theta}_{t,l}^{(0)}, \hat{\phi}_{t,l}^{(0)}\Theta_{r,l}, \phi_{r,l}\right)^{-1} \cdot f\left(\hat{\tau}_l^{(0)}, \hat{\Theta}_{t,l}^{(0)}, \hat{\phi}_{t,l}^{(0)}\Theta_{r,l}, \phi_{r,l}\right)\}\end{aligned} \tag{2.24}$$

where f is defined similarly to (2.16) with $y_l(\tau)$ instead of $x_l(\tau)$. In order to keep these two last estimations computationally feasible, a large angular step is chosen to get a first rough estimate of the angles of departure and arrival. These angles will be refined during the iteration steps of the SAGE algorithm.

2.2.3 Measurement Setup Considerations When Extracting MPCs with SAGE

When using SAGE to extract MPC, it has been seen in the previous subsections that several hypotheses have been made:

- The plane wave assumption holds for all MPCs.
- The different MPCs are independent.
- The propagation parameters are independent.
- The MPCs have to have a certain SNR to be detected and to be estimated as reliable by SAGE (this is not an actual hypothesis, but merely common sense).

These assumptions can be also called as the requirements for planning of a measurement campaign: close obstacles should be avoided, to maintain the plane wave assumption. The measurement range should be limited, in order to keep sufficient measurement SNR to have reliable estimates for the MPCs. The measurement SNR can also be adapted with equipment setup considerations (increased transmit power, longer PN-sequences for channel sounders, etc.)

Another important factor that has not been detailed is the impact of the type of antenna array that is used for the measurement. If a linear array is used, it is easy to notice that the elevation of the MPCs will not affect the phase shift between the different elements of the array. A linear array can thus not be used to estimate the elevation of the MPCs, but only the azimuth of the MPCs. If a circular or a planar array is used, it will give the azimuth of the MPCs, but an ambiguity will remain for the elevation on whether the MPCs comes from an angle θ_l or an angle $\pi - \theta_l$. Only three-dimensional arrays can give the azimuth and elevation of an MPC without ambiguity.

The angular resolution of the array is not a limiting factor for high resolution algorithms like SAGE, but a higher angular resolution (thus more antennas) will give a faster convergence and a more reliable result for the angular estimates. The bandwidth and oversampling factor used for the measurements will intrinsically limit the delay resolution for the estimation of the MPCs' delay. Furthermore, regarding polarization, it is important to have antennas with a sufficient gain for all polarizations to have a good resolution for all polarizations in all directions. Although it is theoretically possible to estimate the horizontal polarization with only vertical antennas, the small error that is made when measuring the horizontal polarization of the vertical antenna in an anechoic chamber will be amplified in the SAGE algorithm, yielding an unreliable result for the horizontal polarization of the MPCs.

In order to avoid unreliable result, only parameters for which the measurement setup has sufficient resolution should be extracted with the SAGE algorithm.

Regarding the estimation parameters used to process the measured data, we could refer to [83]. The data obtained during one sounding cycle (I = 1) were processed with the SAGE algorithm to extract the complex weight, the propagation delay as well as the azimuths and co-elevations of departure and of incidence of 20 waves. Five iteration cycles were performed to calculate the above estimates. The selected quantization steps is $0.1\,\mathrm{deg}$ in azimuth domain.

For this thesis an Uniform Circular Antenna (UCA) was used because azimuth was the point of interest. Next section is dedicated to description of the antennas which have been used for measurement campaigns on which this thesis is based on.

2.3 Antennas

In the measurement campaigns performed for this thesis two kinds of antennas were used: custom made omni-directional dipole antennas (with a gain of 1.75 dB) and a circular antenna array (see Fig 2.4). The antennas were connected to the 8-port switches of the transmitter and receiver of the channel sounder(or directly to the Tx/Rx unit, depending on the campaign) using long low-loss RF cables, which had equal length. The RF cables had excellent RF stability, even when they were slightly bent or moved during the measurements.

2.4 Conclusions

This chapter has presented measurement tools to characterize the wireless propagation channels in this thesis. First, the channel sounding approach has been described.

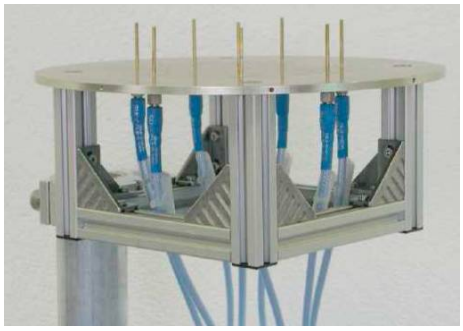

(a) Circular array: Seven elements at circle and one in the middle.)

(b) Circular array: during measurements

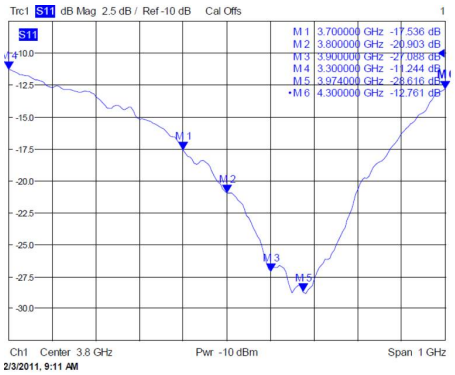

(c) Circular array: Return loss over bandwidth 1GHz

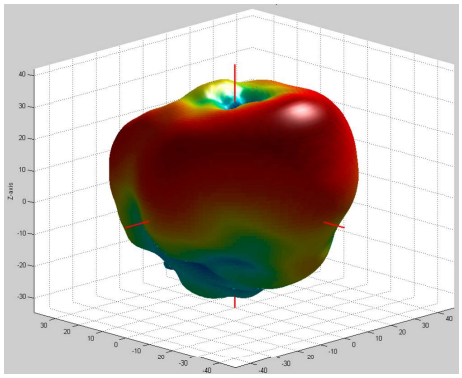

(d) Circular array: Radiation pattern of one element

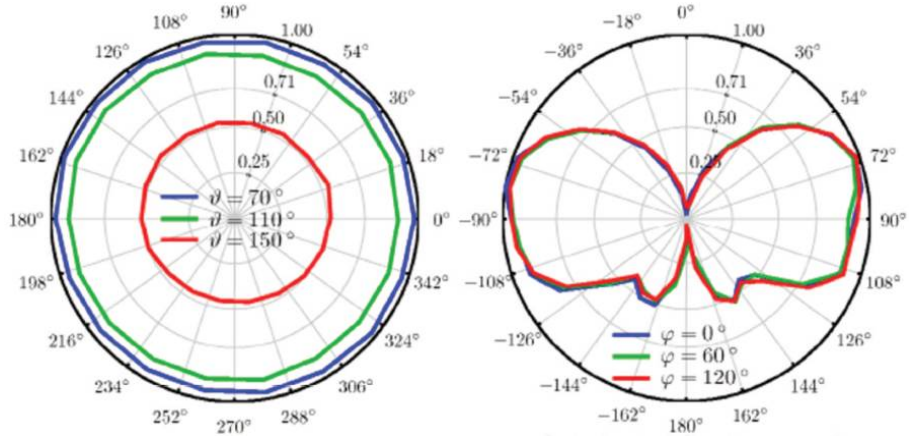

(e) Radiation pattern of the node antenna at 3.8 GHz. Polarization in $\vartheta-$direction versus φ (left) and Polarization in $\vartheta-$direction versus ϑ (right)

Figure 2.4: Used antennas

Various aspects such as synchronization issue, important limitations and techniques have been discussed. Second, the Elektrobit channel sounder has been presented as the practical commercial implementation of the theoretical concept. Main principles of hardware and software used for measurement campaigns were described. Next, important characteristics and parameters of the Elektrobit channel sounder have been presented. High resolution parameter estimation algorithm (SAGE-ISIS) was described. Finally, we completed the description of the equipment used in the measurement campaigns with presenting the antennas.

Chapter 3

Single Antenna Narrowband Channel Modeling

In this chapter, we investigate narrowband indoor peer-to-peer channels based on a wideband experimental campaign at 3.8 GHz in a typical office environment consisting in different rooms aligned along corridor and separated by different types of walls (in contrast to [3], where a single large room with partitions was considered). Key contributions are as follows

- We analyze and model the variations of small-scale fading statistics based on measurements and using the so-called second-order scattering fading (SOSF) distribution [19, 3] which reflects any combination of Rician, Rayleigh, and double-Rayleigh fading [23]. In addition, second-order statistics are derived using a double-ring model [59]. The combination of empirical first-order statistics and geometry-based channel dynamics enables to implement a time-series generator of channel realizations.

- To model the sudden changes of fading statistics, we introduce a three-step approach: (i) for reflecting the sudden changes of the statistics, we define and parameterize a hidden Markov model [79], (ii) the parameters of the SOSF distribution are modeled according to a Beta or an Extreme Value distribution, fitting the measurements, (iii) fading realizations are generated [78].

Details of the measurement campaign are provided in Section 3.1. Section 3.2 introduces the approach to represent non-stationary fading statistics and details the empirical model parameters. The proposed equivalent geometry-based model for second-order scattering fading (SOSF) is presented in Section 3.3. Section 3.4 describes the path-loss and Large-Scale fading models extracted from the measurements and provides an implementation summary and simulation results of the model, which is validated against measurements.

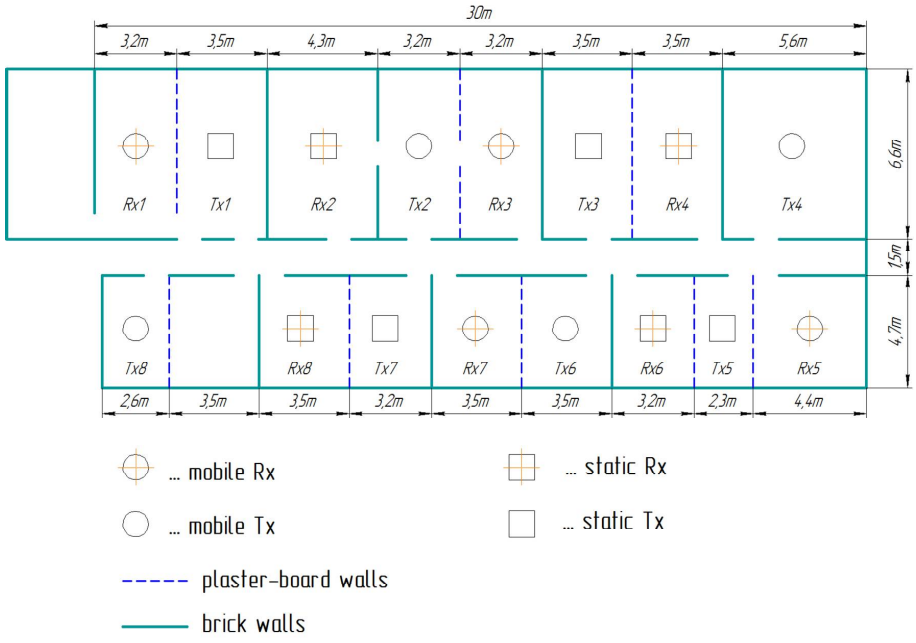

Figure 3.1: Floor-plan of peer-to-peer measurements

3.1 Measurements

3.1.1 Environment

The channel measurement campaign was carried out at the Université Catholique de Louvain (UCL), Louvain-la-Neuve, Belgium, in Fall 2009 (see Figure 3.2). The investigated environment was located on the first floor of an office building, and consisted of typical offices along a corridor separated by brick or plaster-board walls, as illustrated in Figure 3.1. Circles indicate mobile nodes (moving in random directions with the walking speed $v \approx 1$ m/s), squares indicate static nodes; receivers are additionally marked by a cross. Two different types mobility scales were investigated: limited motion (over a small area, i.e. within a square of 1 m^2) and extended motion (over a larger area, i.e. throughout the whole room they were in). Depending on the node mobility, peer-to-peer channels were measured for four sub-scenarios :

- single-mobile links (where only one node is moving),
- double-mobile links (where both nodes are moving),
- links between static nodes(in the absence of moving people in corridors)
- links between static nodes(where a few people moved along the corridors).

For links between static nodes (in the absence and presence of moving people in corridors), channel statistics were investigated in [18]. Hence, this chapter only considers links between mobile nodes.

(a) Limited motion measurements

(b) Corridor

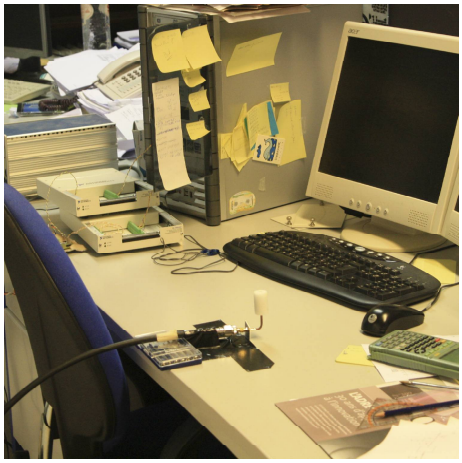

(c) Receiver 6

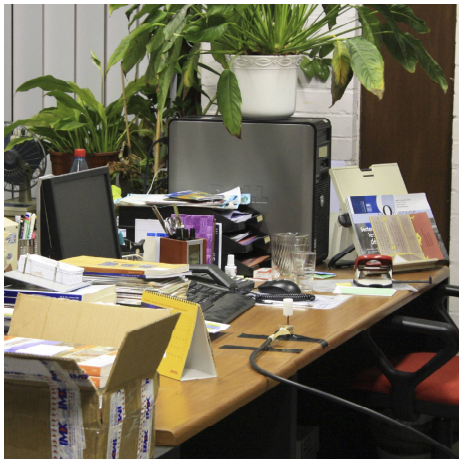

(d) Transmitter 1

Figure 3.2: Pictures of the measurement campaign

Table 3.1: Measurement Parameters (After Post-Processing)

Parameter	Value
Center frequency	3.8 GHz
Transmit power	23 dBm
Measurement bandwidth (null-to-null)	50 MHz
Bandwidth (post-processed)	30 MHz
Recorded frequency tones F	121
Recorded time samples N_s	300
Measurement duration	113 s
Code length	2047

3.1.2 Equipment

The measurements were carried out be means of UCL/ULB Elektrobit PROPSound™ CS at a carrier frequency of 3.8 GHz, using the switched-array principle. The sounder was calibrated twice (before and after measuring channels). The distributed nodes were connected to the 8-port switches of the transmitter and receiver of the channel sounder using long low-loss RF cables, which had equal length. The RF cables had excellent RF stability, even when they were slightly bent or moved during the measurements. At the nodes, custom-made dipole antennas with a gain of 1.75 dB and an almost omnidirectional radiation pattern (see Figure 2.4 e) were used.

The channel sounder used long pseudo-noise (PN) sequences to estimate the impulse response of the radio channels between all combination of Tx and Rx nodes. The measurement parameters are summarized in Table 3.1. The recorded channel transfer function is denoted by $H[t, f, j]$, where t denotes the time index, f denotes the frequency index, and j denotes the link index (one link joining one transmit node to a receive node).

3.1.3 Concepts of Data Analysis

The channel results from the addition (when expressed in logarithmic scale, i.e. in decibels) of path-loss Λ, LS fading $S(t)$ and SS fading $G(t)$. The path-loss is constant over time for a given link, and only depends on the distance between the nodes, whereas large- and small-scale fading are time-variant. Let us define the average received power as

$$\bar{P}[j] = \frac{1}{N_s F} \sum_{t=1}^{N_s} \sum_{f=1}^{F} |H[t, f, j]|^2, \tag{3.1}$$

where t and f denote the time sample and the frequency tones respectively.

It turns out that the minimum stationarity time of SS fading equals 0.8 s. Accordingly, the length of the sliding time window T_{av} used to define the time-variant average power as the received power averaged over all tones was chosen to be 20 time samples (corresponding to $\frac{113 \text{ s}}{300} \cdot 20 = 7.5$ s) and the size of sliding shift of the time

window equals 2, so that the time-variant average power can be written as

$$P[t,j] = \frac{1}{T_{av}F} \sum_{t'=t-T_{av}/2}^{t+T_{av}/2} \sum_{f=1}^{F} |H[t',f,j]|^2. \tag{3.2}$$

Consequently, we obtain $T = \frac{N_s - T_{av}+2}{2} = 141$ realizations of $P[t,j]$ which allow us to evaluate the time-variant average power each $\frac{113\text{ s}}{141} = 0.8$ s.

Based on these two definitions, we may evaluate

- the path-loss exponent η by fitting the log-log variation of $\bar{P}[j]$ over the average distance $\bar{d}_j$ between the nodes of link j,

$$\bar{P}[j]|_{dB} \rightarrow \bar{P}_0|_{dB} - \eta \cdot 10\log_{10}\left(\frac{\bar{d}_j}{d_0}\right), \tag{3.3}$$

  where $\bar{P}_0$ denotes the reference power at the reference distance $d_0 = 1$m [84], [85],

- the LS fading (in decibels)

$$S[t,j] = \bar{P}_0|_{dB} - \eta \cdot 10\log_{10}\left(\frac{\bar{d}_j}{d_0}\right) - P[t,j]|_{dB}, \tag{3.4}$$

- the SS fading (in natural scale)

$$G[t,f,j] = \frac{H[t,f,j]}{\sqrt{P[t,j]}}, \tag{3.5}$$

  the fading amplitude being then simply defined as $g = |G|$.

To extract first-order statistics of time-frequency fading, T blocks of $T_{av} \times F$ of realizations can be used.

For a given link j, LS fading can be expressed as the sum of a mean value and a time-variant component, so that $S[t,j] = \overline{S}[j] + \tilde{S}[t,j]$. $Mean$ LS fading $\bar{S}[j]$ is related to time-invariant site-specific obstructions of the link including the influence of different effects such as refraction, diffraction, reflection, and absorption in environment (furniture, static people etc.). Hence, $\bar{S}[j]$ is a random variable depending on the environment. Large-scale fading $\tilde{S}[t,j]$ is caused by the mobility of scatterers and so-called body fading or shadowing (due to the changing orientation of the person holding the device). Additionally, when nodes are moving over a large scale, it is caused by the mobility of the stations themselves cannot be considered as static unlike the case of limited motion of the nodes. Therefore, we expect the standard deviation $\sigma_{\tilde{s}}$ to increase in the case of extended motion. Dynamic LS fading can also be expressed as

$$\tilde{S}[t,j] = -[P[t,j]|_{dB} - \bar{S}[j]]. \tag{3.6}$$

Note that we can normalize fading so that $\mathbb{E}\{g^2\} = 1$, the expectation being conducted over time or frequency.

3.2 Experimental Characterization of Non-Stationary Time-Frequency Fading Statistics

3.2.1 SOSF Parameters Extracted From Measurements

As it is shown in Chapter 1, small-scale fading over time and/or frequency can be described by a single distribution called SOSF distribution which is specified by two parameters α and β presented in (1.39) and (1.40). Temporal behavior of the parameters can be estimated from experimental time-frequency fading realizations by iteratively fitting the SOSF probability density function assuming a moment-based estimate as starting point [47].

Looking at the values of $\alpha(t)$ and $\beta(t)$ in Figure 3.3, we observe that the five groups presented in Section 1.3 (Rice, Rayleigh, Double Rayleigh, Rayleigh-Double Rayleigh and a combination of Double Rayleigh and LOS) describe the major part of measured small-scale fading realizations. For reasons of simplicity, we neglect points in the middle zone (where $0 < \alpha < 1, 0 < \beta < 1$ and $\alpha + \beta \neq 1$), which occur only with a very low probability($\sim 1\%$).

Figures 3.4 a, c show time-variant changes of the parameters $\alpha(t)$ and $\beta(t)$ for a typical double-mobile channels. We see that predominantly Rayleigh-double-Rayleigh fading ($\beta = 0, 0 < \alpha < 1$) occurs. Only scarcely we observe an impact of LOS (see Figure 3.4 c) or pure double-Rayleigh fading.

Looking at the single-mobile channels in Figures 3.4 b, d, we observe that Rayleigh-double-Rayleigh fading remains the main fading mechanism. However, Rayleigh fading ($\alpha = 0, \beta = 0$) and Rician fading ($\alpha = 0, 0 < \beta < 1$) occur with a higher probability than in the case of the double-mobile channels.

The distribution of the parameter α for the Rayleigh-double Rayleigh subset (see

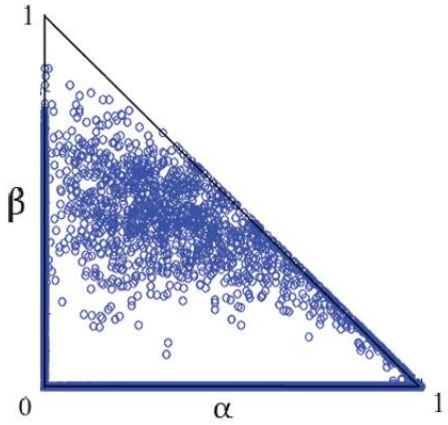

Figure 3.3: Measured parameters of SOSF realizations for Double mobile channels

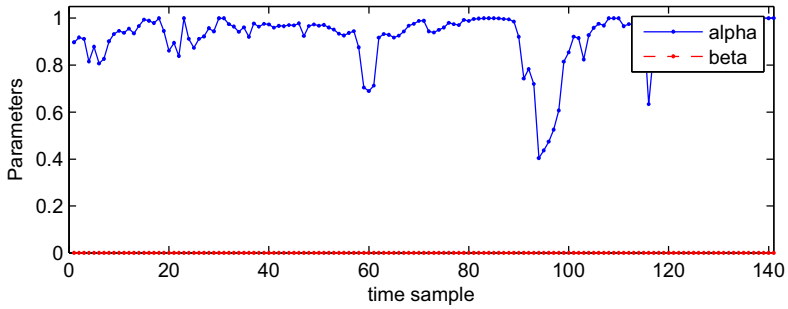

(a) Extended motion, Double mobile channel(Tx4-Rx5)

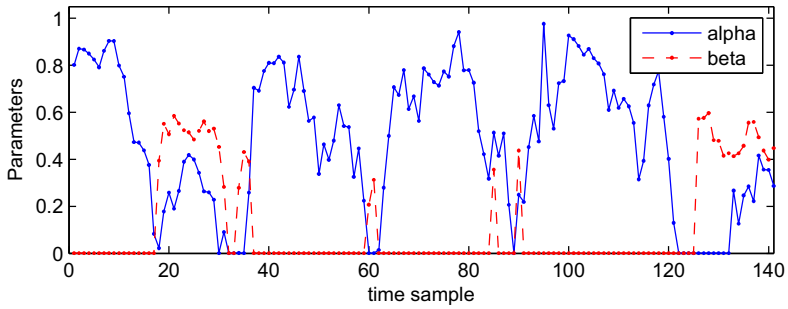

(b) Extended motion, Single mobile channel(Tx7-Rx1)

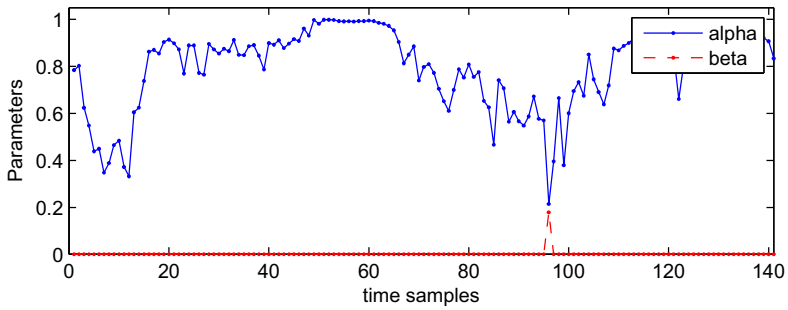

(c) Limited motion, Double mobile channel(Tx4-Rx5)

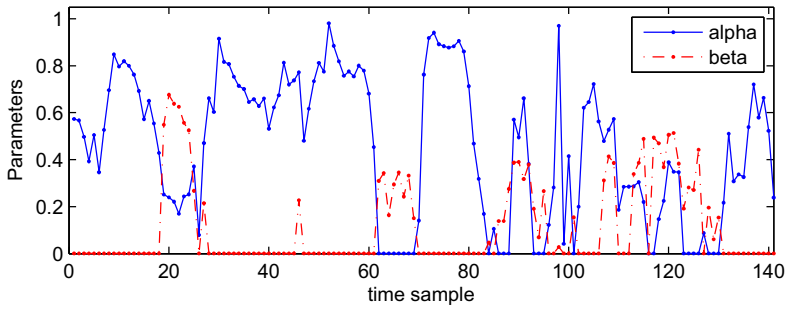

(d) Limited motion, Single mobile channel(Tx7-Rx1)

Figure 3.4: Typical variation of small-scale time-frequency fading parameters over time

Table 3.2: Evaluated parameters of the time-frequency SOSF distribution for different mobility scenarios

Subset	Single Mobile	Double mobile
	Distribution	Distribution
Rician	$K \sim p_{ev}(-1.15, 3.6), \alpha = 0$	$K \sim p_{ev}(-1.83, 3.68), \alpha = 0$
RDR	$\alpha \sim p_\beta(1.8, 0.85), \beta = 0$	$\alpha \sim p_\beta(2.08, 0.79), \beta = 0$
DRLOS	$\Delta \sim p_\beta(1, 1.9)$	$\Delta \sim p_\beta(1.32, 2.73)$

Table 3.3: Probabilities of the subsets

Subset	Single mobile	Double mobile
Rician	0.12	0.05
Rayleigh	0.03	0.02
RDR	0.78	0.86
Double Rayleigh	0.05	0.06
DRLOS	0.02	0.01

Figures 3.5 a, b) is found to be well approximated by the Beta distribution

$$p_\beta(x|p_1, p_2) = \frac{\Gamma(p_1 + p_2)}{\Gamma(p_1)\Gamma(p_2)} x^{p_1 - 1}(1 - x)^{p_2 - 1}, \tag{3.7}$$

where $\Gamma(\cdot)$ denotes the Gamma function. For the DRLOS distribution, we define $\Delta = \sqrt{(1-\alpha)^2 + \beta^2}$, denoting the set of points on the line $\alpha+\beta = 1$. Parameter Δ is also found to be Beta-distributed (see Figure 3.5 c, d). Finally, the distribution of the K-Factor in Rician fading, $K = \frac{\beta}{1-\beta}$, can be modeled by Extreme Value distribution(see Figure 3.5 e, f),

$$p_{ev}(x|\mu, \sigma) = \sigma^{-1} e^{\left(\frac{x-\mu}{\sigma}\right)} e^{\left(-e^{\left(\frac{x-\mu}{\sigma}\right)}\right)}, \tag{3.8}$$

when the K-factor expressed in decibels.

Eventually, probabilities of the subsets and a probability distribution of the SOSF parameters within the subset can be estimated(see Tables 3.3 and 3.2). Note, that a high probability of occurrence for Rayleigh - double Rayleigh fading is observed $(78 - 86\%)$.

Note, that the values of $\alpha(t)$ in Figures 3.4 (a, c) are slightly higher in the case of extended motion. However, for reasons of the final model's simplicity, the parameters

Table 3.4: Values of the parameter τ for the autoregressive model

	Parameter		
Subscenario	τ_K	τ_α	τ_Δ
Double Mobile	1.1 s	3.1 s	1.3 s
Single Mobile	1.4 s	2.8 s	1 s

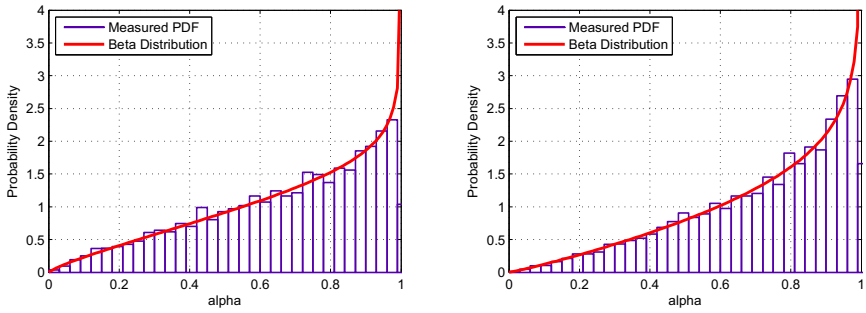

(a) Parameter α, Single mobile

(b) Parameter α, Double mobile

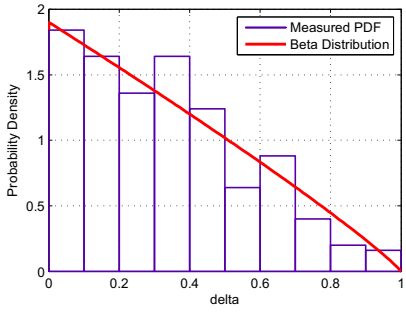

(c) Parameter Δ, Single mobile

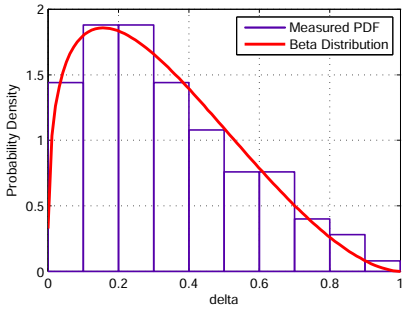

(d) Parameter Δ, Double mobile

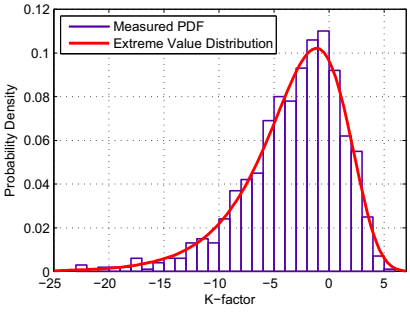

(e) K-factor, Single mobile

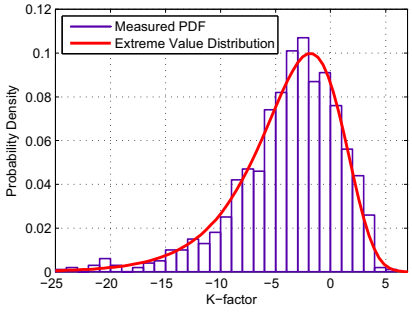

(f) K-factor, Double mobile

Figure 3.5: Probability density functions of the SOSF distribution parameters

shown in Table 3.2 are calculated for the whole set of channels (limited and extended motion scenarios together).

The temporal autocorrelations of the parameters $\alpha(t)$, $K(t)$ and $\Delta(t)$ can be modeled by a decreasing exponential function. Hence, an autoregressive process can be used to generate autocorrelated values of the parameters of a SOSF channel over time samples ($t = [1, \cdots, T]$):

$$\alpha(t) = e^{-\triangle\ t/\tau_\alpha}\alpha(t- \triangle\ t) + \sqrt{1 - e^{-2\triangle\ t/\tau_\alpha}}x_\alpha(t), \tag{3.9}$$

$$\Delta(t) = e^{-\triangle\ t/\tau_\Delta}\Delta(t- \triangle\ t) + \sqrt{1 - e^{-2\triangle\ t/\tau_\Delta}}x_\Delta(t), \tag{3.10}$$

$$K(t) = e^{-\triangle\ t/\tau_K}K(t- \triangle\ t) + \sqrt{1 - e^{-2\triangle t/\tau_K}}x_K(t), \tag{3.11}$$

where x_α, x_Δ, x_K are time series of length T, whose values are drawn independently from the distributions described by Table 3.2. The parameters τ are extracted from measurements and given in Table 3.4. Finally, $\triangle\ t$ is the desired sampling rate which is equal the stationarity period of 0.8s.

Using modeled values of the parameters α and β, the weights in (1.36) can be calculated as

$$\omega_0 = \sqrt{\beta} = \sqrt{\frac{K}{1+K}}, \tag{3.12}$$

$$\omega_1 = \sqrt{1-\alpha-\beta} = \sqrt{1-\alpha-\frac{K}{1+K}}, \tag{3.13}$$

$$\omega_2 = \sqrt{\alpha}. \tag{3.14}$$

3.2.2 Hidden Markov Model

Transitions between different fading states can be modeled by a hidden Markov model (HMM) [79]. Usually, the system being modeled by a HMM is assumed to be a Markov process with unobserved (*hidden*) states. Since the SOSF distribution reduces to the five distributions of small-scale fading highlighted above, we model the transitions between the subsets using a five-state HMM: (i) Rican fading, (ii) Rayleigh-double-Rayleigh fading (iii) pure double-Rayleigh fading, (iv) pure Rayleigh fading and (v) DRLOS fading.

Using measured data, the state transition probabilities have been estimated for the two sub-scenarios (see Table 3.5)

3.3 Double-Ring Models For Peer-to-Peer Radio Channels

The ultimate goal of this chapter is to present a radio channel simulator taking into account both first- and second-order statistics of small-scale fading. However, the

Table 3.5: Transition matrices

Single mobile					
Subset	Rician	RDR	DRLOS	Double Rayleigh	Rayleigh
Rician	0.77	0.19	0.01	0	0.03
RDR	0.03	0.93	0.01	0.02	0.01
DRLOS	0.05	0.44	0.50	0.01	0
Double Rayleigh	0	0.24	0.01	0.75	0
Rayleigh	0.13	0.40	0	0.01	0.46
Double mobile					
Subset	Rician	RDR	DRLOS	Double Rayleigh	Rayleigh
Rician	0.68	0.26	0.01	0.01	0.04
RDR	0.02	0.95	0.01	0.01	0.01
DRLOS	0.03	0.60	0.36	0.01	0
Double Rayleigh	0	0.29	0.01	0.70	0
Rayleigh	0.10	0.54	0	0	0.36

measurement setup does not permit to extract appropriate second-order statistics. For this reason, we need to propose an equivalent representation that is compatible with measured first-order statistics but further enables to model second-order statistics. Geometrically, each room along the corridor can be represented by a local ring of scatterers around a given node. As the nodes were located in different rooms, the corresponding geometry of any given link can indeed be represented by two different rings of scatterers.

3.3.1 Generalized Reference Double-Ring Model for SOSF Channels

The double-ring geometry [59] used to fit a reference model to the SOSF formalism is illustrated in Figure 3.6. Transmitter (Tx) and receiver (Rx) are denoted by 0_T and 0_R, respectively; R_T and R_R are radii of rings which are formed by scatterers $S_T^m (m = 1, 2, \dots M)$ and $S_R^n (n = 1, 2, \dots N)$ located around the transmitter and the receiver. The symbols α_T^m and α_R^n denote the angle of departure (AoD) of the m-th transmitting wave and the angle of arrival (AOA) of the n-th receiving wave, respectively. The following assumptions are made: (i) the nodes move with speed v_T and v_R in the direction determined by the angle of motion γ_T and γ_R for the transmitter and the receiver, respectively[1]; (ii) the distance between Tx and Rx is much larger than the radii R_T and R_R, i.e. $\max(R_T, R_R) \ll D$; (iii) for short periods of time,

[1]Note that each scatterer S_T^m (S_R^n) can be considered as a virtual base-station. Next, the communication link from each base station to the node can be modeled as a conventional fixed-to-mobile link. Hence, the properties of the channel between the nodes are strongly dependent on the scattering environment around each node. The concept of relative motion between Tx and Rx cannot be applied.

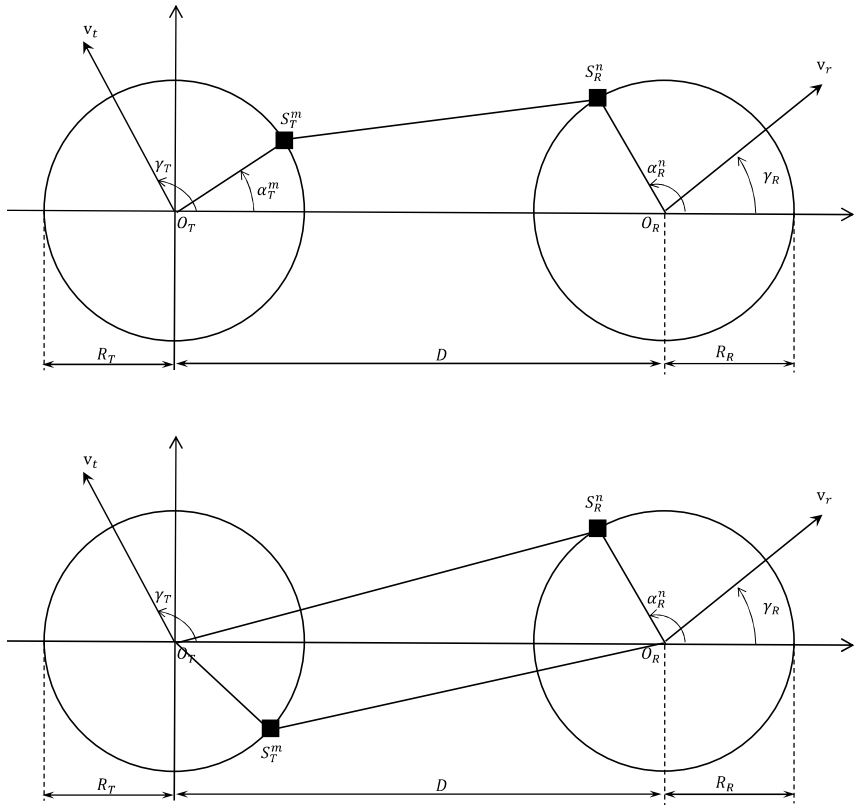

Figure 3.6: The geometrical double-ring model in case of the double bouncing(top) and the single bouncing(bottom)

the mobile environment can be assumed as quasi-stationary, i.e. the rings of scatterers are fixed. The distances which a plane wave travels in the case of so-called double bounce scattering (Figure 3.6 top) or single bounce scattering (Figure 3.6 bottom) can be written as

$$D_{DB} = (D_0 - R_T \cos\alpha_T^m + R_R \cos\alpha_R^n) + R_R + R_T,$$

$$D_{SBT} = D_0 - R_T \cos\alpha_T^m + R_T = D_0 + 2R_T \sin^2 \frac{\alpha_T^m}{2},$$

$$D_{SBR} = D_0 + R_R \cos\alpha_R^n + R_R = D_0 + 2R_R \cos^2 \frac{\alpha_R^n}{2},$$

for scattering at the rings around the transmitter and receiver, respectively.

Based on this representation and extending a single-input and single-output (SISO) version of the reference model presented in Chapter 1.5.2 and [58] to the case of time-frequency second order scattering fading, we can identify 3 types of mechanisms.

Line-of-Sight

The LOS component can be modeled as

$$G_{LOS}(t,f) = e^{j\left(\frac{2\pi f}{c}(tv_T\cos\gamma_T - tv_R\cos\gamma_R - D_0) + \phi_{LOS}\right)}, \tag{3.15}$$

where ϕ_{LOS} is a random phase shift over [0, 2π].

Double Bounce scattering

The component of the channel describing the transmission link under double bouncing conditions can be written as

$$G_{DB}(t,f) = \lim_{\substack{N\to\infty \\ M\to\infty}} \frac{1}{\sqrt{MN}} \sum_{m=1}^{M}\sum_{n=1}^{N} e^{j\left(\frac{2\pi f t}{c}(V_T+V_R) + \phi_{mn} + \psi_{mn}\right)}, \tag{3.16}$$

where ϕ_{mn} denotes the random phase-shift caused by the joint interaction of the scatterers S_T^m and S_R^n and V_T and V_R are described by

$$V_T = v_T\cos(\alpha_T^m - \gamma_T), \tag{3.17}$$

$$V_R = v_R\cos(\alpha_R^n - \gamma_R). \tag{3.18}$$

The phase shift ϕ_{nm} induced by the traveled distance does not depend on time t, and can be expressed as

$$\psi_{nm}(f) = -\frac{2\pi f}{c} D_{DB}. \tag{3.19}$$

In [58] and (1.48) in Section 1.5, the double bounce component has only one phase per path and similar to (3.16). However, when the phase shifts introduced by each scatterer S_T^m and S_R^n are independent, i.e. $\phi_{mn} = \phi_m + \phi_n$, we can express (3.16) as a product of two single sums

$$\begin{aligned} G_{DBI}(t,f) = \lim_{\substack{N\to\infty \\ M\to\infty}} \frac{1}{\sqrt{MN}} &\sum_{m=1}^{M} e^{j\left(\frac{2\pi f}{c}\left(V_T t - 2R_T\sin^2\frac{\alpha_T^m}{2}\right) + \phi_m\right)} \\ &\times \sum_{n=1}^{N} e^{j\left(\frac{2\pi f}{c}\left(V_R t - 2R_R\cos^2\frac{\alpha_R^n}{2}\right) + \phi_n\right)}. \end{aligned} \tag{3.20}$$

Single Bounce scattering

Using the approximations $\sin x \approx x$ (for small x) and $\sin\left(\alpha_R^{m(n)} - \alpha_T^{m(n)}\right) \approx \sin\alpha_{T(R)}^{m(n)}$, we obtain the components caused by single bounce scattering as

$$G_{SBT}(t,f) = \lim_{M\to\infty} \frac{1}{\sqrt{M}} \sum_{m=1}^{M} e^{j\left(\frac{2\pi f t}{c}(V_T+\hat{V}_R) + \phi_m + \psi_m\right)}, \tag{3.21}$$

$$G_{SBR}(t,f) = \lim_{N\to\infty} \frac{1}{\sqrt{N}} \sum_{n=1}^{N} e^{j\left(\frac{2\pi ft}{c}(\hat{V}_T+V_R)+\phi_n+\psi_n\right)}, \tag{3.22}$$

where $\hat{V}_T$ and $\hat{V}_R$ are given by

$$\hat{V}_T = \frac{v_T R_R^2}{2D_0^2}\cos\left(2(\alpha_R^n - \gamma_T)\right), \tag{3.23}$$

$$\hat{V}_R = \frac{v_R R_T^2}{2D_0^2}\cos\left(2(\alpha_T^m - \gamma_R)\right). \tag{3.24}$$

The phase shift introduced by traveled distance

$$\psi_m(f) = -\frac{2\pi f}{c} D_{SBT}, \tag{3.25}$$

$$\psi_n(f) = -\frac{2\pi f}{c} D_{SBR}. \tag{3.26}$$

3.3.2 Weights Identification

The generalized reference model for SOSF can be obtained as a weighted combination of components described by (3.15), (3.16), (3.20), (3.21) and (3.22):

$$\begin{aligned} G(t,f) &= \kappa_{LOS}\cdot G_{LOS}(t,f) \\ &+ \kappa_{SBR}\cdot G_{SBR}(t,f) + \kappa_{SBT}\cdot G_{SBT}(t,f) \\ &+ \kappa_{DB}\cdot G_{DB}(t,f) + \kappa_{DBI}\cdot G_{DBI}(t,f), \end{aligned} \tag{3.27}$$

where the various κ variables are the corresponding weights.

Since the central limit theorem states that each single sum is a zero-mean complex Gaussian process with unit variance, the envelopes $g_{DB}(t,f) = |G_{DB}(t,f)|$, $g_{SBR}(t,f) = |G_{SBR}(t,f)|$ and $g_{SBT}(t,f) = |G_{SBT}(t,f)|$ are all characterized by Rayleigh distributions whereas the envelope $g_{DBI}(t,f) = |G_{DBI}(t,f)|$ enables to reproduce the Double-Rayleigh distribution, so that κ_{DBI} can be identified to ω_2 in (1.36). The Rayleigh term in (1.36) is made of the combination of all other components. In the absence of further information, we may set $\kappa_{DB} = \kappa_{SBT} = \kappa_{SBR} = \frac{\omega_1}{\sqrt{3}}$, assuming that all three mechanisms are occurring with the same probability[2]. Finally, $\kappa_{LOS} = \omega_0$, so that we can express (3.27) as

$$\begin{aligned} G(t,f) &= \omega_0\cdot G_{LOS}(t,f) \\ &+ \frac{\omega_1}{\sqrt{3}}\cdot\left(G_{DB}(t,f) + G_{SBT}(t,f) + G_{SBR}(t,f)\right) \\ &+ \omega_2\cdot G_{DBI}(t,f), \end{aligned} \tag{3.28}$$

where ω_0, ω_1 and ω_2 can be experimentally derived or modeled using the concept described in Section 3.2. From the statistical properties of (3.28), it can be concluded that small-scale time-frequency fading follows a SOSF distribution.

[2]It can be showed that the difference between the channels simulated using different impacts of $\kappa_{DB}, \kappa_{SBT}$ and κ_{SBR} is negligible

3.3.3 Application to Double- and Single-Mobile Scenarios

Let us now apply the generalized reference model to both types of mobility and consider only the temporal fading properties.

Temporal Fading in Double-Mobile Scenarios

Since ϕ_{nm}, ϕ_n and ϕ_m are random, the constant (over time) shifts ψ_{nm}, ψ_m and ψ_n can be arbitrarily set to 0. Furthermore, since $R_{T(R)} \ll D_0$, the impact of (3.23) and (3.24) is negligible when the node is mobile, the reference model under double-mobile conditions describes the fading behavior over time by

$$G_{DB}(t) = \lim_{\substack{N\to\infty \\ M\to\infty}} \frac{1}{\sqrt{MN}} \sum_{m=1}^{M} \sum_{n=1}^{N} e^{j\left(\frac{2\pi f}{c}(V_T t + V_R t) + \phi_{mn}\right)}, \tag{3.29}$$

$$G_{DBI}(t) = \lim_{\substack{N\to\infty \\ M\to\infty}} \frac{1}{\sqrt{MN}} \sum_{m=1}^{M} e^{j\left(\frac{2\pi f}{c} V_T t + \phi_m\right)} \times \sum_{n=1}^{N} e^{j\left(\frac{2\pi f}{c} V_R t + \phi_n\right)}, \tag{3.30}$$

$$G_{SBT}(t) = \lim_{M\to\infty} \frac{1}{\sqrt{M}} \sum_{m=1}^{M} e^{j\left(\frac{2\pi f}{c} V_T t + \phi_m\right)}, \tag{3.31}$$

$$G_{SBR}(t) = \lim_{N\to\infty} \frac{1}{\sqrt{N}} \sum_{n=1}^{N} e^{j\left(\frac{2\pi f}{c} V_R t + \phi_n\right)}. \tag{3.32}$$

Similar to the case of time-frequency fading, $g_{DB}(t) = |G_{DB}(t)|$, $g_{SBR}(t) = |G_{SBR}(t)|$ and $g_{SBT}(t) = |G_{SBT}(t)|$ follow a Rayleigh distribution and the term $g_{DBI}(t) = |G_{DBI}(t)|$ follows the Double-Rayleigh distribution, so that we can express (3.28) as

$$\begin{aligned} G_{dm}(t) = {} & \omega_0 \cdot G_{LOS}(t) \\ & + \frac{\omega_1}{\sqrt{3}} \cdot \big(G_{DB}(t) + G_{SBT}(t) + G_{SBR}(t)\big) \\ & + \omega_2 \cdot G_{DBI}(t). \end{aligned} \tag{3.33}$$

From the statistical properties of (3.33), it can be concluded that small-scale fading under double mobile conditions follows a SOSF distribution.

Temporal Fading in Single-Mobile Scenarios

By setting the phase shifts ψ_{nm}, ψ_n and ψ_m to zero, the reference model under single-mobile conditions[3] can be described by

$$G_{DB}(t) = \lim_{\substack{N\to\infty \\ M\to\infty}} \frac{1}{\sqrt{MN}} \sum_{m=1}^{M} \sum_{n=1}^{N} e^{j\left(\frac{2\pi f}{c} V_R t + \phi_{mn}\right)}, \tag{3.34}$$

$$G'_{DBI}(t) = \lim_{\substack{N\to\infty \\ M\to\infty}} \frac{1}{\sqrt{MN}} \sum_{n=1}^{N} e^{j\left(\frac{2\pi f}{c} V_R t + \psi_n\right)} \sum_{m=1}^{M} e^{j\phi_m}. \tag{3.35}$$

[3]Only expressions for a fixed transmitter are shown in this subsection, but all expressions can similarly be applied to a fixed receiver by changing subscripts.

The component described by (3.32) remains unchanged in single mobile scenarios. Alternatively, $\hat{V}_R$ cannot be neglected in (3.21) since $V_T = 0$. Consequently, (3.21) can be re-written as

$$G'_{SBT}(t) = \lim_{N\to\infty} \frac{1}{\sqrt{N}} \sum_{n=1}^{N} e^{j\left(\frac{2\pi f}{c}\hat{V}_R t + \phi_n\right)}. \tag{3.36}$$

So that we obtain

$$\begin{aligned} G_{sm}(t) = \omega_0 \cdot G_{LOS}(t) \\ + \frac{\omega_1}{\sqrt{3}} \cdot \left(G_{DB}(t) + G'_{SBT}(t) + G_{SBR}(t)\right) \\ + \omega_2 \cdot G'_{DBI}(t). \end{aligned} \tag{3.37}$$

Again, the envelopes $g_{DB}(t) = |G_{DB}(t)|$ and $g_{SBR}(t) = |G_{SBR}(t)|$ follow Rayleigh distributions since the central limit theorem states. However, since the second sum in (3.35) is constant over time, the envelope $g'_{DBI}(t) = |G'_{DBI}(t)|$ also follows a Rayleigh distribution, unlike double-mobile scenarios. The weight ω_2 remains unchanged because it describes the impact of double bounce scattering with independent phase shifts introduced by each scatterer S_T^m and S_R^n.

This means that in case of single mobility, the envelope of $g_{sm}(t) = |G_{sm}(t)|$ has a Rician (or Rayleigh) distribution.

3.3.4 Reference Model Over Frequency

Rather than investigating the temporal behavior at any given frequency, it is also possible to study the fading resulting from the reference model over frequency at any given time. This comes to express the frequency dependence of $\psi_{nm}, \psi_m, \psi_n$, so that we can rewrite the different components of the model as

$$G_{DB}(f) = \lim_{\substack{N\to\infty \\ M\to\infty}} \frac{1}{\sqrt{MN}} \sum_{m=1}^{M}\sum_{n=1}^{N} e^{j\left(-\frac{4\pi f}{c}\left(R_T \sin^2\frac{\alpha_T^m}{2} + R_R \cos^2\frac{\alpha_R^n}{2}\right) + \phi_{mn}\right)}, \tag{3.38}$$

$$G_{SBT}(f) = \lim_{M\to\infty} \frac{1}{\sqrt{M}} \sum_{m=1}^{M} e^{j\left(-\frac{4\pi f}{c} R_T \sin^2\frac{\alpha_T^m}{2} + \phi_m\right)}, \tag{3.39}$$

$$G_{SBR}(f) = \lim_{N\to\infty} \frac{1}{\sqrt{N}} \sum_{n=1}^{N} e^{j\left(-\frac{4\pi f}{c} R_R \cos^2\frac{\alpha_R^n}{2} + \phi_n\right)}, \tag{3.40}$$

$$\begin{aligned} G_{DBI}(f) = \lim_{\substack{N\to\infty \\ M\to\infty}} \frac{1}{\sqrt{MN}} \sum_{m=1}^{M} e^{j\left(-\frac{4\pi f R_T}{c} \sin^2\frac{\alpha_T^m}{2} + \psi_m\right)} \\ \times \sum_{n=1}^{N} e^{j\left(-\frac{4\pi f R_R}{c} \cos^2\frac{\alpha_R^n}{2} + \phi_n\right)}. \end{aligned} \tag{3.41}$$

Since the central limit theorem states, the envelopes of $g_{DB}(f)$, $g_{SBT}(f)$, $g_{SBR}(f)$ are all characterized by Rayleigh distributions whereas the envelope of $g_{DBI}(f)$ follows a double-Rayleigh distribution.

Interestingly, the statistics of $(3.38 - 3.41)$ do not depend on the mobility. This contradicts the assumption that time-, frequency- and space-fading share the same cause. This assumption was used in number of papers [86, 48, 87]. In other words, (3.41) can produce double-Rayleigh fading over frequency even for a single-mobile scenario. Probably, this fact could be the reason for apparent double-Rayleigh fading measurements in single-mobile scenarios in [48], [87], which are based on the same measurement campaign. Indeed, in these models, the fading behavior is characterized by jointly considering time samples and frequency tones, although we have shown above that they might not follow the same distribution in single-mobile scenarios.

3.3.5 Second-Order Statistics of SOSF Channels

We have outlined in Section 3.3.1 that a double-ring geometry could be used to reproduce the SOSF first-order statistics observed in measurements. Therefore, we can use the same geometrical model to infer the second-order statistics (the autocorrelation function), which could not be extracted from our measurements.

Second-Order Statistics in Double Mobile Scenarios

In double-mobile scenarios, the correlation properties of the reference channel model can be summarized as

$$\begin{aligned} R_{G_iG_i}(\tau) &= R_{G_qG_q}(\tau) = \mathbb{E}[G_q(t)G_q(t+\tau)] \\ &= \omega_0^2 \cos\left(2\pi\tau\left(f_T\cos\gamma_T - f_R\cos\gamma_R\right)\right) \\ &+ \frac{\omega_1^2}{3}\left(J_0(2\pi f_T\tau) + J_0(2\pi f_R\tau)\right) \\ &+ \left(\frac{\omega_1^2}{3} + \omega_2^2\right) J_0(2\pi f_T\tau)J_0(2\pi f_R\tau), \end{aligned} \tag{3.42}$$

$$R_{G_iG_q}(\tau) = -R_{G_qG_i}(\tau) = \omega_0^2 \sin\left(2\pi\tau\left(f_T\cos\gamma_T - f_R\cos\gamma_R\right)\right), \tag{3.43}$$

$$\begin{aligned} R_{GG}(\tau) &= \mathbb{E}[G(t)G^*(t+\tau)] = \\ &= \omega_0^2 e^{(j2\pi\tau(f_T\cos\gamma_T - f_R\cos\gamma_R))} \\ &+ \frac{\omega_1^2}{3}\left(J_0(2\pi f_T\tau) + J_0(2\pi f_R\tau)\right) \\ &+ \left(\frac{\omega_1^2}{3} + \omega_2^2\right) J_0(2\pi f_T\tau)J_0(2\pi f_R\tau), \end{aligned} \tag{3.44}$$

where $G = G_i + jG_q$, and f_R, f_T and f_{rel} denote the Doppler frequencies caused by motion of the nodes,

$$f_R = \frac{v_R \cdot f}{c}, \tag{3.45}$$

$$f_T = \frac{v_T \cdot f}{c}. \tag{3.46}$$

By proceeding as in [58] , we can obtain the proofs for the derivations of the auto- and cross-correlations.

Second-Order Statistics in Single Mobile Scenarios

By using [58], it can be shown that the correlation functions of the components described by (3.32), (3.34) and (3.35) are the same. Using [46, §3.715.13, §3.715.18] to derive the correlations of the component (3.36), we can write:

$$\begin{aligned} &R_{G_iG_i}(\tau) = R_{G_qG_q}(\tau) = \mathbb{E}[G_q(t)G_q(t+\tau)] \\ &= \omega_0^2 \cos\left(2\pi\tau\left(f_T\cos\gamma_T - f_R\cos\gamma_R\right)\right) \\ &+ \Big(\frac{2\,\omega_1^2}{3} + \omega_2\Big)\cdot J_0\Big(2\pi f_m\tau\Big) + \frac{\omega_1^2}{3}\cdot J_0\Big(\frac{R^2}{D^2}\pi f_m\tau\Big), \end{aligned} \tag{3.47}$$

$$R_{G_iG_q}(\tau) = -R_{G_qG_i}(\tau) = \omega_0^2 \sin\left(2\pi\tau\left(f_T\cos\gamma_T - f_R\cos\gamma_R\right)\right), \tag{3.48}$$

$$\begin{aligned} R_{GG}(\tau) &= \mathbb{E}[G(t)G^*(t+\tau)] = \\ &= \omega_0^2 e^{(j2\pi\tau(f_T\cos\gamma_T - f_R\cos\gamma_R))} \\ &+ \Big(\frac{2\,\omega_1^2}{3} + \omega_2\Big)\cdot J_0\Big(2\pi f_m\tau\Big) \\ &+ \frac{\omega_1^2}{3}\cdot J_0\Big(\frac{R^2}{D^2}\pi f_m\tau\Big), \end{aligned} \tag{3.49}$$

where f_m denotes the Doppler frequency caused by motion of the mobile node

$$f_m = \begin{cases} f_T & [v_R = 0] \\ f_R & [v_T = 0] \end{cases} \tag{3.50}$$

3.4 Time-Series Model

3.4.1 Path-Loss and Mean Large-Scale Fading

Considering the expression for the received power (3.3) and LS fading (3.4), the combined path-loss and mean LS fading $\Lambda = \Lambda' + \overline{S}$ can be defined as

$$\Lambda = \Lambda_0 + \eta \cdot 10\log_{10}\left(\frac{d}{d_0}\right) + \overline{S}, \tag{3.51}$$

where Λ_0 is the deterministic path-loss at the reference distance $d_0 = 1$m and $\overline{S}$ is found to be normal with zero mean (when expressed in decibels) over the whole set of rooms/links. The deterministic path-loss at the reference distance Λ_0, the path-loss exponent η and the standard deviation $\sigma_{\overline{s}}$ characterizing distribution of $\overline{S}$ have been estimated from the data (see Table 3.6).

3.4.2 Dynamic Large-Scale Fading

When the deterministic path-loss and mean LS fading are removed and small-scale fading is averaged out, the remaining variations are due to dynamic LS fading, as

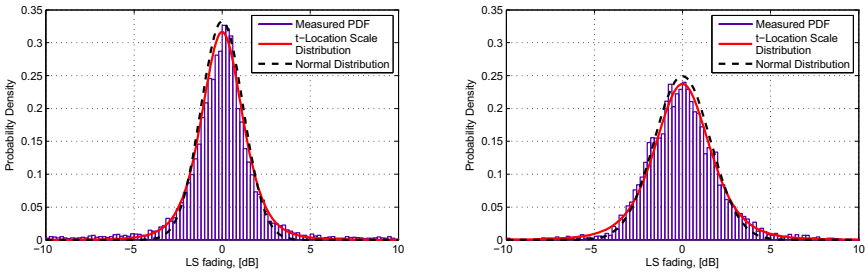

(a) Single mobile, limited motion

(b) Single mobile, extended motion

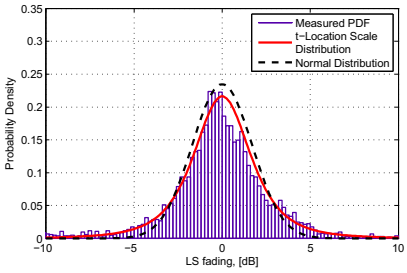

(c) Double mobile, limited motion

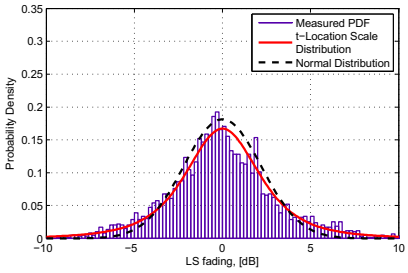

(d) Double mobile, extended motion

Figure 3.7: Fit of the T-location scale and Normal distribution to measured data in different motion scenarios

Table 3.6: Model parameters for path-loss and LS fading

Scenario	$\sigma_{\tilde{s}}$	$\tau_{\tilde{s}}$[s]	ν	Λ_0[dB]	η	$\sigma_{\overline{s}}$
Single-mobile, limited motion	1.1	6.3	5	42	2.8	9.8
Single-mobile, extended motion	1.6					
Double-mobile, limited motion	1.8					
Double-mobile, extended motion	2.5					

detailed earlier. Again, we observe in Figure 3.7 that the dynamic LS fading might be described by a t-location scale distribution

$$p\left(x \mid \nu, \mu, \sigma_{\tilde{s}}\right) = \frac{\Gamma\left(\frac{\nu+1}{2}\right)}{\Gamma\left(\frac{\nu}{2}\right)\sigma_{\tilde{s}}\sqrt{\pi\nu}}\left(1+\frac{1}{\nu}\left(\frac{x-\mu}{\sigma_{\tilde{s}}}\right)^2\right)^{-\frac{\nu+1}{2}}, \tag{3.52}$$

with zero-mean ($\mu = 0$) by definition, $\nu = 5$ degrees of freedom and a scale parameter $\sigma_{\tilde{s}}$ (see Table 3.6). This distribution results from compounding a normal distribution with mean μ and unknown variance, with an inverse gamma distribution placed over the variance with parameters $\alpha_\Gamma = \nu/2$ and $\beta_\Gamma = \nu\sigma_{\tilde{s}}^2/2$. In other words, the dynamic LS fading is assumed to have a Gaussian distribution with an unknown variance distributed as inverse gamma, and then the variance is marginalized out. As it was mentioned in Section 3.1.3, different mechanisms typical for investigated scenarios lead to variations of the value of the scale parameter $\sigma_{\tilde{s}}$ depending on the type of mobility and the motion scale.

Fitting of Normal and t-location scale distributions to measured data is shown in Figure 3.7. The t-location scale distribution has longer tails which represents the measured data better. Analyzing the figure, we can make a conclusion that the more scatterers and objects interacting with radiated waves are involved in the propagation, the higher $\sigma_{\tilde{S}}$ is: it is obvious that extended motion of both nodes will result in more significant variations of the LS fading levels than in the case of limited motion of the Tx (Rx) while the Rx (Tx) is static.

The dynamic LS fading autocorrelation over time is modeled as a decreasing exponential, whose decay time $\tau_{\tilde{s}}$ is also shown in Table 3.6. Hence, we use an autoregressive process to generate autocorrelated dynamic LS fading values,

$$\tilde{S}(t) = e^{-\triangle t/\tau_{\tilde{s}}}\tilde{S}(t-\triangle t) + \sqrt{1-e^{-2\triangle t/\tau_{\tilde{s}}}}x_{\tilde{s}}(t), \tag{3.53}$$

where $x_{\tilde{s}}$ is a time series of length T, whose values are drawn independently from the distributions described by Table 3.6 and $\triangle\ t$ is the targeted resolution in time (in simulation, it equals the stationarity period).

No correlation between dynamic LS fading and the SS fading states has been found, so that we can combine independently simulated dynamic LS fading and small-scale fading realizations.

3.4.3 Small-Scale Fading

Summarizing, we propose to model peer-to-peer channels with time-variant statistics as shown in Figure 3.8. We start with a random initial state of the HMM. Next, using

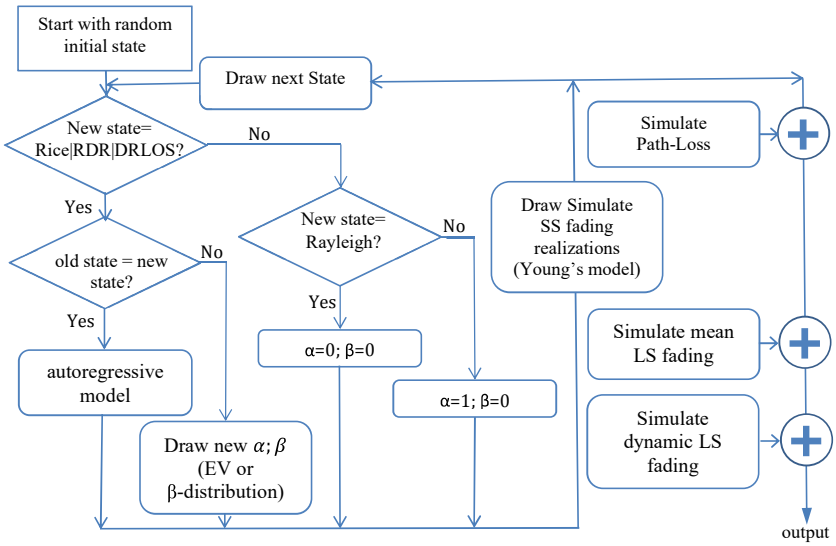

Figure 3.8: Flow-diagram of the simulation model

the corresponding distribution provided in Table 3.2, we draw the SOSF parameters (α, β). Using a weighted combination (the weights are extracted using expressions $(3.12 - 3.14)$) of correlated small-scale fading realizations generated by the model[4] described in [78], we obtain a pre-defined number of correlated complex fading realizations $G(t)$. Next, the path-loss, the mean LS fading and the dynamic LS fading are added to small-scale fading realizations. Next, the state of the HMM is updated. If the state is unchanged, we use the autoregressive models described by $(3.9 - 3.11)$ to generate new values of α, β and Δ for RDR, Rician or DRLOS subsets or we keep the constant values of the parameters for Rayleigh and double-Rayleigh subsets. If the state is modified, depending on the subset, we generate the parameters α and β using the distributions described in Table 3.2 or we set fixed values (for Rayleigh and double-Rayleigh subsets). Note that duration of one state equals $\frac{113[s]}{T} = 0.8$ s.

3.4.4 Simulations and Validation

Modeled time-variant fading statistics of a peer-to-peer network in an indoor office environment are shown in Figure 3.9 (top). The first five pairs (α, β) are then used to simulate channel realizations (only the combination of small-scale fading and dynamic LS fading are illustrated) in Figure 3.9 (bottom).

Figure 3.10 compares the statistics of two sets of measured channels and gener-

[4]Filter coefficients used in the model are specified by appropriate first- and second-order statistics derived in Section 3.3.5.

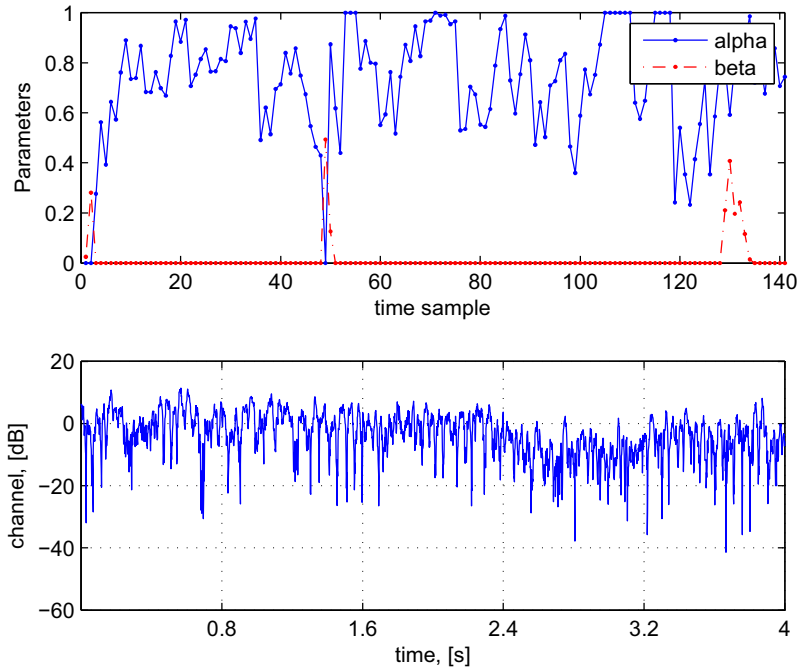

Figure 3.9: Simulated small-scale fading distribution parameters over time for the double-mobile scenario (top). Simulated time-variant components of the channel (small-scale fading and dynamic LS fading) (bottom)

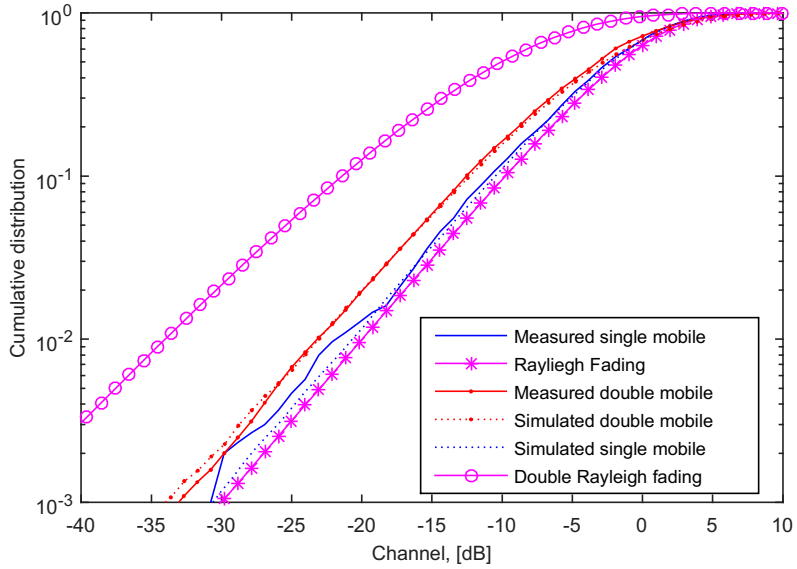

Figure 3.10: Fit of the model to measured data

ated channels using the model of Section 3.4.3. To verify the model under different mobile conditions, we simulated sets of single-mobile links between nodes separated by the distance $d = 12$ m and between mobile nodes separated by the distance $d = 13$ m. Next, we compared the Cumulative Distribution Function (CDF) of the generated small-scale fading with the CDF of measured small-scale fading between nodes having the same parameters (Rx1-Tx7,Rx7-Tx1 and Rx7-Tx8 for single-mobile and double-mobile scenarios respectively). To quantify the difference between CDFs of measured and simulated small-scale fading, the mean squared error (MSE) was estimated for both mobility scenarios. The asymptotic values of MSE ($7.8 \cdot 10^{-5}$ for single mobile and $6 \cdot 10^{-5}$ for double mobile curves) are achieved after 50 simulation trials. Additionally, we used Kullback-Leibler divergence [88] to estimate the number of necessary trials: simulation was stopped after achieving a threshold of 0.01 (used, for example in [89]). The numbers of needed trials are 60 and 50 for single- and double mobile scenarios, respectively. The larger value of MSE and the higher number of simulation trials for the single mobile model can be explained by the fact that we cannot use realizations of small-scale fading measured on different frequency tones(see Section 3.3.3) to obtain CDF of small-scale fading under single mobile conditions. Probably, this explains the non-smooth behavior of the CDF below -20 dB level.

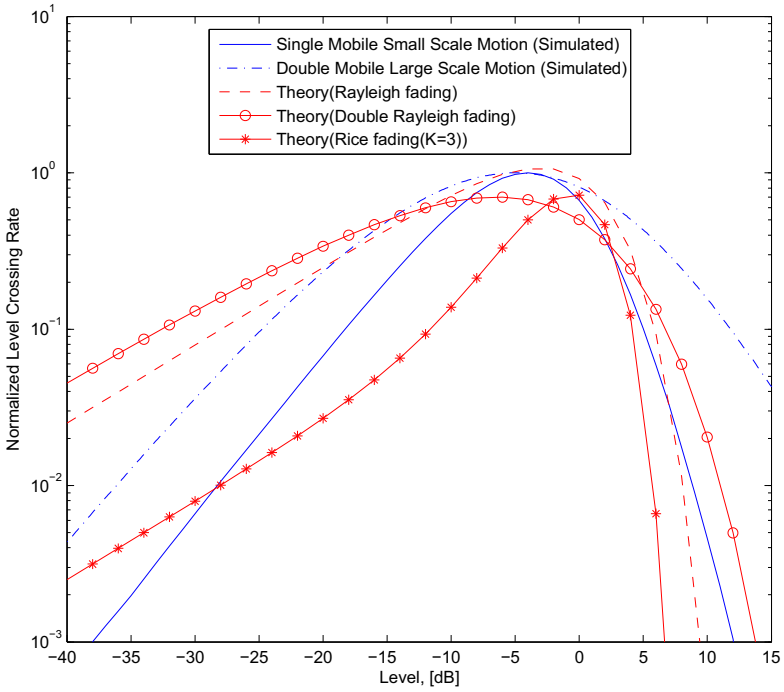

Figure 3.11: Level crossing rate normalized to the maximum Doppler frequency

Figure 3.11 shows normalized Level Crossing Rate (LCR) of the simulated time-variant components of the channel(SS fading and dynamic LS fading) for both types

of mobility and different motion scales in comparison with theoretical curves. It can be noted that simulation results are different from the conventional methods. The comparison of the measured and simulated LCR cannot be provided since we cannot extract LCR from measurements.

3.5 Summary

This chapter has presented an analysis and an empirical model of time-variant channel statistics of a peer-to-peer network based on measurement in an indoor office environment at 3.8 GHz:

1. Models and simulators for second-order scattering fading (SOSF) in different mobility scenarios have been proposed.

2. In double-mobile scenarios, the measured data is characterized by the SOSF distribution, with time-variant statistics ranging from double-Rayleigh to Rician.

3. In single-mobile scenarios, temporal small-scale fading is Rayleigh or Rician distributed.

4. Frequency small-scale fading does not depend on mobility and follows a SOSF distribution.

5. Distributions of the parameter α for the Rayleigh-double Rayleigh and Δ for the double-Rayleigh-LOS subsets can be well approximated by the Beta distribution.

6. Distribution of the K-Factor can be modeled by Extreme Value distribution.

7. Transitions between the fading states are described by a hidden Markov model fully parameterized from the measurements.

8. Following the concept of [3], mean and dynamic LS fading mechanisms are separated. We find that the experimental dynamic LS fading distribution follows the t-location scale distribution.

9. The proposed model has been validated and good agreement between simulations using the proposed model and measurement data is obtained

Chapter 4

Multidimensional Channel Models

In this chapter, we investigate narrowband MIMO channels based on a wideband experimental campaign at 3.8 GHz in a typical office environment consisting of different rooms aligned along corridor and separated by different types of walls. The investigated environment is similar to the one described in the previous chapter, but the measurement campaign was performed in another building. Key contributions are as follows.

- We analyze and model the variations of small-scale fading statistics based on measurements and using the so-called second-order scattering fading (SOSF) distribution similar to the approach presented in Chapter 3: (i) for reflecting the sudden changes of the statistics, we define and parameterize a hidden Markov model [79], (ii) the parameters of the SOSF distribution are modeled according to a Beta or an Extreme Value distribution, fitting the measurements, (iii) fading realizations are generated.
- The stationarity period of indoor MIMO channels is defined.
- We proposed a statistical model of time-variant directional statistics and APS based on the measurements.
- Appropriate spatial correlation functions are derived using a double-ring model [59].
- Simulation model of SOSF MIMO fading channels is proposed.

Details of the measurement campaign are provided in Section 4.1. Section 4.2 describes how the stationarity period can be defined. Section 4.3 introduces the approach to represent non-stationary fading statistics. The proposed equivalent geometry-based model for second-order scattering fading (SOSF) is presented in Section 4.4. Section 4.5 describes the path-loss, large- and small-scale simulation models based on the measurements and Section 4.6 provides an implementation summary and simulation results of the model, which is validated against measurements.

Table 4.1: Measurement Parameters (After Post-Processing)

Parameter	Value
Center frequency	3.8 GHz
Transmit power	23 dBm
Measurement bandwidth (null-to-null)	200 MHz
Bandwidth (post-processed)	120 MHz
Recorded frequency tones	510
Number of frequency tones (post-processed), F	300
Recorded time samples T_s	6000
Measurement duration	60 s
Code length	255

Table 4.2: Distances between the nodes

Nodes	Tx1 (Rx1)	Tx2 (Rx2)	Tx3 (Rx3)	Tx4 (Rx4)	Tx5 (Rx)	Tx6 (Rx6)	Tx7 (Rx7)
Rx(Tx)	21 m	11 m	4 m	8 m	7.5 m	11 m	15 m

4.1 Measurements

4.1.1 Environment

The channel measurement campaign was carried out at the Université Catholique de Louvain (UCL), Louvain-la-Neuve, Belgium, in winter 2016 (see Figures 4.1-4.3). The investigated environment was located on the first floor of an office building, and consisted of typical offices along a corridor separated by brick or plaster-board walls, as illustrated in Figure 4.4. The circles indicate the rooms where nodes were. A static receiver was equipped with UCA, a dipole antenna was used at a mobile transmitter.

First, the Rx (additionally marked with a cross) was located in a room in the middle of the building. The mobile transmitter was successively positioned in different rooms along the corridor. Note that for this measurement the transmitter was moving in arbitrary directions with the walking speed $v \approx 1$ m/s only over a small-scale area (~ 1 m^2).

Second, the mobile Tx was moved to the room where the Rx had been located. Accordingly, single mobile channels were measured between the static Rx sequentially positioned in different rooms along the corridor and the mobile Tx located in the same room (the node marked with a cross). In total, fourteen SIMO channels were measured. Communication channels were measured twice (for each node's position) to eliminate a possible unpredictable influence of random factors.

4.1.2 Equipment

The measurements were carried out by means of UCL/ULB Elektrobit PROPSound™ CS at a carrier frequency of 3.8 GHz, using the switched-array principle. The sounder was calibrated twice (before and after measuring channels). The UCA was connected to the 8-port receiver's switch using RF cables with perfect stability. The transmit

(a) Room with Rx2

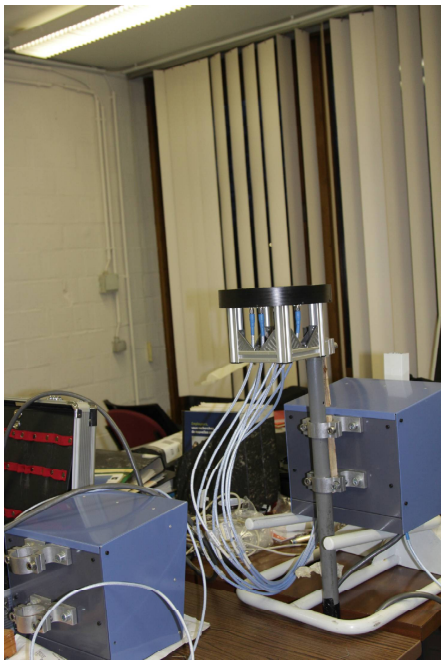

(b) Room with Rx

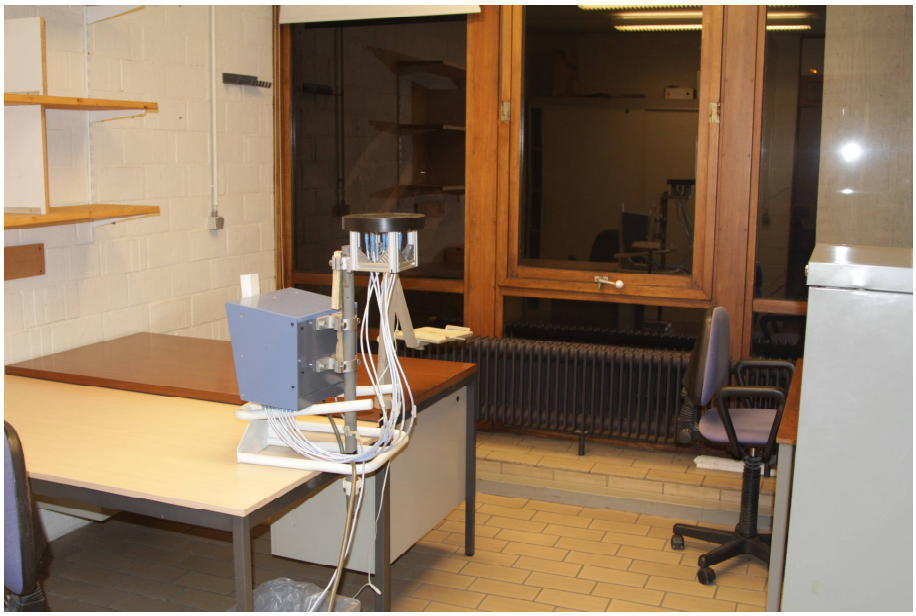

(c) Room with Rx6

Figure 4.1: Pictures of the environment

(a) Room with Rx1

(b) Room with Rx1

(c) Room with Rx3

Figure 4.2: Pictures of the environment

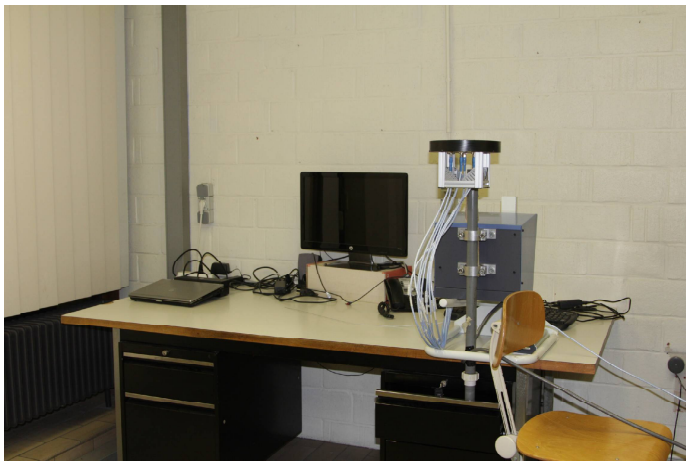

(a) Room with Rx7

(b) Room with Rx4

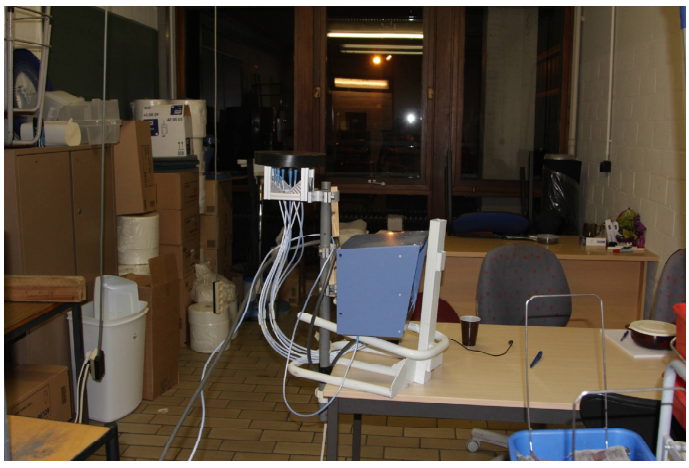

(c) Room Rx5

Figure 4.3: Pictures of the environment

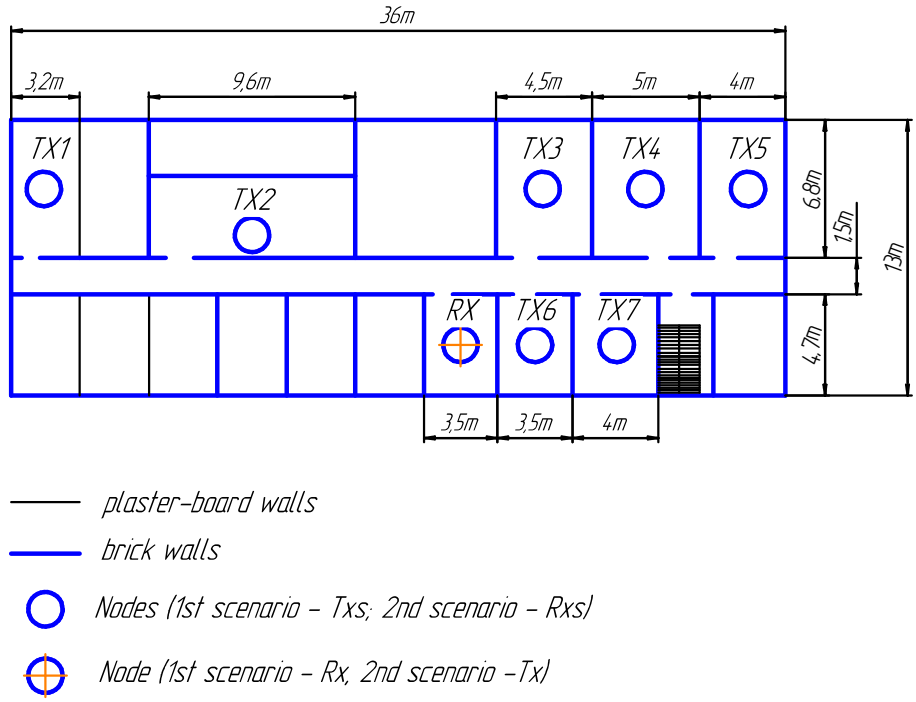

Figure 4.4: Floor-plan of measurements

antenna was directly connected to the TX unit with a long low-loss RF cable. The RF cables had excellent RF stability, even when they were slightly bent or moved during the measurements. At the Tx end, custom-made dipole antenna with a gain of 1.75 dB and an almost omnidirectional radiation pattern (see Section 2.3) was used.

The channel sounder used long PN sequences to estimate the impulse response of the radio channels between all combination of Tx and Rx nodes. The measurement parameters are summarized in Table 4.1. Because of the resulting noise enhancement at the band-limits the further data analysis is restricted to inner 120MHz. The channel transfer function (obtained from the recorded impulse responses) is denoted by $H[t, f, m]$, where t denotes the time index, f denotes the frequency index, and m denotes the link index (one link joining one receive antenna node to the transmitter). ISIS algorithm presented in Section 2.2 was used to estimate directional properties of the measured SIMO channels.

4.1.3 Concepts of Data Analysis

Similarly to the concept used in the previous chapter, the channel coefficients are considered to reflect a superposition of the following propagation phenomena (when the channel is expressed in logarithmic scale):

$$channel = \Lambda + \bar{S} + \tilde{S} + G$$

where $\Lambda,\ \bar{S},\ \tilde{S}$, and G are path-loss, mean LS fading, dynamic LS fading and SS fading, respectively.

The path-loss is constant over time for a given MIMO channel, and only depends on the distance between the nodes, whereas large- and small-scale types of fading are time-variant.

Let us define the average received power as

$$\bar{P} = \frac{1}{T_s F M} \sum_{m=1}^{M} \sum_{t=1}^{T_s} \sum_{f=1}^{F} |H[t, f, j]|^2 \tag{4.1}$$

where m, t and f denote the link number, the time sample and the frequency tones respectively.

The length of the sliding time window T_{av} used to define the time-variant average power as the received power averaged over all tones was chosen to be 20 wavelength (160 time samples i.e corresponding to 1.6 s), so that the time-variant average power can be written as

$$P[t, b] = \frac{1}{T_{av} F_{sub} M} \sum_{t'=t-T_{av}/2}^{t+T_{av}/2} \sum_{f=1+(b-1)F_{sub}}^{bF_{sub}} \sum_{m=1}^{M} |H[t', b, m]|^2 \tag{4.2}$$

Based on these two definitions, we may evaluate the effects observed earlier for narrowband SISO channels:

- the path-loss exponent η by fitting the log-log variation of $\bar{P}$ over the average distance $\bar{d}$ between the Tx and Rx,

$$\Lambda|_{dB} \to \Lambda_0|_{dB} - \eta \cdot 10 \log_{10} \left(\frac{\bar{d}}{d_0} \right), \tag{4.3}$$

  where Λ_0 denotes the reference power at the reference distance $d_0 = 1$m [84], [85],

- the large-scale fading (in decibels)

$$S[t, b] = \bar{P}_0|_{dB} - \eta \cdot 10 \log_{10} \left(\frac{\bar{d}}{d_0} \right) - P[t, b]|_{dB}, \tag{4.4}$$

- the small-scale fading (in natural scale)

$$G[t, f] = \frac{H[t, f]}{\sqrt{P[t, \lceil f / F_{sub} \rceil]}}, \tag{4.5}$$

  where $\lceil \cdot \rceil$ is the ceiling function. The fading amplitude being then simply defined as $g = |G|$.

For a given channel, LS fading can be expressed as the sum of a mean value and a time-variant component, so that $S[t, b] = \overline{S}[b] + \tilde{S}[t]$. $Mean$ large-scale fading $\bar{S}[b]$ is related to time-invariant site-specific obstructions of the link including the influence of different effects such as refraction, diffraction, reflection, and absorption in environment (furniture, static people etc.). Hence, $\bar{S}[b]$ is a random variable depending

on the environment. $Dynamic$ large-scale fading $\tilde{S}[t]$ is caused by the mobility of scatterers and so-called body fading or shadowing (due to the changing orientation of the person holding the device).

Dynamic LS fading can also be expressed as

$$\tilde{S}[t,b] = -[P[t,b]|_{dB} - \bar{S}[b]]. \tag{4.6}$$

Note that we can normalize fading so that $\mathbb{E}\{g^2\} = 1$, the expectation being conducted over time or frequency.

4.2 Experimental Characterization of Stationarity Period

We concentrate our analysis on SS fading, hence, all correlation matrices are calculated after removing the path-loss and LS fading from the channel.

As it was shown in Chapter 1, the correlation matrix distance can be used to determine stationarity periods. However, to use this metric, the correlation matrices must be calculated first. In [90], an impact of the correlation matrix estimation accuracy on the computation of stationarity intervals was investigated. It was shown that the choice of the number of snapshots used to estimate correlation matrices must be

- large enough in order to accurately estimate the Tx, Rx and full correlation matrices,
- but small enough in order to average over snapshots having the same statistics (i.e. the channel behavior remains unchanged over this set of snapshots).

For small window sizes, the estimated correlation matrices may be significantly different from their expectations. Hence, CMD matrices will be roughly estimated. No stationarity regions can be detected. As the window size increases, the correlation matrices will be closer to their expectations. As a consequence, CMD matrices are more reliable and have smoother variations, while stationarity regions can now be identified. However, if the window is too long, then temporal variations of CMD will be smoothed out and the channel mistakenly will be characterized as stationary for the whole measured interval.

4.2.1 Calculation of Correlation Matrices

Since SIMO channels with 8 receive antennas were measured, we will concentrate our analysis on the receive spacial correlation matrices (1.21). When considering narrowband multi-antenna systems (i.e. frequency fading is flat), it is possible to use the frequency samples of a wideband multi-antenna measurements as fading realizations too. Therefore, in addition to the spatial realizations, also the frequency realizations are used as fading realizations in this thesis.

Due to the maximum observed delay spread of $\tau_{max} =\sim 250$ ns, the coherence bandwidth is estimated to be $F_{coh,min} = 1/\tau_{max} = 4$ MHz ($n_{f.coh} = 10$ frequency chips), therefore, within 120 MHz, there are only 30 independent frequency realizations, which means that effectively a smaller number of independent samples is available.

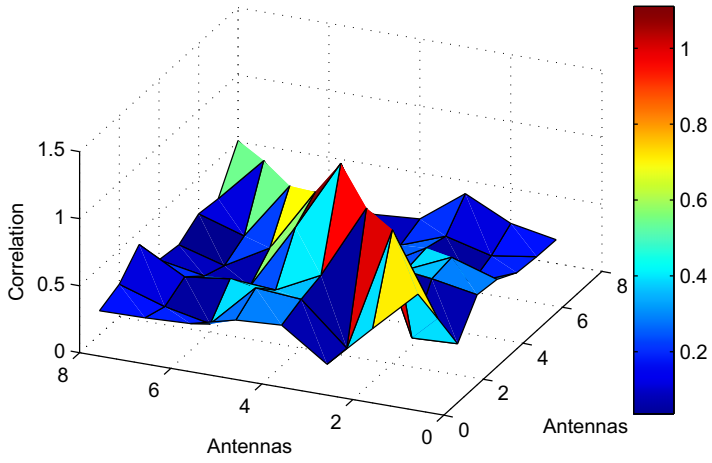

Figure 4.5: An example of the correlation matrix R_{Rx} measured for the channel Tx-Rx2

Since the receiver and the scatterers are fixed, we obtain a maximal Doppler shift $f_{max} = |v_{max}|f_c/c_0 = 12.7$Hz, with the center frequency f_c and the speed of light in vacuum c_0. This results in a minimal coherence time $T_{coh,min} = 1/f_{max} = 79$ ms.

As it was mentioned before, the choice of the time window is not trivial. It turns out that the channels between Tx(Rx) 6,7 and the Rx(Tx) are less correlated than in the case of Tx(Rx) 1-5. It can be explained by the fact that they are located in rooms on the same side of the corridor and the distance is smaller, so the MPCs arriving the receiver are influenced by larger number of various objects around the nodes at both ends of the channel. In the case of Tx(Rx) 1-5, the features of the measured environment around the static Rx have more impact on the MPCs. This means that the CMD is higher for the channels Tx(Rx) 6,7, hence, a larger time window can be used. On the contrary, for a correct analysis, a smaller time window has to be used in the case of Tx(Rx)1-5, because some of the variations of the temporal CMD can be mistakenly averaged out. However, for simplicity reasons let us use a window of the same length.

Different time windows of $5 - 15 \times T_{coh,min}$ were inspected and it turns out that the maximum time window allowing to detect stationarity regions for all measured channels equals $n_t = 5 \cdot T_{coh,min} = 40$ (approximately equivalent to a traveled distance of 5λ).

In order to obtain estimates of the correlation matrices, we average over an ensemble of $n_t = 40$ time samples and $n_f = 300$ frequency tones. In total, we thus average over 12000 (5×30 non-coherent) realizations. Hence, the time-variant correlation matrix $R_{Rx}(t)$ can be calculated as

$$R_{Rx}(t) = \frac{\mathbb{G}\mathbb{G}^H}{n_t \cdot n_f}, \tag{4.7}$$

where $\mathbb{G}$ is a data matrix with dimensions of $n_{antennas} \times (n_t \cdot n_f)$, where each column

corresponds to the used time-frequency data block.

These time-variant matrices (see Figure 4.5) are used for the estimation of stationarity periods of the measured channels.

4.2.2 Calculation and Analysis of CMD

As it was shown in Chapter 1, the CMD (see equation 1.26) between $R_{Rx}(t_i)$ and $R_{Rx}(t_j)$ can be used as a measure of non-stationarity, where $R_{Rx}(t_{i,j})$ are the correlation matrices calculated with (4.7) for time instants $i, j = 1 \dots T_s - n_t$. Conventionally, a channel is considered to be stationary over a region (a traveled distance, time period, frequency range etc.) if the CMD is bellow the 0.2 threshold. In this research, stationarity is studied in the time domain, however it is possible to derive stationarity over space due to the assumption that speed was constant and equal 1 m/s.

Figure 4.6 shows stationarity periods estimated as in [90]. A possible approach for stationarity periods modeling is to allow it to be a random variable with a distribution extracted from measured channels. Cumulative distribution function of estimated time-variant stationarity periods for all measured channels is shown in Figure 4.7. This approach makes sense in the case of high mobility of the node(s) traveling over a diverse environment where MPCs are influenced by many obstacles which may appear and disappear with a high speed.

For indoor propagation channels this manner of modeling can be superfluous and make the model too complex. For this reason we will use a fixed value rather than a random variable. This fixed time window can be defined as the minimum duration of stationarity period observed in the measurements or a value corresponding to a threshold of the CDF.

As all correlation matrices within the period must be mutually correlated, the stationarity period must be defined as a squared one. In Figure 4.8 these time periods are indicated by red squares of sizes $n_{st.per} \times n_{st.per}$. Note, that the minimum duration of stationarity period shown in Figure 4.7 is the same as the one estimated by the second approach (squared stationarity regions) and equals $n_{st.per} = 80$ samples $= 0.8$ s (equivalent to the traveled distance of $\sim 10\lambda$).

Next, blocks of $n_{st.per} \times n_{f.coh} \times n_{antennas}$ can be used to extract time-variant statistics of narrowband SOSF SIMO channels.

4.3 Experimental Characterization of Non-Stationary Fading Statistics

4.3.1 SOSF Parameters Extracted From Measurement

Analogously to Chapter 3, small-scale fading over time can be described by a SOSF distribution which is specified by two parameters α and β presented in (1.39) and (1.40). Again, by iteratively fitting the SOSF probability density function assuming a moment-based estimate as starting point [47], temporal behavior of the parameters can be estimated from experimental fading realizations. Examples of temporal variations

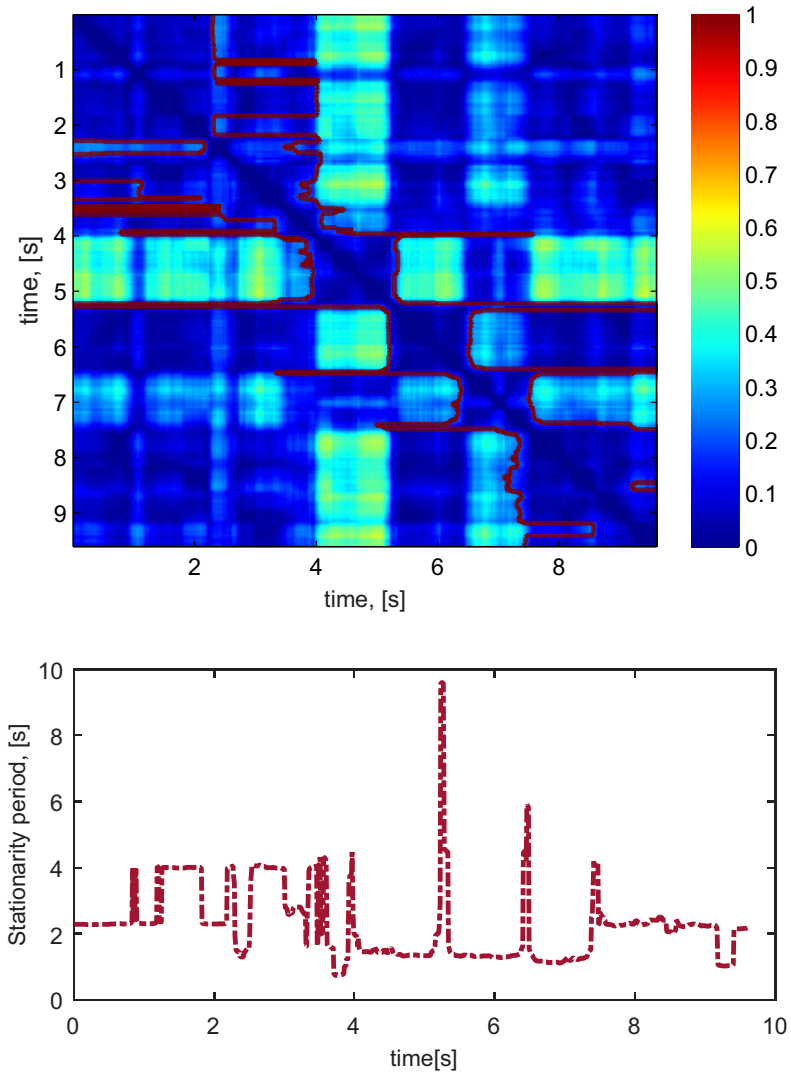

Figure 4.6: Correlation Matrix Distance for 10 seconds of measured channel Tx-Rx6

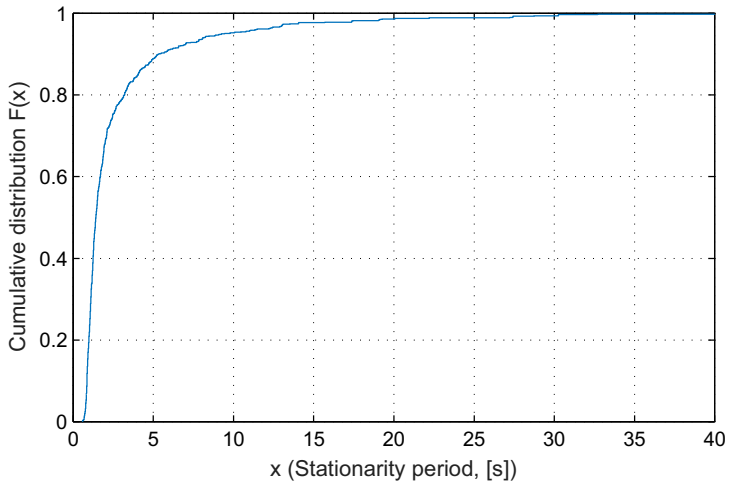

Figure 4.7: Cumulative Distribution Function of measured time-variant stationarity periods

Table 4.3: Evaluated parameters of the SOSF distribution

Subset	Distribution Parameters	Probability	τ
Rician	$K \sim p_{ev}(-3.1, 3), \alpha = 0$	0.12	$\tau_K = 0.8s$
RDR	$\alpha \sim p_{\beta}(3, 4.2), \beta = 0$	0.83	$\tau_\alpha = 2.4s$
Rayleigh	–	0.05	–

of the parameters are shown in Figure 4.9. Again, we see that predominantly Rayleigh-double-Rayleigh fading ($\beta = 0, 0 < \alpha < 1$) occurs. Only scarcely we observe an impact of LOS.

In Figure 4.10 a, three main groups (Rice, Rayleigh, Rayleigh-Double Rayleigh) can be observed. These subsets of SOSF describe the major part of measured SS fading realizations. For reasons of simplicity, we neglect DRLOS and points in the middle zone (where $0 < \alpha < 1, 0 < \beta < 1$ and $\alpha + \beta \neq 1$).

The distribution of the parameter α for the Rayleigh-double Rayleigh subset (see Figures 4.10 b) is found to be well approximated by the Beta distribution (see (3.7)). The distribution of the K-Factor in Rician fading, $K = \frac{\beta}{1-\beta}$, can be modeled by Extreme Value distribution(see equation (3.8) and Figure 4.10 c), when the K-factor expressed in decibels.

Eventually, probabilities of the subsets and a probability distribution of the SOSF parameters within the subset can be estimated (see Table 4.3). Note, that a high probability of occurrence for Rayleigh - double Rayleigh fading is observed as in the case of SISO SOSF channels.

Similar to the approach presented in Chapter 3, the temporal autocorrelations of the parameters $\alpha(t)$, $K(t)$ can be modeled by a decreasing exponential function. Hence, an autoregressive process (3.9) and (3.11) can be used to generate au-

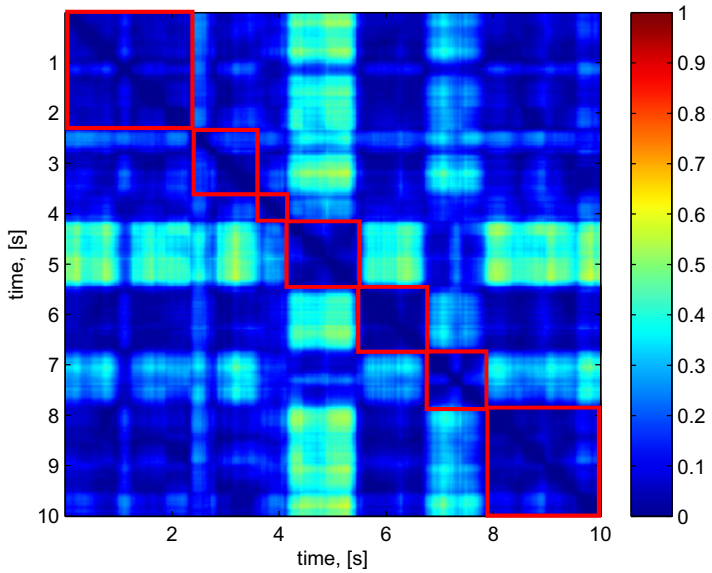

Figure 4.8: Correlation Matrix Distance for 10 seconds of measured channel Tx-Rx6, squared definition of stationarity periods

tocorrelated values of the parameters of a SOSF channel over time samples, where x_α, x_Δ, x_K are time series of length T, whose values are drawn independently from the distributions described by Table 4.3. The parameters τ are extracted from measurements and given in Table 4.3.

Using modeled values of the parameters α and β, the weights in (1.36) can be calculated as

$$\omega_0 = \sqrt{\beta} = \sqrt{\frac{K}{1+K}}, \tag{4.8}$$

$$\omega_1 = \sqrt{1-\alpha-\beta} = \sqrt{1-\alpha-\frac{K}{1+K}}, \tag{4.9}$$

$$\omega_2 = \sqrt{\alpha}, \tag{4.10}$$

4.3.2 Hidden Markov Model

Transitions between different fading states can be modeled by a hidden Markov model (HMM) [79]. Usually, the system being modeled by a HMM is assumed to be a Markov process with unobserved (*hidden*) states. Since the SOSF distribution reduces to the three distributions of small-scale fading highlighted above, we model the transitions between the subsets using a three-state HMM: (i) Rican fading, (ii) Rayleigh-double-Rayleigh fading and (iii) pure Rayleigh fading.

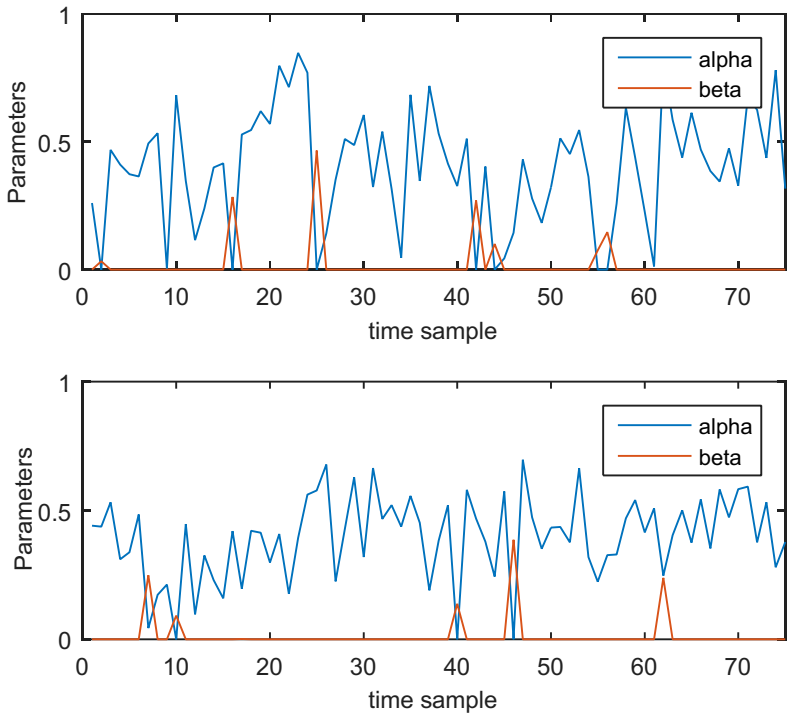

(a) Time variant fading statistics, Tx-Rx

Figure 4.9: Typical variation of small-scale fading parameters over time for Tx1-Rx(top) and Tx-Rx1(bottom)

Table 4.4: Transition matrix

Subset	Rician	RDR	Rayleigh
Rician	0.19	0.10	0.12
RDR	0.75	0.85	0.81
Rayleigh	0.06	0.05	0.07

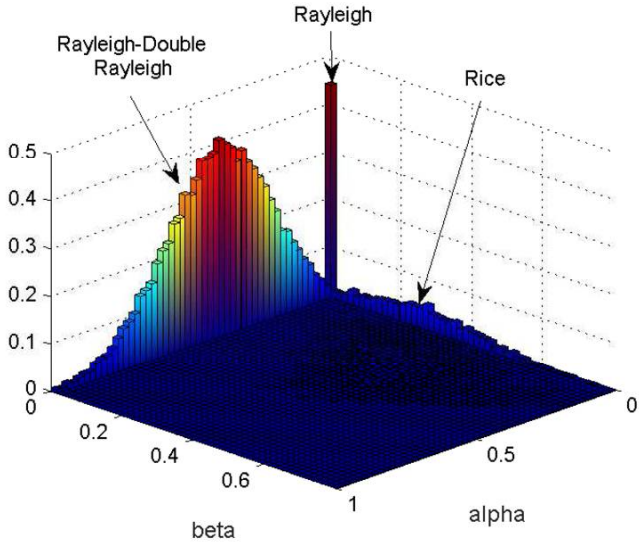

(a) Distribution of the SOSF distribution parameters

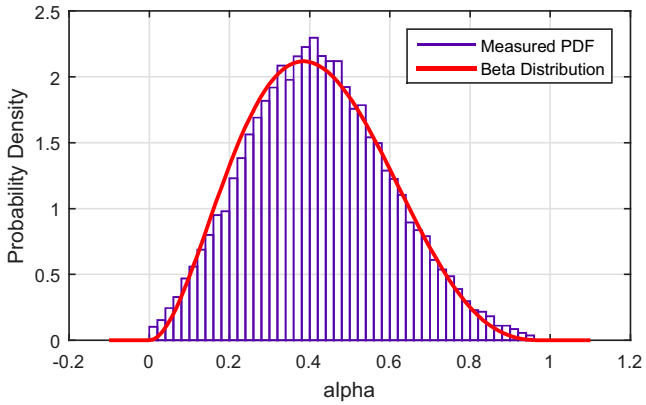

(b) Distribution of parameter α

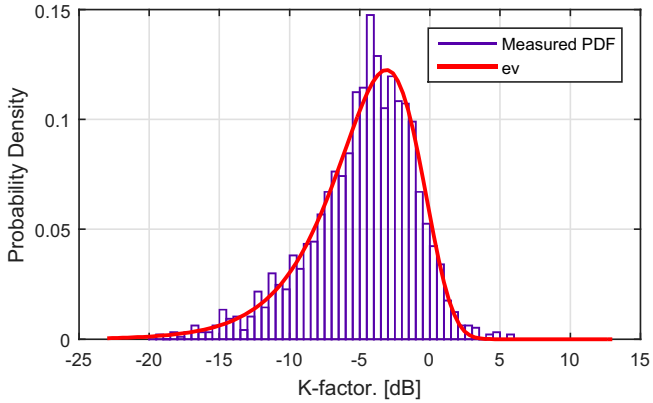

(c) Distribution of K-factor

Figure 4.10: Probability density functions of the SOSF distribution parameters

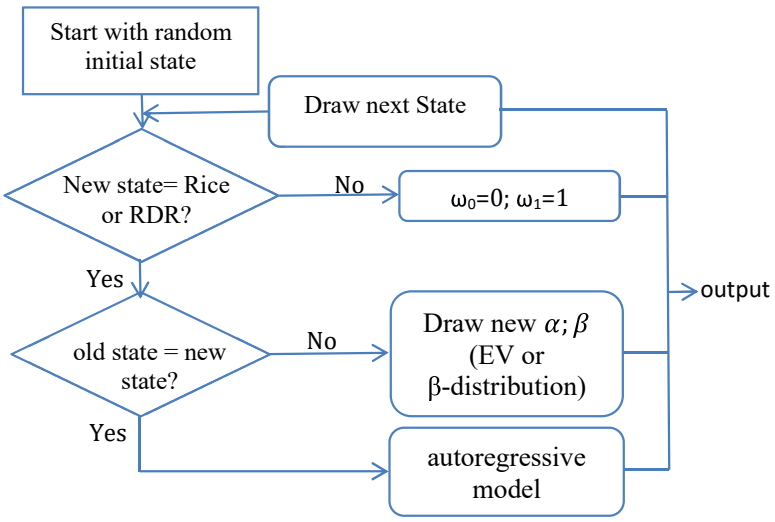

Figure 4.11: Flow-diagram of time-variant statistics modeling

4.3.3 Directional Statistics

Both powers and AoAs of MPCs were estimated. Figures 4.12 and 4.13 show APS extracted from the measurements. Two situations can be differentiated: when the nodes are on the same and opposite sides of the corridor. When the corridor is a part of the propagation channel, the major part of waves arrives over a smaller angular range. Usually, the maximum direction of arriving waves corresponds to a corner of the room where the RX is located. In the case when the nodes are located in the rooms on the same side of the corridor, AoAs are dispersed over a larger range, mostly concentrated in the direction of the transmitting node. Moreover, a noticeable impact of the backscattering is observed.

The distribution of measured AoAs can be approximated by a mixture of TvM distributions:

$$p_{TvM}(x|\mu,\kappa) = \frac{e^{(\kappa\cos(x-\mu))}}{2\pi I_0(\kappa)}, \tag{4.11}$$

where I_0 is the modified Bessel function of order 0, κ and μ are measures of concentration and location, respectively. Note, that the Tikhonov-von Mises function can be directly used to model APS as in [91] by

$$APS(x) = P_0 p_{TvM}(x), \tag{4.12}$$

where P_0 is total power of received signal.

Let us analyze and model these two different situations mentioned above separately. In figures 4.12 and 4.13 (Rx (Tx) 1-5) we can see a peak pointing towards the transmitter. The corresponding peak of the AoA distribution can be modeled as a Tikhonov-von Mises distribution with a large parameter $\kappa_{1,diff}$ and the mean direction $\mu_{1,diff}$.

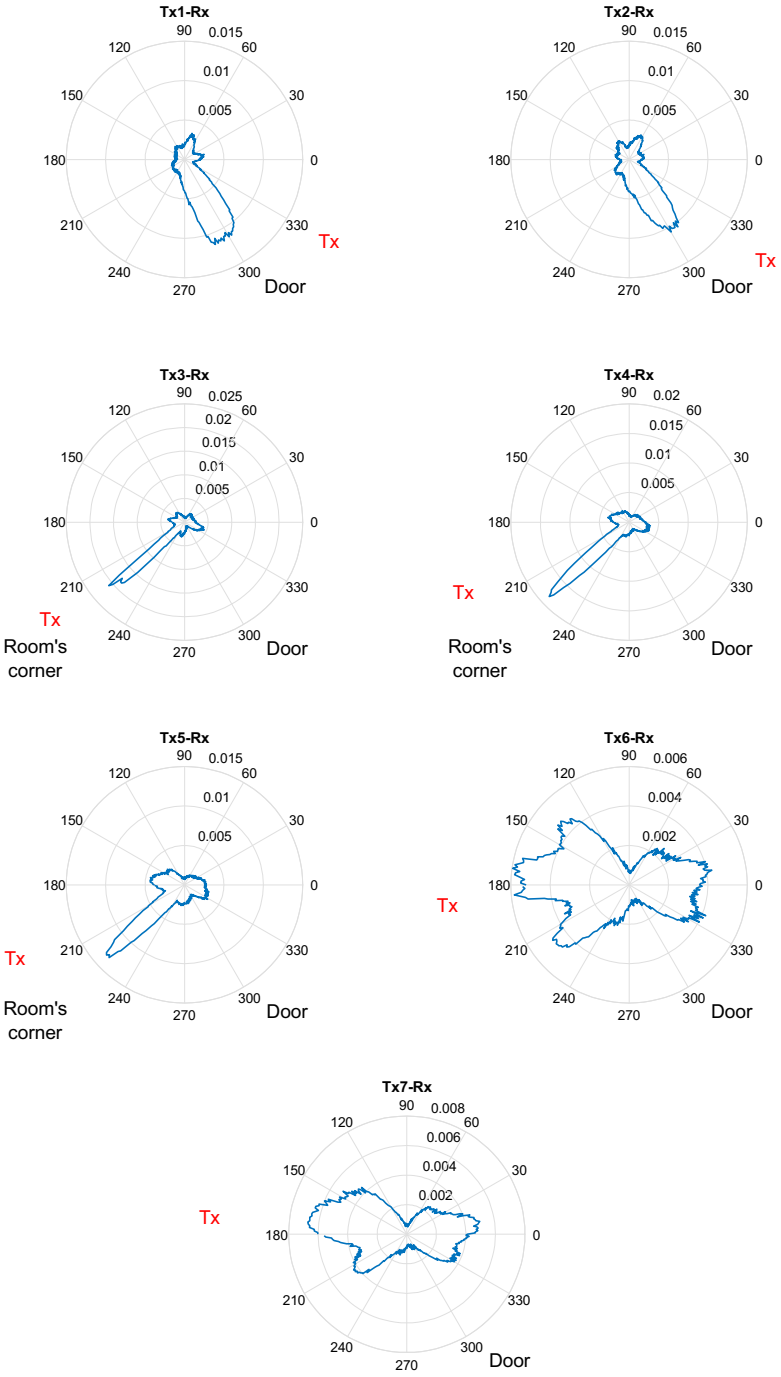

Figure 4.12: Angular Power Spectrum (Rx in the same room)

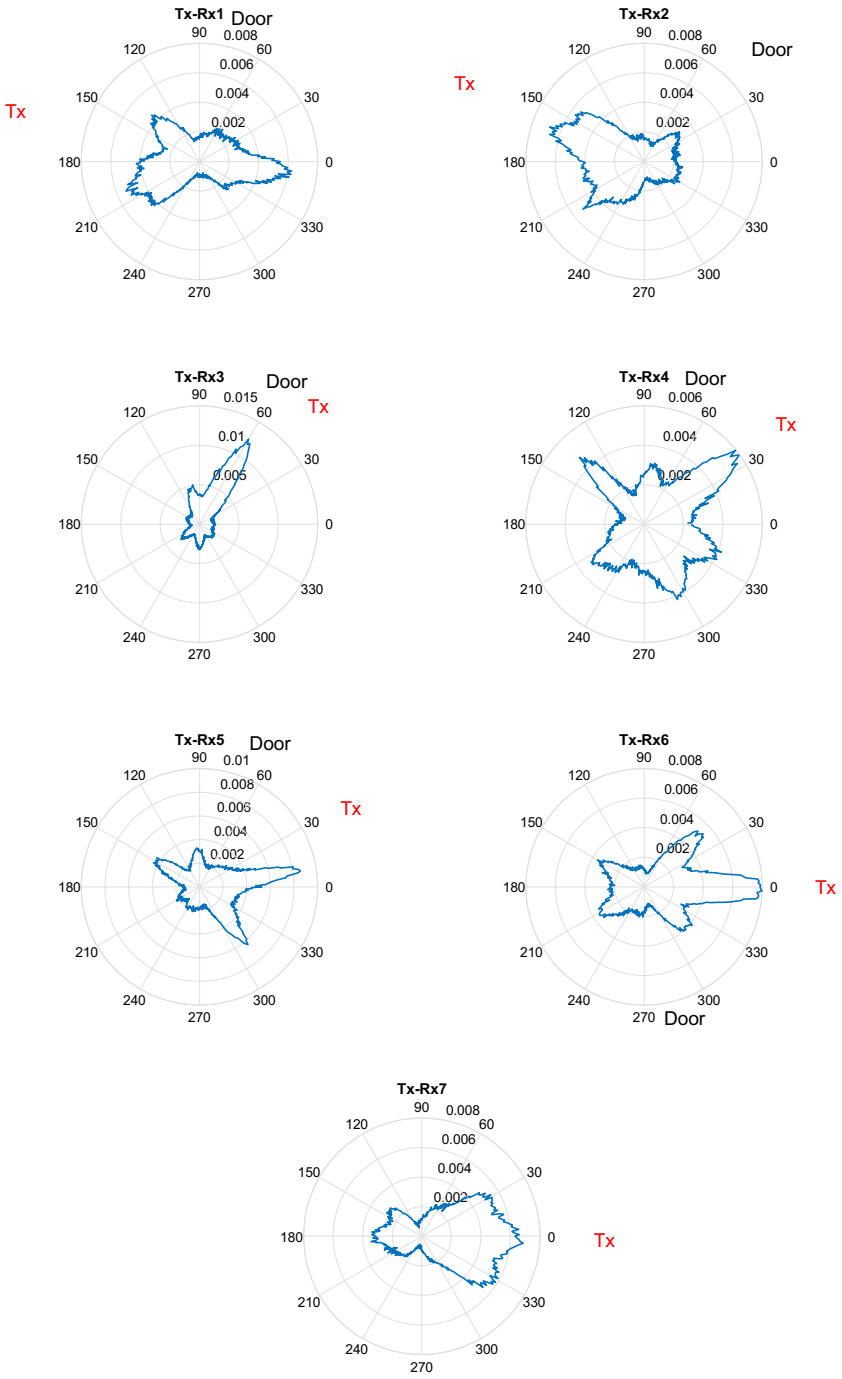

Figure 4.13: Angular Power Spectrum (Rx in different rooms)

Table 4.5: Evaluated parameters of angular distributions

Parameter	Same side	Different sides
κ_1	$p_\Gamma(16.1, 0.13)$	$p_\Gamma(7, 0.7)$
κ_2	$p_\Gamma(20.8, 0.11)$	$p_\Gamma(7, 0.17)$
w	$p_\beta(23, 13.6)$	$p_\beta(8.8, 14.8)$
c_{κ_1,κ_2}	-0.28	-0.54
$c_{\kappa_1,w}$	-0.78	-0.84
$c_{\kappa_2,w}$	0.37	0.66
τ_a	2.4 s	

Up to seven small peaks can be detected in the measurements, but modeling of all these components is not practical. For sake of simplicity, the distribution of AoA excluding the main peak can be approximated by single TvM distribution with a small parameter $\kappa_{2,diff}$. The mean angle of this component has low impact because the distribution is close to uniform when $\kappa_{2,diff}$ is small. In the case of the same-side rooms, again main peaks pointing towards the transmitter are seen in figures 4.12 and 4.13 (Rx (Tx) 6, 7). However, the peak is wider than in the case of communication between the nodes on the different sides of the corridor. Moreover, its impact is just slightly bigger than the one of backscattering. Hence, the final distribution can be approximated by two TvM distributions with parameters $\kappa_{1,same}$ and $\kappa_{2,same}$ and $|\mu_{1,same} - \mu_{2,same}| = \pi$.

To estimate the parameters $\kappa_{1,diff}, \kappa_{2,diff}, \kappa_{1,same}, \kappa_{2,same}$, we assume that the angle corresponding to the maximum of AoA distribution is the direction of LOS and shifted to 0. Consequently, $\mu_{1,same} = \mu_{1,diff} = 0$ and, considering the reasoning above, we can set $\mu_{2,same} = \mu_{2,diff} = \pi$. Next, we performed least squares fitting of the measured distributions and

$$p_{TvM}(x, w, \kappa_1, \kappa_2) = w \cdot \frac{e^{(\kappa_1 \cos(x))}}{2\pi I_0(\kappa_1)} + (1 - w) \cdot \frac{e^{(\kappa_2 \cos(x-\pi))}}{2\pi I_0(\kappa_2)}, \tag{4.13}$$

where w and $(1 - w)$ are the impacts of components. The Kolmogorov-Smirnov test with 95 $\%$ confidence interval was used to check whether the LS estimation gives an appropriate result. It turns out that $\kappa_{1,2}$ follow Gamma distributions and some correlation between the parameters was found. Parameter w is Beta-distributed (see Figure 4.14). The temporal autocorrelations of the parameters κ_1, κ_2, w is a decreasing exponential function with the decay time of 2.4 s ($\approx$ 3 stationarity periods). The evaluated parameters are listed in Table 4.5.

4.3.4 Modeling of Angular Power Spectra

The angular statistics' (and consequently the power spectra) temporal changes can be modeled using the extracted directional statistics. First, the parameters of (4.13) are generated using the autoregressive processes:

$$y_{\kappa_1}(t) = e^{-\triangle t/\tau_a} \kappa_1(t - \triangle\, t) + \sqrt{1 - e^{-2\triangle t/\tau_a}} x_{\kappa_1}(t), \tag{4.14}$$

$$y_{\kappa_2}(t) = e^{-\triangle t/\tau_a} \kappa_2(t - \triangle\, t) + \sqrt{1 - e^{-2\triangle t/\tau_a}} x_{\kappa_2}(t), \tag{4.15}$$

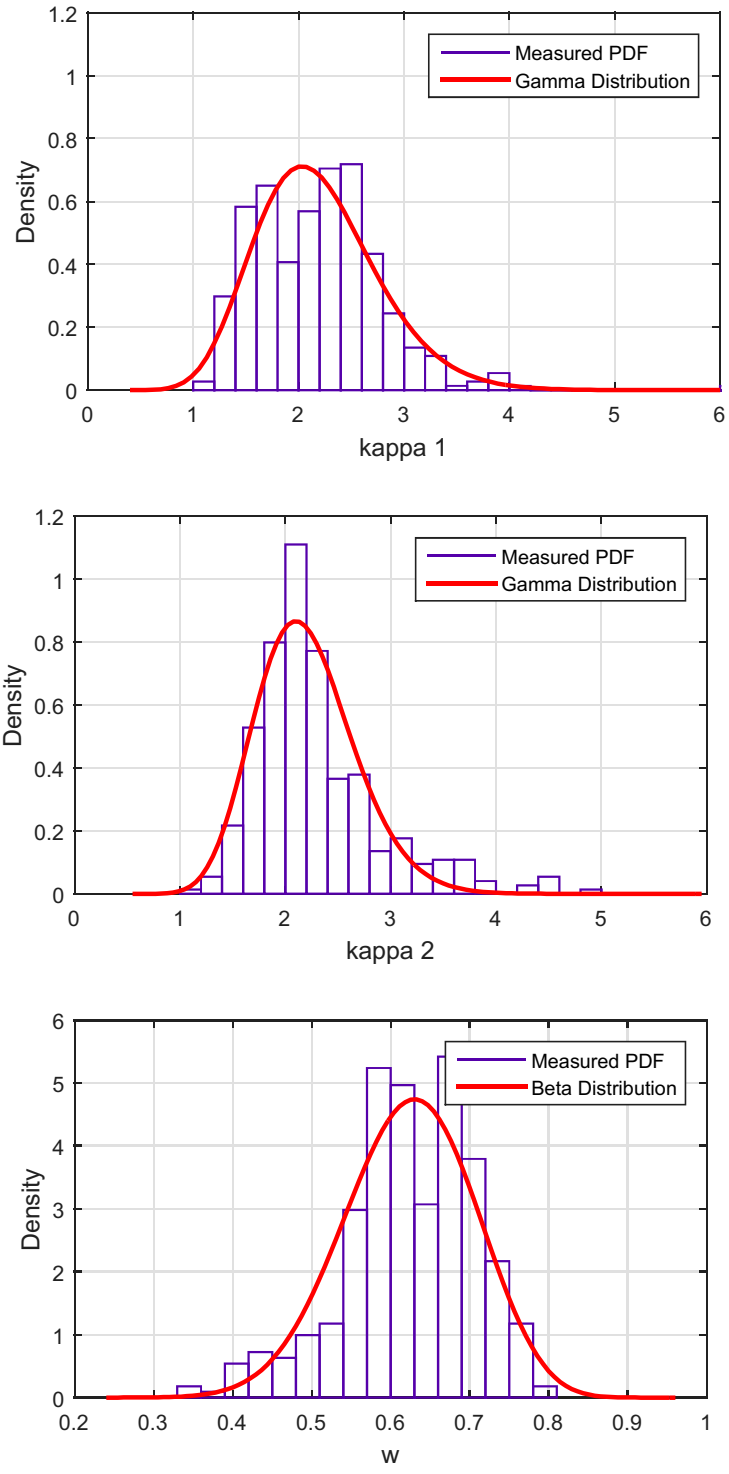

Figure 4.14: Distributions of estimated parameters (Tx and Rx are on the same side of the corridor)

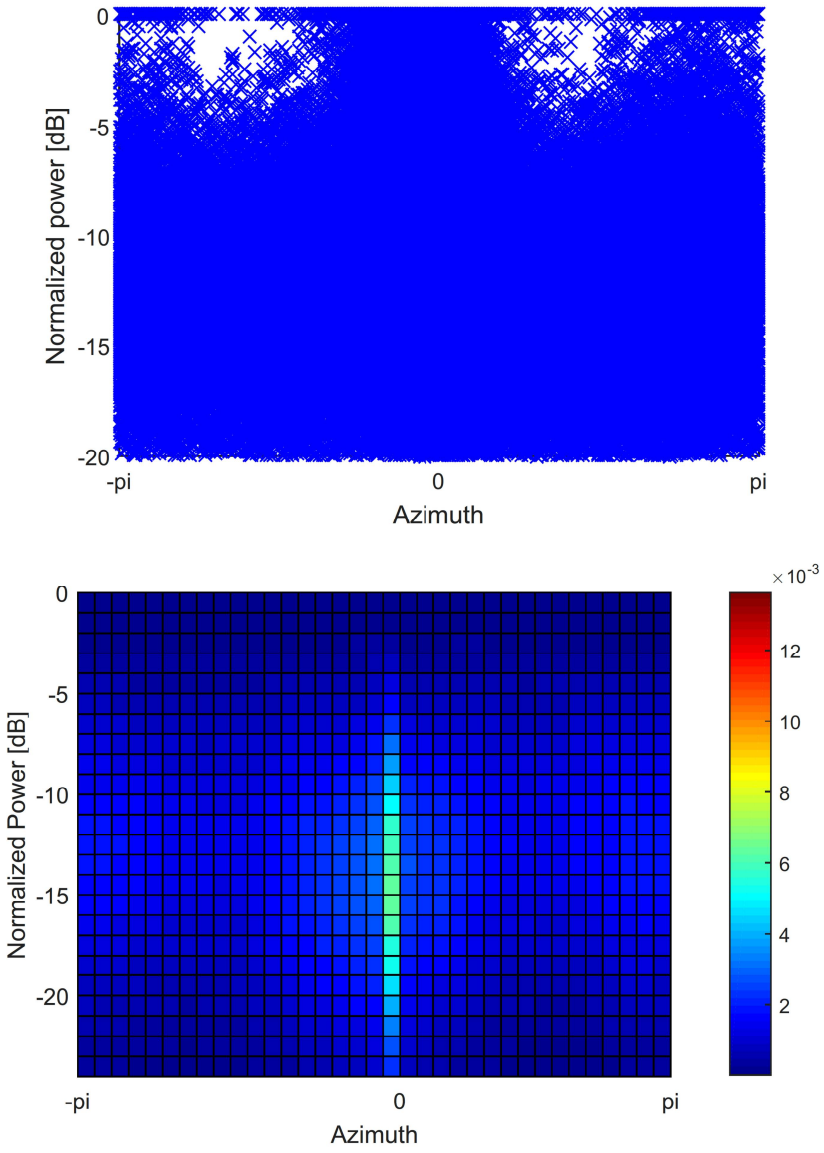

Figure 4.15: Scatter plot of power vs azimuth using the Tx1-Rx measurement (top). Density of powers vs azimuth using all the measurements.

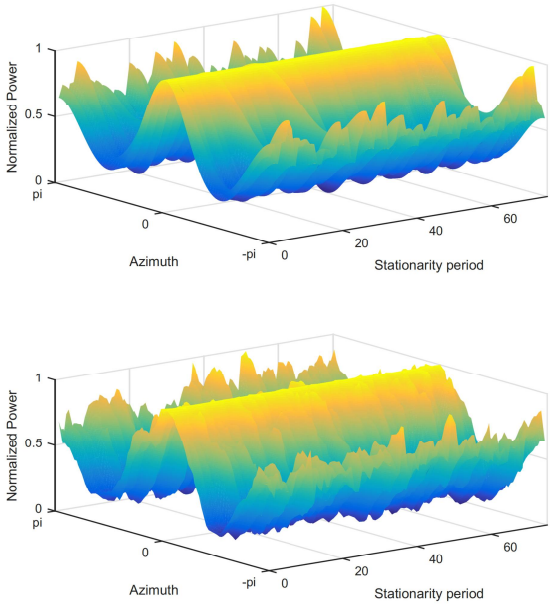

Figure 4.16: Simulated (top) and measured(bottom) time-variant Angular Power Spectrum, the nodes are on the same side of the corridor

$$y_w(t) = e^{-\Delta t/\tau_a} w(t - \triangle\, t) + \sqrt{1 - e^{-2\Delta t/\tau_a}} x_w(t), \tag{4.16}$$

where $x_{\kappa_1}(t), x_{\kappa_2}(t)$ and $x_w(t)$, are time series drawn from the appropriate distributions (see Table 4.5) and $\triangle\, t$ equals the stationarity period.

The full correlation matrices composed of the elements shown in Table 4.5 satisfy a positive semi-definiteness constraint and they are symmetric. We,finally can correlate the time series at each time t as

$$\begin{bmatrix} \kappa_1(t) \\ \kappa_2(t) \\ w(t) \end{bmatrix} = \mathbf{L} \begin{bmatrix} y_{\kappa_1}(t) \\ y_{\kappa_2}(t) \\ y_w(t) \end{bmatrix}, \tag{4.17}$$

where $\mathbf{L}$ is the Cholesky decomposition of the full correlation matrix.

Figure 4.15 a shows a scatter plot of normalized MPC power against azimuth. Powers are normalized so that the power of LOS component equals to 0 dB. It is observed that the normalized MPC power does not depend on MPC azimuth, but the density of paths does depend on angles (see Figure 4.15 b). In other words, the observed shape of APS is caused by the path's density. So that, when temporal evolution of the angular distribution's parameters are modeled, we can obtain correspondent time-variant Angular Power Spectrum. Examples of obtained APS are shown in Figures 4.16 and 4.17.

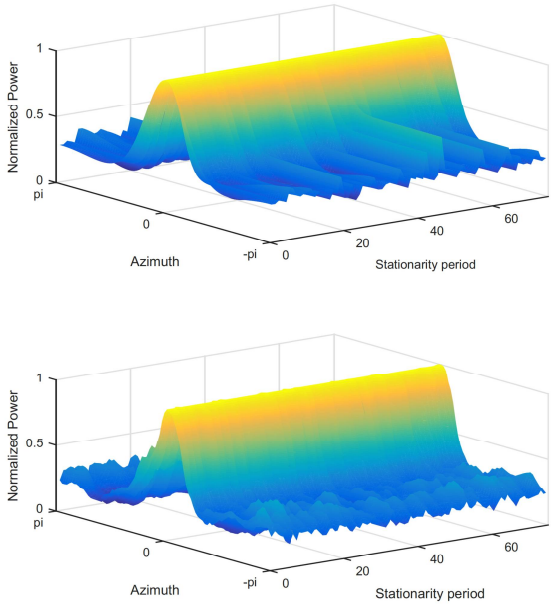

Figure 4.17: Simulated (top) and measured(bottom) time-variant Angular Power Spectrum, the nodes are on different sides of the corridor

4.4 Generalized Reference Double-Ring Model for SOSF channels

In this chapter we consider a narrowband MIMO communication system with $\mathcal{A}_T$ transmit and $\mathcal{A}_R$ receive omnidirectional antenna elements.

It is shown in [58] that the double-ring geometry can be used to model MIMO channels in indoor environments. The geometry of the proposed model is shown in Figure 4.18 a and b for the cases of double- and single-bouncing, respectively. Transmitter (Tx) and receiver (Rx) are denoted by 0_T and 0_R, respectively; R_T and R_R are radii of rings which are formed by scatterers $S_T^m(m = 1, 2, \dots M)$ and $S_R^n(n = 1, 2, \dots N)$ located around the transmitter and the receiver. The spacing between two adjacent antenna elements at the Tx and Rx is denoted by δ_T and δ_R. Angles α_T^m and α_T^n denote the angles of departure (AoD) of the transmitting waves scattered from the scatterers S_T^m and S_R^n, whereas α_R^m and α_R^n are the angles of arrival (AoA) of the receiving waves that impinge on S_T^m and S_R^n, respectively. Angles θ_T and θ_R describe the orientation of the Tx and Rx antenna array, respectively, relative to the x-axis.

The following assumptions are made: (i) the Tx and Rx are moving with speeds v_t and v_r in directions described by angles γ_T and γ_R for the transmitter and the receiver, respectively; (ii) the distance between Tx and Rx is much larger than the radii R_T and

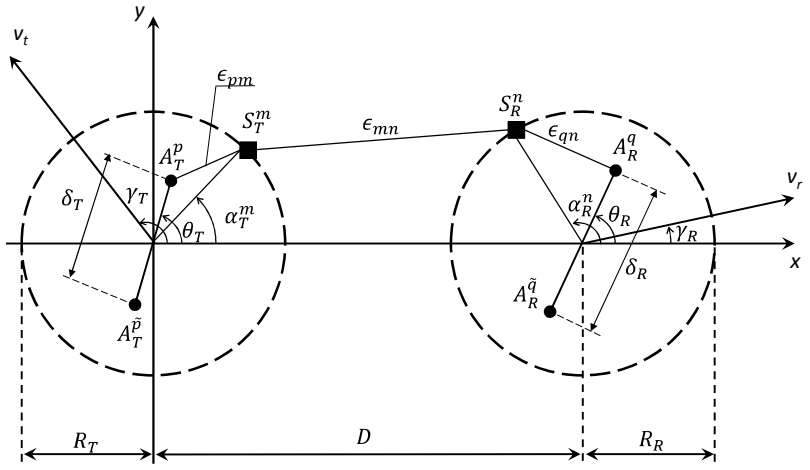

(a) Double Bouncing

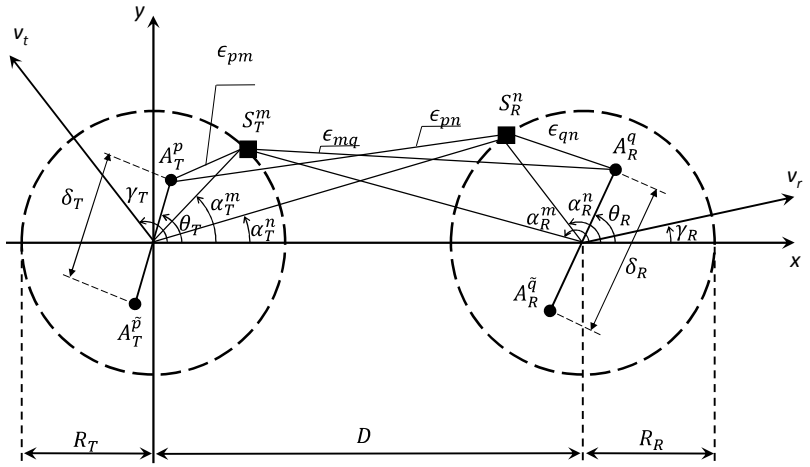

(b) Single Bouncing

Figure 4.18: The geometrical double-ring model

R_R, i.e. $\max(R_T, R_R) \ll D$; (iii) δ_T and δ_R are much smaller than the radii R_T and R_R, i.e., $\max\{\delta_T, \delta_R\} \ll \min\{R_T, R_R\}$; (iv) the angles α_T^m and α_R^n are random variables following the distribution described by (4.13); (v) for short periods of time, the mobile environment can be assumed as quasi-stationary, i.e. the rings of scatterers are fixed.

The expressions for the distances which a plane wave travels in the case of so-called double bounce scattering ($\epsilon_{pm}, \epsilon_{mn}, \epsilon_{qn}$ in Figure 4.18 a) and single bounce scattering ($\epsilon_{pm}, \epsilon_{mq}, \epsilon_{pn}, \epsilon_{qn}$ in Figure 4.18 b) can be found in [58]

$$\epsilon_{pm} = R_t - (0.5\mathcal{A}_t + 0.5 - p)\delta_T \cos(\theta_T - \alpha_T^m),$$

$$\epsilon_{mq} = D - (0.5\mathcal{A}_r + 0.5 - q)\delta_R\Big[\Delta_T \sin theta_T \sin\alpha_T^m - \cos\theta_R\Big],$$
$$\epsilon_{pn} = D - (0.5\mathcal{A}_t + 0.5 - p)\delta_T\Big[\Delta_R \sin\theta_T \sin\alpha_R^n + \cos\theta_T\Big],$$
$$\epsilon_{nq} = R_r - (0.5\mathcal{A}_r + 0.5 - q)\delta_r \cos(\alpha_R^n - \theta_R),$$
$$\epsilon_{mn} \approx D,$$
$$\epsilon_{pq} = D - (0.5\mathcal{A}_t + 0.5 - p)\delta_t \cos\theta_R - (0.5\mathcal{A}_r + 0.5 - q)\delta_r \cos(\alpha_{Rq}^{LoS} - \theta_R),$$

where p and q are the antenna's numbers, $\Delta_T = \frac{R_t}{D}$ and $\Delta_R = \frac{R_r}{D}$.

The complex faded envelop of the link from the transmit antenna element A_p to the receive antenna element A_q can be expressed as:

$$\begin{aligned} h^{pq}(t) =& \omega_0 h_{LOS}^{pq}(t) + \omega_{SBR} h_{SBR}^{pq}(t) + \omega_{SBT} h_{SBT}^{pq}(t) \\ &+ \omega_{DB} h_{DB}^{pq}(t) + \omega_{DBI} h_{DBI}^{pq}(t), \end{aligned} \tag{4.18}$$

where $h_{LOS}^{pq}(t)$ denotes the LOS term; $h_{SBR}^{pq}(t)$ and $h_{SBT}^{pq}(t)$ are the components caused by single bounce scattering at the scatterers around the receiver and the transmitter, respectively; $h_{DB}^{pq}(t)$ and $h_{DBI}^{pq}(t)$ are the components caused by double bounce scattering under conditions of correlated and independent[1] scattering, respectively. The various ω are the corresponding weights.

By proceeding as in [58], we can express the components of (4.18) as:

$$\begin{aligned} h_{LOS}^{pq}(t) =& e^{j2\pi t f_T^{max}\cos\left(\pi - \alpha_{Rq}^{LOS} - \gamma_T\right) - j\frac{2\pi}{\lambda}\epsilon_{pq}} \\ &\times e^{j2\pi t f_R^{max}\cos\left(\alpha_{Rq}^{LOS} - \gamma_R\right)}, \end{aligned} \tag{4.19}$$

$$\begin{aligned} h_{SBT}^{pq}(t) =& \lim_{M\to\infty} \frac{1}{\sqrt{M}} \sum_{m=1}^{M} e^{j\phi_m - j\frac{2\pi}{\lambda}(\epsilon_{pm} + \epsilon_{mq})} \\ &\times e^{j2\pi t(f_T^{max}\cos(\alpha_T^m - \gamma_T) + f_R^{max}\cos(\alpha_R^m - \gamma_R))}, \end{aligned} \tag{4.20}$$

$$\begin{aligned} h_{SBR}^{pq}(t) =& \lim_{N\to\infty} \frac{1}{\sqrt{N}} \sum_{n=1}^{N} e^{j\phi_n - j\frac{2\pi}{\lambda}(\epsilon_{pn} + \epsilon_{nq})} \\ &\times e^{j2\pi t(f_T^{max}\cos(\alpha_T^n - \gamma_T) + f_R^{max}\cos(\alpha_R^n - \gamma_R))}, \end{aligned} \tag{4.21}$$

$$\begin{aligned} h_{DB}^{pq}(t) =& \lim_{\substack{N\to\infty \\ M\to\infty}} \frac{1}{\sqrt{MN}} \sum_{n=1}^{N}\sum_{m=1}^{M} e^{j\phi_{mn} - j\frac{2\pi}{\lambda}(\epsilon_{pm} + \epsilon_{mn} + \epsilon_{nq})} \\ &\times e^{j2\pi t(f_T^{max}\cos(\alpha_T^m - \gamma_T) + f_R^{max}\cos(\alpha_R^n - \gamma_R))}. \end{aligned} \tag{4.22}$$

By using the results in [43], [58] for the case of independent scatterers, we obtain

$$\begin{aligned} &h_{DBI}^{pq}(t) = \\ &\lim_{N\to\infty} \frac{1}{\sqrt{N}} \sum_{n=1}^{N} e^{j\left(\phi_n - \frac{2\pi}{\lambda}\epsilon_{nq}\right)} \times e^{j2\pi t f_R^{max}\cos(\alpha_R^n - \gamma_R)} \\ &\times \lim_{M\to\infty} \frac{1}{\sqrt{M}} \sum_{m=1}^{M} e^{j\left(\phi_m - \frac{2\pi}{\lambda}\epsilon_{pm}\right)} \times e^{j2\pi t f_T^{max}\cos(\alpha_T^m - \gamma_T)}. \end{aligned} \tag{4.23}$$

[1] i.e when the phase shifts caused by joint interaction of the scatterers S_T^m and S_R^n can be expressed as $\phi_{mn} = \phi_m + \phi_n$

Since the central limit theorem states that each single sum is a zero-mean complex Gaussian process with unit variance, the envelopes $g_{DB}^{pq}(t) = |h_{DB}^{pq}(t)|$, $g_{SBR}^{pq}(t) = |h_{SBR}^{pq}(t)|$ and $g_{SBT}^{pq}(t) = |h_{SBT}^{pq}(t)|$ are all characterized by Rayleigh distributions whereas the envelope $g_{DBI}^{pq}(t) = |h_{DBI}^{pq}(t)|$ enables to reproduce the Double-Rayleigh distribution, so that ω_{DBI} can be identified to ω_2 in (1.36). The Rayleigh term in (1.36) is made of the combination of all other components. Proceeding as in [43], we may set $\omega_{DB} = \omega_{SBT} = \omega_{SBR} = \frac{\omega_1}{\sqrt{3}}$, assuming that all three mechanisms are occurring with the same probability. Finally, $\omega_{LOS} = \omega_0$, so that we can express (4.18) as

$$\begin{aligned} h^{pq}(t) = \omega_0 h_{LOS}^{pq}(t) \\ + \frac{\omega_1}{\sqrt{3}} \cdot \left(h_{DB}^{pq}(t) + h_{SBT}^{pq}(t) + h_{SBR}^{pq}(t)\right) \\ + \omega_2 \cdot h_{DBI}^{pq}(t). \end{aligned} \tag{4.24}$$

Note, that the envelope's distribution of (4.23) does not depend on mobility, so small-scale fading produced by (4.24) is SOSF distributed.

Using the approach described by Figure 4.11, time-variant statistics of the SOSF channel (i.e weights ω_0, ω_1 and ω_2) can be modeled.

4.4.1 Spatial Correlation Function

Using the approach in [92], the space-time correlation function can be derived. The normalized spatial correlation function between two complex fading envelopes $h^{pq}(t)$ and $h^{\tilde{p}\tilde{q}}(t)$ can be written as

$$\begin{aligned} R^{pq,\tilde{p}\tilde{q}}(\delta_T, \delta_R) = \omega_0^2 \cdot R_{LOS}^{pq,\tilde{p}\tilde{q}}(\delta_T, \delta_R) \\ + \frac{\omega_1^2}{3} \cdot \left[R_{SBT}^{pq,\tilde{p}\tilde{q}}(\delta_T, \delta_R) + R_{SBR}^{pq,\tilde{p}\tilde{q}}(\delta_T, \delta_R) + R_{DB}^{pq,\tilde{p}\tilde{q}}(\delta_T, \delta_R) \right] \\ + \omega_2^2 \cdot R_{DBI}^{pq,\tilde{p}\tilde{q}}(\delta_T, \delta_R). \end{aligned} \tag{4.25}$$

When the azimuth statistics derived in the previous section are used, the components $R_{SBR}^{pq,\tilde{p}\tilde{q}}(\delta_T, \delta_R)$, $R_{SBT}^{pq,\tilde{p}\tilde{q}}(\delta_T, \delta_R)$, $R_{DB}^{pq,\tilde{p}\tilde{q}}(\delta_T, \delta_R)$ and $R_{DBI}^{pq,\tilde{p}\tilde{q}}(\delta_T, \delta_R)$ can be expressed as

$$\begin{aligned} R_{LOS}^{pq,\tilde{p}\tilde{q}}(\delta_T, \delta_R) = e^{\frac{j2\pi}{\lambda}(\delta_T \cos\theta_T - \delta_R \cos\theta_R)} \\ \times e^{j2\pi(f_T^{max}\cos\gamma_T - f_R^{max}\cos\gamma_R)}, \end{aligned} \tag{4.26}$$

$$\begin{aligned} R_{SBT}^{pq,\tilde{p}\tilde{q}}(\delta_T, \delta_R) = e^{-\frac{j2\pi}{\lambda}((\tilde{q}-q)\delta_R \cos\theta_R - j2\pi\tau f_R^{max}\cos\gamma_R)} \\ \left[\frac{w I_0\left(\sqrt{a_{SBT,1}^2 + b_{SBT,1}^2}\right)}{I_0(\kappa_{1,T})} + \frac{(1-w) I_0\left(\sqrt{a_{SBT,2}^2 + b_{SBT,2}^2}\right)}{I_0(\kappa_{2,T})} \right], \end{aligned} \tag{4.27}$$

$$\begin{aligned} R_{SBR}^{pq,\tilde{p}\tilde{q}}(\delta_T, \delta_R) = e^{-\frac{j2\pi}{\lambda}((\tilde{p}-p)\delta_T \cos\theta_T - j2\pi\tau f_T^{max}\cos\gamma_T)} \\ \left[\frac{w I_0\left(\sqrt{a_{SBR,1}^2 + b_{SBR,1}^2}\right)}{I_0(\kappa_{1,T})} + \frac{(1-w) I_0\left(\sqrt{a_{SBR,2}^2 + b_{SBR,2}^2}\right)}{I_0(\kappa_{2,T})} \right], \end{aligned} \tag{4.28}$$

$$R_{DB}^{pq,\tilde{p}\tilde{q}}(\delta_T,\delta_R)=R_{DBI}^{pq,\tilde{p}\tilde{q}}(\delta_T,\delta_R)=\frac{wI_0\left(\sqrt{a_{DB,1}^2+b_{DB,1}^2}\right)I_0\left(\sqrt{c_{DB,1}^2+d_{DB,1}^2}\right)}{I_0\left(\kappa_{1,T}\right)I_0\left(\kappa_{1,R}\right)} + \frac{(1-w)I_0\left(\sqrt{a_{DB,2}^2+b_{DB,2}^2}\right)I_0\left(\sqrt{c_{DB,2}^2+d_{DB,2}^2}\right)}{I_0\left(\kappa_{2,T}\right)I_0\left(\kappa_{2,R}\right)}, \tag{4.29}$$

where

$$a_{SBT,1(2)}=\frac{j2\pi}{\lambda}(\tilde{p}-p)\delta_T\cos\theta_T-2\pi\tau f_T^{max}\cos\gamma_T+\kappa_{1(2),T},$$

$$\begin{aligned}b_{SBT,1(2)}=&\frac{j2\pi}{\lambda}\left[(\tilde{p}-p)\delta_T\sin\theta_T+(\tilde{q}-q)\delta_R\Delta_T\sin\theta_R\right]\\&-2\pi\tau(f_T^{max}\sin\gamma_T+f_R^{max}\Delta_T\sin\gamma_R),\end{aligned}$$

$$a_{SBR,1(2)}=\frac{j2\pi}{\lambda}(\tilde{q}-q)\delta_R\cos\theta_R-2\pi\tau f_R^{max}\cos\gamma_R+\kappa_{1(2),R},$$

$$\begin{aligned}b_{SBT,1(2)}=&\frac{j2\pi}{\lambda}\left[(\tilde{p}-p)\delta_T\Delta_R\sin\theta_T+(\tilde{q}-q)\delta_R\sin\theta_R\right]\\&-2\pi\tau(f_T^{max}\Delta_R\sin\gamma_T+f_R^{max}\sin\gamma_R),\end{aligned}$$

$$a_{DB,1(2)}=j2\pi\tau f_T^{max}\cos\gamma_T+\frac{j2\pi}{\lambda}(\tilde{p}-p)\delta_T\cos\theta_T+\kappa_{1(2),T},$$

$$b_{DB,1(2)}=-j2\pi\tau f_T^{max}\sin\gamma_T+\frac{j2\pi}{\lambda}(\tilde{p}-p)\delta_T\sin\theta_T,$$

$$c_{DB,1(2)}=\frac{j2\pi}{\lambda}(\tilde{q}-q)\delta_R\cos\theta_R-2\pi\tau f_R^{max}\cos\gamma_R+\kappa_{1(2),R},$$

$$d_{DB,1(2)}=\frac{j2\pi}{\lambda}(\tilde{q}-q)\delta_R\sin\theta_R-2\pi\tau f_R^{max}\sin\gamma_R.$$

Many existing correlation functions, including the ones presented in Chapters 1 and 3, are special cases the space-time correlation function presented in (4.25)-(4.29). By setting $\kappa_{1,T(R)}=\kappa_{2,T(R)}=0$, isotropic scattering around the transmitter (receiver) can be modeled, the expressions for single and double mobile channels can be obtained by the appropriate choice of f_T^{max} and f_R^{max} etc.

Expressions (4.27)-(4.29) are general for any number of the antennas $\mathcal{A}_T$ and $\mathcal{A}_R$. Consequently, the spatial correlation function components in the case of SIMO channels will be

$$R_{SBT}^{1q,1\tilde{q}}(\delta_R)=z_{SBT}\left[\frac{wI_0\left(\sqrt{a_{SBT,1}^2+b_{SBT,1}^2}\right)}{I_0\left(\kappa_{1,T}\right)} + \frac{(1-w)I_0\left(\sqrt{a_{SBT,2}^2+b_{SBT,2}^2}\right)}{I_0\left(\kappa_{2,T}\right)}\right], \tag{4.30}$$

$$R_{SBR}^{1q,1\tilde{q}}(\delta_R) = z_{SBR}\left[\frac{wI_0\left(\sqrt{a_{SBR,1}^2 + b_{SBR,1}^2}\right)}{I_0\left(\kappa_{1,T}\right)} + \frac{(1-w)I_0\left(\sqrt{a_{SBR,2}^2 + b_{SBR,2}^2}\right)}{I_0\left(\kappa_{2,T}\right)}\right], \tag{4.31}$$

where

$$z_{SBT} = e^{-j\frac{2\pi}{\lambda}(\tilde{q}-q)\delta_R\cos\theta_R},$$

$$z_{SBR} = e^{-j2\pi\tau f_T^{max}\cos\gamma_T|},$$

$$a_{SBT,1(2)} = \frac{j2\pi}{\lambda}2\pi\tau f_T^{max}\cos\gamma_T + \kappa_{1(2),T},$$

$$b_{SBT,1(2)} = \frac{j2\pi}{\lambda}(\tilde{q}-q)\delta_R\Delta_T\sin\theta_R - 2\pi\tau f_T^{max}\sin\gamma_T,$$

$$a_{SBR,1(2)} = \frac{j2\pi}{\lambda}(\tilde{q}-q)\delta_R\cos\theta_R + \kappa_{1(2),R},$$

$$b_{SBT,1(2)} = \frac{j2\pi}{\lambda}(\tilde{q}-q)\delta_R\sin\theta_R - 2\pi\tau f_T^{max}\Delta_R\sin\gamma_T.$$

Equation (4.29) does not change, however its elements are expressed as

$$a_{DB,1(2)} = j2\pi\tau f_T^{max}\cos\gamma_T + \kappa_{1(2),T},$$

$$b_{DB,1(2)} = -j2\pi\tau f_T^{max}\sin\gamma_T,$$

$$c_{DB,1(2)} = \frac{j2\pi}{\lambda}(\tilde{q}-q)\delta_R\cos\theta_R + \kappa_{1(2),R},$$

$$d_{DB,1(2)} = \frac{j2\pi}{\lambda}(\tilde{q}-q)\delta_R\sin\theta_R.$$

4.5 Time-Series Model

4.5.1 Path-Loss and Mean Large-Scale Fading

In analogy with narrowband single antenna channels, the combined path-loss and mean LS fading $\Lambda = \Lambda' + \overline{S}$ can be defined as

$$\Lambda = \Lambda_0 + \eta \cdot 10\log_{10}\left(\frac{d}{d_0}\right) + \overline{S}, \tag{4.32}$$

where Λ_0 is the deterministic path-loss at the reference distance $d_0 = 1$m and $\overline{S}$ is found to be normal with zero mean (when expressed in decibels) over the whole set of measured channels. The deterministic path-loss at the reference distance Λ_0, the path-loss exponent η and the standard deviation $\sigma_{\overline{s}}$ characterizing distribution of $\overline{S}$ have been estimated from the data (see Table 4.6).

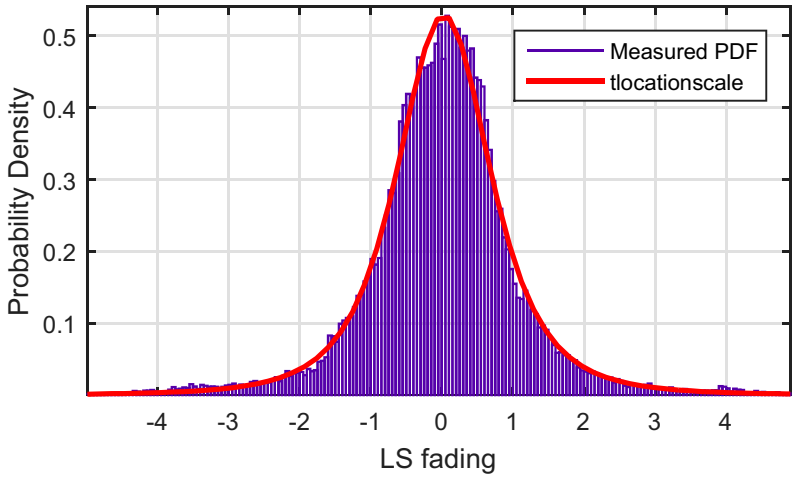

(a) Single mobile, limited motion

Figure 4.19: Fit of the T-location scale distribution to measured LS fading

Table 4.6: Model parameters for path-loss and LS fading

Parameter	Value	Parameter	Value
$\sigma_{\tilde{s}}$	0.7	$\tau_{\tilde{s}}$	6.5 [s]
ν	3	Λ_0	56 [dB]
η	3	$\sigma_{\bar{s}}$	3.6

4.5.2 Dynamic Large-Scale Fading

When the deterministic path-loss and mean LS fading are removed and small-scale fading is averaged out, the remaining variations are due to dynamic LS fading, as detailed earlier. In line with previous results, the dynamic LS fading might be described by a t-location scale distribution with zero-mean ($\mu = 0$) by definition, $\nu = 3$ degrees of freedom and a scale parameter $\sigma_{\tilde{s}}$ (see Table 4.6). Fitting of Normal and t-location scale distributions to measured data is shown in Figure 4.19.

The dynamic LS fading autocorrelation over time is modeled as a decreasing exponential, whose decay time $\tau_{\tilde{s}}$ is also shown in Table 4.6. Hence, we use an autoregressive process to generate autocorrelated dynamic LS fading values,

$$\tilde{S}(t) = e^{-\Delta t/\tau_{\tilde{s}}}\tilde{S}(t- \triangle\, t) + \sqrt{1 - e^{-2\Delta t/\tau_{\tilde{s}}}}x_{\tilde{s}}(t), \tag{4.33}$$

where $x_{\tilde{s}}$ is a time series of length T, whose values are drawn independently from the distributions described by Table 4.6 and $\triangle\, t$ equals the stationarity period.

No correlation between dynamic LS fading and the SS fading states has been found, so that we can combine independently simulated dynamic LS fading and small-scale fading realizations.

4.5.3 Small-Scale Fading

The reference model described in Section 4.4 assumes an infinite number of scatterers, which cannot be applied in a practical simulation model. Hence, it is necessary to propose a model with a finite number of scatterers, while still matching with the statistical properties. The complex faded envelope (4.18) can be written as

$$\begin{aligned}
h^{pq}(t) =&\omega_0 \Re\{h^{pq}_{LOS}(t)\} + \omega_{SBR}\Re\{h^{pq}_{SBR}(t)\} + \omega_{SBT}\Re\{h^{pq}_{SBT}(t)\} \\
&+\omega_{DB}\Re\{h^{pq}_{DB}(t)\} + \omega_{DBI}\Re\{h^{pq}_{DBI}(t)\} \\
&\; j\Big[\omega_0 \Im\{h^{pq}_{LOS}(t)\} + \omega_{SBR}\Im\{h^{pq}_{SBR}(t)\} + \omega_{SBT}\Im\{h^{pq}_{SBT}(t)\} \\
&+\omega_{DB}\Im\{h^{pq}_{DB}(t)\} + \omega_{DBI}\Im\{h^{pq}_{DBI}(t)\}\Big] \\
=&\omega_0 h^{pq(I)}_{LOS}(t) + \omega_{SBR}h^{pq(I)}_{SBR}(t) + \omega_{SBT}h^{pq(I)}_{SBT}(t) \\
&+\omega_{DB}h^{pq(I)}_{DB}(t) + \omega_{DBI}h^{pq(I)}_{DBI}(t) \\
&\; j\Big[\omega_0 h^{pq(Q)}_{LOS}(t) + \omega_{SBR}h^{pq(Q)}_{SBR}(t) + \omega_{SBT}h^{pq(Q)}_{SBT}(t) \\
&+\omega_{DB}h^{pq(Q)}_{DB}(t) + \omega_{DBI}h^{pq(Q)}_{DBI}(t)\Big],
\end{aligned} \tag{4.34}$$

where $\Re$ and $\Im$ denote real and imaginary operations, respectively. By proceeding as in [58], we can express the components of (4.34) as:

$$\begin{aligned}
h^{pq(I)}_{LOS}(t) =& \cos\Big[2\pi t f^{max}_T \cos\left(\pi - \alpha^{LOS}_{Rq} - \gamma_T\right) \\
&+ 2\pi t f^{max}_R \cos\left(\alpha^{LOS}_{Rq} - \gamma_R\right) - \frac{2\pi}{\lambda}\epsilon_{pq}\Big],
\end{aligned} \tag{4.35}$$

$$\begin{aligned}
h^{pq(I)}_{SBT}(t) = \frac{1}{\sqrt{M}}\sum_{m=1}^{M} &\cos\Big[\xi_m - l_q - 2\pi t f^{max}_R \cos\gamma_R\Big]\cos\Big[l_p\cos\left(\theta_T - \alpha^m_T\right) \\
&+ 2\pi t f^{max}_T \cos\left(\alpha^m_T - \gamma_T\right) + l_q\Delta_T \sin\theta_R \sin\alpha^m_T \\
&+ 2\pi t f^{max}_R \Delta_T \sin\gamma_R \sin\alpha^m_T + \phi_m\Big],
\end{aligned} \tag{4.36}$$

$$\begin{aligned}
h^{pq(I)}_{SBR}(t) = \frac{1}{\sqrt{N}}\sum_{n=1}^{N} &\cos\Big[\xi_n + l_p + 2\pi t f^{max}_T \cos\gamma_T\Big]\cos\Big[l_q\cos\left(\alpha^n_R - \theta_R\right) \\
&+ 2\pi t f^{max}_R \cos\left(\alpha^n_R - \gamma_R\right) + l_p\Delta_R \sin\theta_T \sin\alpha^n_R \\
&+ 2\pi t f^{max}_T \Delta_R \sin\gamma_T \sin\alpha^n_R + \phi_n\Big],
\end{aligned} \tag{4.37}$$

$$\begin{aligned}
h^{pq(I)}_{DB}(t) = \frac{1}{\sqrt{NM}}\sum_{n,m=1}^{N,M} &\cos\Big[l_p\cos\left(\theta_T - \alpha^m_T\right) + 2\pi t f^{max}_T \cos\left(\alpha^m_T - \gamma_T\right)\Big] \\
&\cos\Big[l_q\cos\left(\alpha^n_R - \theta_R\right) + 2\pi t f^{max}_R \cos\left(\alpha^n_R - \gamma_R\right) + \phi_{mn}\Big],
\end{aligned} \tag{4.38}$$

$$h_{DBI}^{pq(I)}(t) = \frac{1}{\sqrt{NM}} \sum_{n=1}^{N} \cos\left[l_q \cos\left(\alpha_R^n - \theta_R\right) + 2\pi t f_R^{max} \cos\left(\alpha_R^n - \gamma_R\right) + \phi_n\right] \times \sum_{m=1}^{M} \cos\left[l_p \cos\left(\theta_T - \alpha_T^m\right) + 2\pi t f_T^{max} \cos\left(\alpha_T^m - \gamma_T\right) + \phi_m\right], \tag{4.39}$$

$$h_{LOS}^{pq(Q)}(t) = \sin\Big[2\pi t f_T^{max} \cos\left(\pi - \alpha_{Rq}^{LOS} - \gamma_T\right) + 2\pi t f_R^{max} \cos\left(\alpha_{Rq}^{LOS} - \gamma_R\right) - \frac{2\pi}{\lambda}\epsilon_{pq}\Big], \tag{4.40}$$

$$h_{SBT}^{pq(Q)}(t) = \frac{1}{\sqrt{M}} \sum_{m=1}^{M} \sin\left[\xi_m - l_q - 2\pi t f_R^{max} \cos\gamma_R\right] \cos\Big[l_p \cos\left(\theta_T - \alpha_T^m\right) + 2\pi t f_T^{max} \sin\left(\alpha_T^m - \gamma_T\right) + l_q \Delta_T \sin\theta_R \cos\alpha_T^m + 2\pi t f_R^{max} \Delta_T \sin\gamma_R \cos\alpha_T^m + \phi_m\Big], \tag{4.41}$$

$$h_{SBR}^{pq(Q)}(t) = \frac{1}{\sqrt{N}} \sum_{n=1}^{N} \sin\left[\xi_n + l_p + 2\pi t f_T^{max} \cos\gamma_T\right] \cos\Big[l_q \sin\left(\alpha_R^n - \theta_R\right) + 2\pi t f_R^{max} \sin\left(\alpha_R^n - \gamma_R\right) + l_p \Delta_R \sin\theta_T \cos\alpha_R^n + 2\pi t f_T^{max} \Delta_R \sin\gamma_T \cos\alpha_R^n + \phi_n\Big], \tag{4.42}$$

$$h_{DB}^{pq(Q)}(t) = \frac{1}{\sqrt{NM}} \sum_{n,m=1}^{N,M} \sin\left[l_p \cos\left(\theta_T - \alpha_T^m\right) + 2\pi t f_T^{max} \cos\left(\alpha_T^m - \gamma_T\right)\right] \sin\left[l_q \sin\left(\alpha_R^n - \theta_R\right) + 2\pi t f_R^{max} \sin\left(\alpha_R^n - \gamma_R\right) + \phi_{mn}\right], \tag{4.43}$$

$$h_{DBI}^{pq(Q)}(t) = \frac{1}{\sqrt{NM}} \sum_{n=1}^{N} \sin\left[l_q \sin\left(\alpha_R^n - \theta_R\right) + 2\pi t f_R^{max} \sin\left(\alpha_R^n - \gamma_R\right) + \phi_n\right] \times \sum_{m=1}^{M} \sin\left[l_p \cos\left(\theta_T - \alpha_T^m\right) + 2\pi t f_T^{max} \cos\left(\alpha_T^m - \gamma_T\right) + \phi_m\right], \tag{4.44}$$

where $l_q = \pi(\mathcal{A}_R + 1 - 2q)\delta_R\,\lambda$ and $l_p = \pi(\mathcal{A}_T + 1 - 2p)\delta_T\,\lambda$.

For the simulation model, phases $\phi_n, \phi_m, \phi_{nm}$ and path-gains ξ_n, ξ_m are generated as independent random variables uniformly distributed over $[-\pi, \pi)$. Numbers of scatterers $N = M = 32$. Since, the simulated channels will be compared with the measured ones, the other parameters used for simulations are $\mathcal{A}_r = 8, \mathcal{A}_T = 1, f_T^{max} = \frac{1\mathbf{m/s}}{\lambda}, f_R^{max} = 0, \delta_R = 0.5\lambda$, orientation of the antennas $\theta_R = \frac{2\pi(q-1)}{\mathcal{A}_R}$.

The angles of departure and arrival follow distribution in (4.13) with the time-variant parameters generated as it was shown in Section 4.3.4. Time-variant weights $\omega_0, \omega_1, \omega_2$ are calculated from time-variant parameters $\alpha(t), \beta(t)$ (see Figure 4.20)

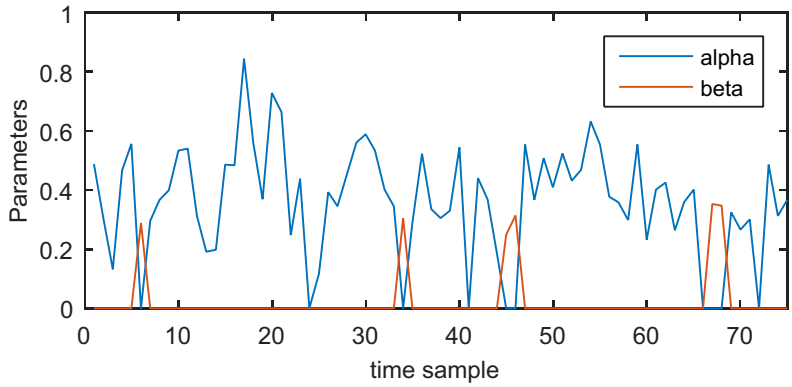

Figure 4.20: Example of simulated time-variant SOSF statistics

which are modeled as shown in Section 4.3.2. Note, that parameters $\alpha, \beta, \kappa_{1,2}, w$ are not changing within one stationarity period.

4.6 Simulations and Validation

Figure 4.21 compares the statistics of two sets of measured channels and generated channels using the model in Figure 4.23. To verify the model under different conditions similar to the ones which were used in the measurement campaign, we simulated sets channels between nodes separated by the distances listed in Table 4.2. Next, we compared the CDF of the generated small-scale fading with the CDF of measured small-scale fading. To quantify the difference between CDFs of measured and simulated small-scale fading, the mean squared error (MSE) was estimated and the asymptotic value of MSE ($4.6 \cdot 10^{-5}$) has been achieved after 6 simulation trials. Similarly, after 5-6 simulation trials, the value of Kullback-Leibler divergence becomes smaller than the threshold of 0.01.

In Section 4.3.4, model for APS has been presented as well as the visual comparison of modeled and measured APS (see Figures 4.16 and 4.17). Since the measured APS is compared with statistical realizations of APS, the agreement can be evaluated only qualitatively. However, to validate the model, second order statistics can be used: Figure 4.22 shows the cumulative distribution function of the root-mean-square azimuth direction spread. The mean of RMS distribution is similar, but still slightly higher than the one reported in [93]. The explanation of the difference can be in the fact that the environment considered in this thesis is reacher of scatterers than the large offices and laboratories investigated in [93].

Summarizing, the complete multidimensional channel model is presented in Figure 4.23: independently generated realizations of path-loss large- and small-scale fading are combined together to obtain channel realizations with time-variant statistics.

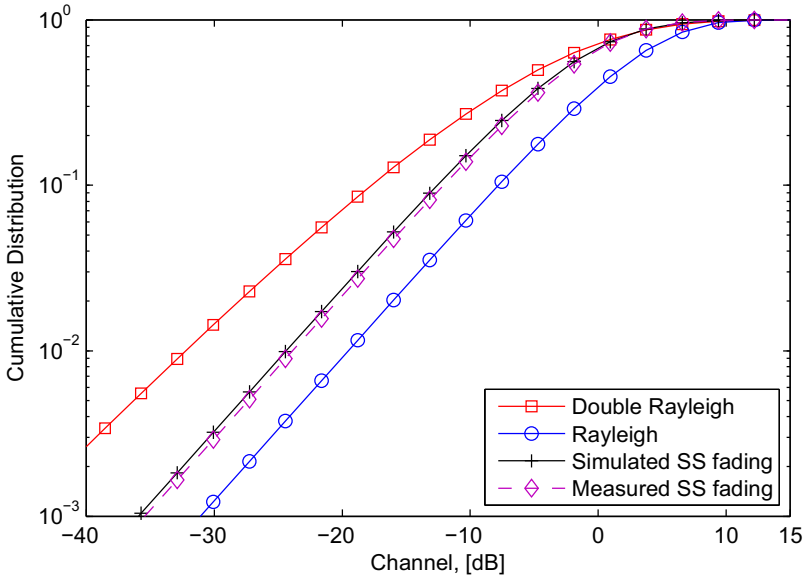

Figure 4.21: CDFs of measured and simulated small-scale fading and comparison with Rayleigh and Double Rayleigh distributions

4.7 Summary

This chapter has presented an analysis and an empirical model of time-variant channel statistics of a peer-to-peer network based on measurement in an indoor office environment at 3.8 GHz:

1. Reference and simulation models for MIMO second-order scattering fading channels have been proposed.

2. Analysis of measured Rx spatial correlation matrices shows that the minimum stationarity period equals 0.8 s.

3. Distribution of angles of arrival can be described by a bimodal Tikhonov-von Mises distribution with time-variant parameters Gamma (κ_1, κ_2) and Beta (w) distributed.

4. Small-scale fading does not depend on mobility and follows a SOSF distribution.

5. Distributions of the parameter α can be modeled by Beta distribution.

6. Distribution of the K-Factor can be well approximated by Extreme Value distribution.

7. Transitions between the fading states are described by a hidden Markov model fully parameterized from the measurements.

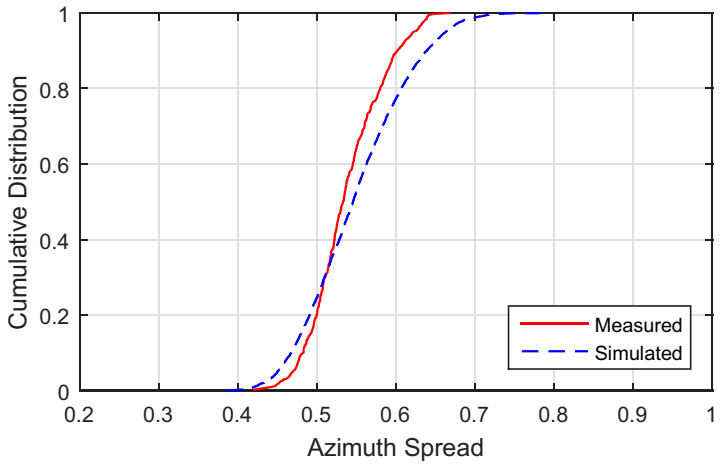

(a) same-side

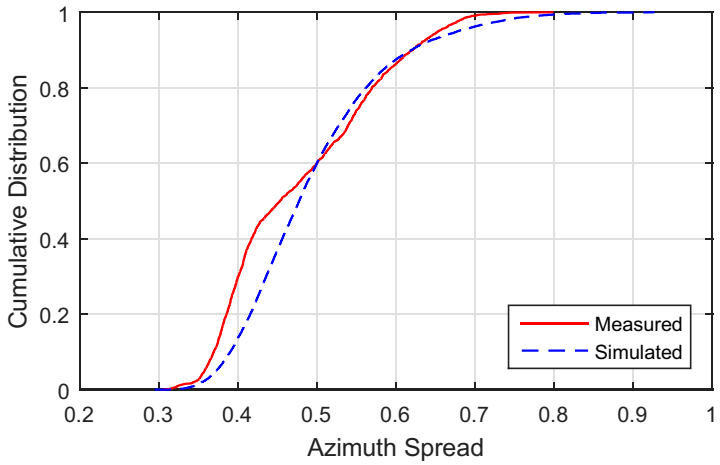

(b) same-side

Figure 4.22: Cumulative Distribution Functions of RMS azimuth direction spread.

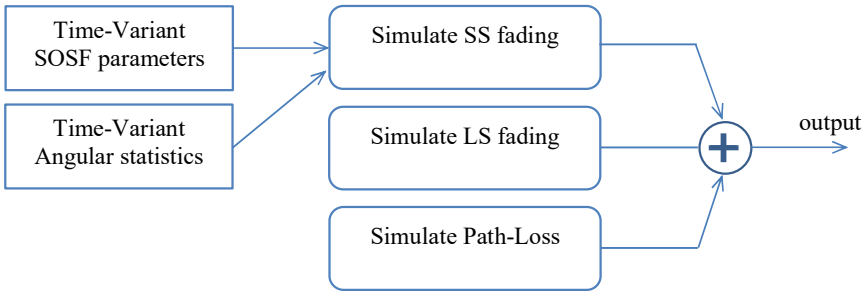

Figure 4.23: Flow-diagram of the channel model

8. As in Chapter 3 experimental dynamic LS fading distribution follows the t-location scale distribution.

9. The proposed model has been validated and good agreement between simulations using the proposed model and measurement data is obtained

Chapter 5

Wideband Channel Models

In this chapter, we propose a physical-statistical technique combining the Room Electromagnetic (REM) Theory for modeling deterministic channel components with a geometry based stochastic channel model with time-variant statistics for modeling stochastic channel components. The method enables the reconstruction of the PDP in a room-to-room dynamic scenario, including effects introduced by the mobility of the communication nodes. The main contributions are as follows:

- The prediction of the specular reflections is improved compared to [94] since e.g., the motion of the transceivers is accounted for.

- We analyze and model the time-delay variations of indoor channels statistics based on measurements. The combination of extracted first- and second-order statistics enables to implement a channel impulse response (CIR) generator.

- To model the sudden changes of fading statistics, we use a three-step approach: (i) for reflecting the sudden changes of the statistics, we use a hidden Markov model [79] parameterized from measurements, (ii) the impacts of the line-of-sight (LOS) term and the Rayleigh component are modeled according to a Extreme Value distribution, fitting the measurements, (iii) fading realizations are generated [78].

- A model for large scale variations of the CIR is proposed.

The chapter is organized as follows: Section 5.1 presents the measurement setup, including the scenario, sounding equipment and antennas. It also outlines the data post- processing approach and the channel representation. Section 5.2 describes analyzed experimental results as well as the modeling of time-variant components. The global model is validated in Section 5.3.2. Finally, conclusions are drawn in Section 5.4.

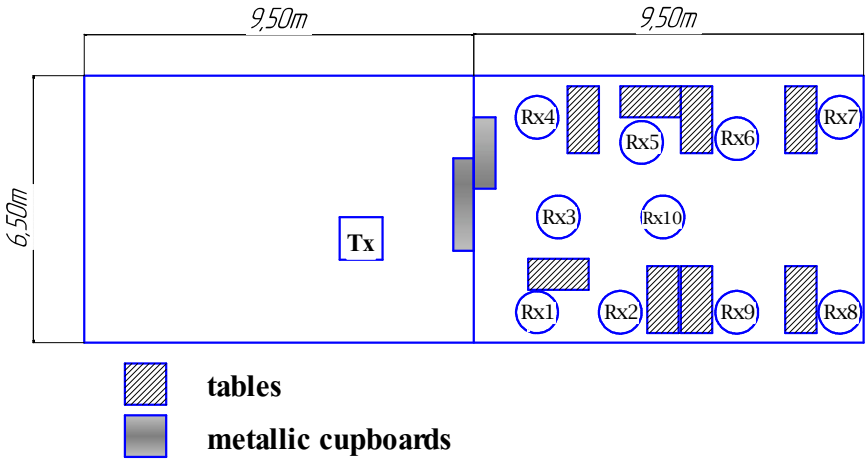

Figure 5.1: Pictures of the rooms and the floor-plan

Table 5.1: Distance between the nodes

Node	Rx1	Rx2	Rx3	Rx4	Rx5
Tx1	4.9 m	6.5 m	4.6 m	5.6 m	7.4 m
Node	Rx6	Rx7	Rx8	Rx9	Rx10
Tx1	9.7 m	12 m	12.1 m	9.2 m	7.6 m

Table 5.2: Measurement Parameters (After Post-Processing)

Parameter	Value
Center frequency	3.8 GHz
Transmit power	23 dBm
Measurement bandwidth	200 MHz
Recorded delay chips C	2048
Recorded time samples N_s	6000
Measurement duration	60 s
Code length	20.47 μs

5.1 Measurements and Methodology

5.1.1 Environment

Results shown in this chapter are based on channel measurements carried out at the Université catholique de Louvain (UCL), Louvain-la-Neuve, Belgium, in Fall 2014. The investigated environment was located on the second floor of an office building, and consisted of two adjacent typical office rooms separated by a brick wall, as illustrated in Figures 5.1. Circles indicate mobile receivers Rx1 to Rx10 (moving in random directions over a small area within a square of 1 m^2 at walking speed, $v \approx 1$ m/s), whereas the square indicates the static transmitter (Tx). The separations between all nodes are listed in the Table 5.1.

5.1.2 Equipment

The measurements were carried out with UCL/ULB Elektrobit PROPSound™ Channel Sounder (CS) at a carrier frequency of 3.8 GHz. The nodes were connected with the channel sounder using long low-loss RF cables of equal length. These cables had excellent RF stability, even when they were slightly bent or moved during the measurements. At the nodes, custom-made dipole antennas with a gain of 1.75 dB and an omnidirectional radiation pattern were used (see Section 2.3). The channel sounder used long pseudo-noise (PN) sequences to estimate the impulse response of the radio channels between Tx and Rx nodes. The measurement parameters are summarized in Table 5.2. The recorded channel impulse response is denoted by $h(t, \tau, j)$, where t denotes the time index, τ denotes the delay index, and j denotes the link index (a link joining one transmit node to one receive node).

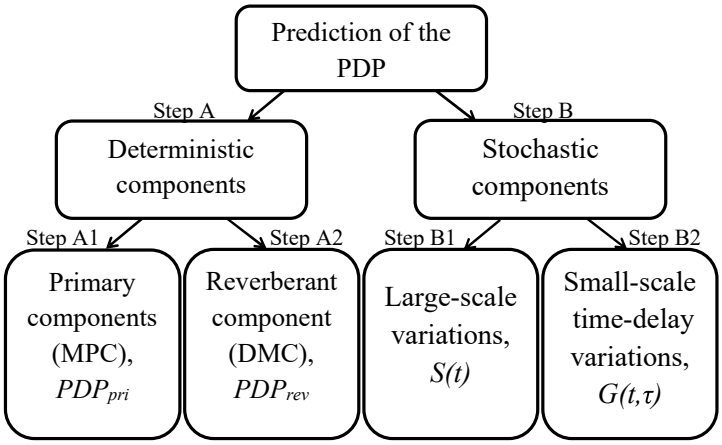

Figure 5.2: Schematic of the methodology.

5.1.3 Channel Representation

The methodology proposed here is based on *i)* the prediction of the deterministic PDP (in static scenario), and *ii)* the prediction of (stochastic) LS fading and SS fading statistics. The small-scale fading statistics [3, 43] describe the variations - around the average power level - caused by random motions of the transceivers. The general methodology to reconstruct the PDP is illustrated in Figure 5.2.

Indoor channel measurements have shown that the PDP averaged over time consists of two parts: a primary part and a reverberant part [67, 68, 69]. The complete PDP is the superposition of the primary and reverberant components, the LS fading which affects only the primary component, and the small-scale fading

$$PDP(t,\tau) = (S(t) \cdot PDP_{pri}(\tau) + PDP_{rev}(\tau)) \cdot |G(t,\tau)|^2, \qquad (5.1)$$

where PDP_{pri}, PDP_{rev}, S and G are the (deterministic) primary component, (deterministic) reverberant component, temporal large- and small-scale variations, respectively. All components in (5.1) are expressed in a natural scale.

5.2 Time-Delay Variant Channel Components

The modeling approach for the stochastic channel components (step B of Figure 5.2) is explained in this section. As mentioned above, the stochastic channel components can be expressed as the product (when expressed in natural scale) of the temporal large-scale variations $S(t)$ and time-delay variant small-scale variations $G(t,\tau)$:

- Temporal large-scale variations $S(t)$ are introduced by mobility of scatterers and slow changes of the environment. Only primary components (see Figure 1.10) are affected.
- Time-delay small-scale variations $G(t,\tau)$ (in natural scale) caused by multipath interference resulting from the small-scale motions of the stations and/or the environment. Both primary and reverberant components are influenced by these variations

$$G(t,\tau,j) = \frac{h(t,\tau,j)}{\sqrt{PDP_{av}(\tau,j)\cdot S(t,j)}}, \tag{5.2}$$

where $PDP_{av}(\tau,j)$ is an averaged over time PDP for channel j, the small-scale fading amplitude is then simply defined as $g = |G|$. Analogous to the terminology used for narrowband channels, let us denote $S(t)$ and $G(t,\tau)$ as large- and small-scale fading, respectively.

Figures 5.3 a, b, c show measured changes of the received power, measured PDP that is constant over time for a given link and time evolution of large- and small-scale variations for a fixed delay, respectively.

5.2.1 Large-Scale Fading Characterization and Modeling

To extract non-deterministic components of the channel, first, the measured PDP_{av} has to be subtracted from the considered channel $P(t,\tau,j) = 10\log|h(t,\tau,j)|^2|_{dB} - PDP_{av}(\tau,j)|_{dB}$. Next, to estimate LS fading, we average out the small-scale fading by using a moving window spanning $T_{av} = 1.5$ s (see Figure 5.3 c), so that the time-variant average power can be written as

$$S(t,j) = \frac{1}{T_{av}\cdot\tau_l}\sum_{t'=t-T_{av}/2}^{t+T_{av}/2}\sum_{\tau'=0}^{\tau_l}|P(t',\tau',j)|. \tag{5.3}$$

The choice of T_{av} is such that the small-scale fading is averaged out, while still following the slow variations induced by the motion of the nodes and/or people. Different sizes of the window have been checked and the window span has been chosen to be equivalent to 20 wavelengths. This size of the sliding window was also used in [92, 82].

When the static PDP_{av} is removed and time-delay small-scale fading is averaged out, the remaining variations are due to large-scale fading, as detailed earlier. We observe in Figure 5.4 a that the LS fading (in dB) is described by a t-location scale distribution with zero-mean ($\mu = 0$) by definition, $\nu = 8$ degrees of freedom and a scale parameter $\sigma_{\tilde{s}} = 2.4$. This distribution has been used previously to describe large-scale fading in Chapters 3,4, so that large-scale fading is assumed to have a Gaussian distribution with an unknown variance distributed as inverse gamma, and then the variance is marginalized out.

The LS fading autocorrelation function (ACF) over time is modeled as a decreasing exponential, whose decay time $\tau_{\tilde{s}} = 8.4$ $[s]$ (see Figure 5.4 b). Hence, we use an autoregressive process to generate autocorrelated LS fading values:

$$S(t)|_{dB} = e^{-\triangle t/\tau_S}S(t-\triangle t) + \sqrt{1-e^{-2\triangle t/\tau_S}}x_S(t), \tag{5.4}$$

where x_S is a t-location scale distributed variable generated independently for each time instant t and $\triangle\ t$ equals the state duration.

No correlation between large-scale fading levels and the small-scale fading states has been found, so that we can combine independently simulated large- and small-scale fading realizations.

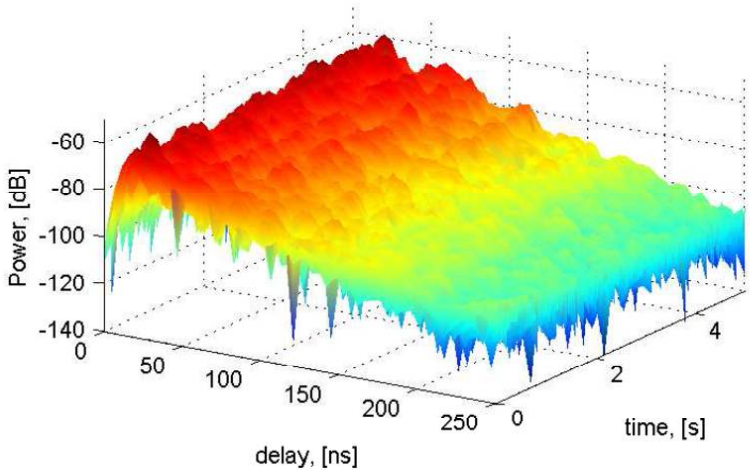

(a) Time evolution of relative power

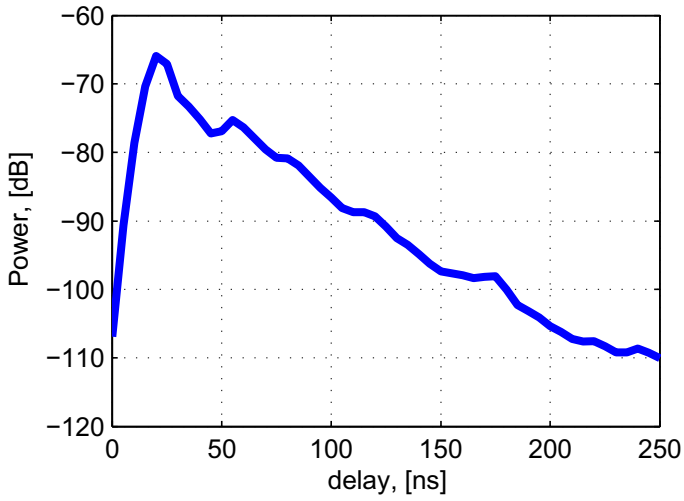

(b) Power delay profile

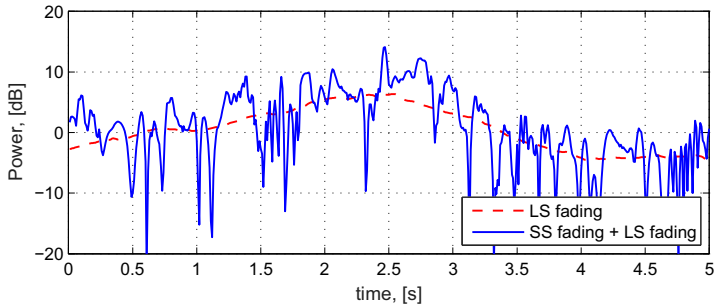

(c) Time-variant components of the channel (Primary component, fixed delay)

Figure 5.3: Channel components

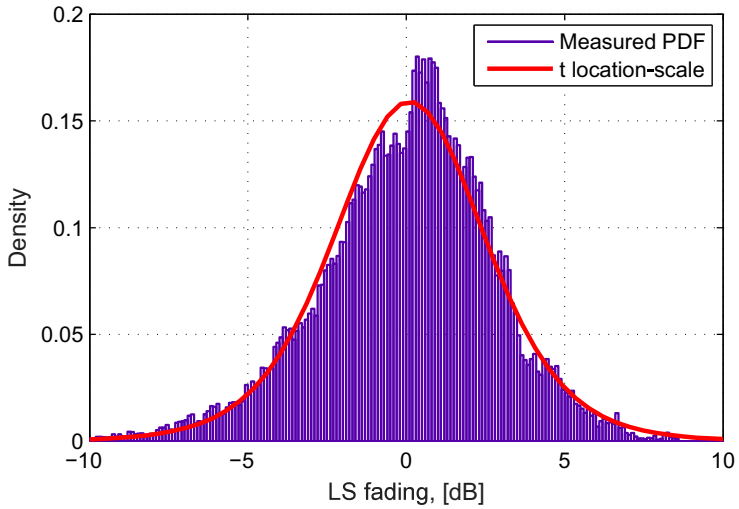

(a) Fit of the normal distribution to measured LS fading

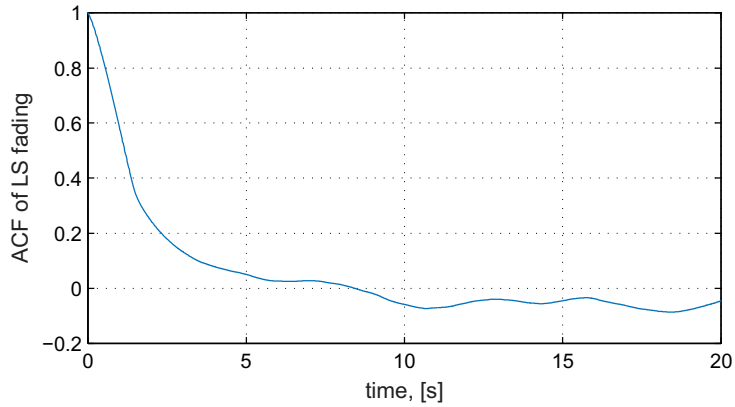

(b) Temporal autocorrelation of LS fading

Figure 5.4: Large-Scale fading statistics

Table 5.3: Probabilities of the subsets and transition probabilities

Subset	Probability	Transitions	
		Rician	Rayleigh
Rician	0.65	0.84	0.16
Rayleigh	0.35	0.85	0.15

5.2.2 Small-Scale Fading Modeling

As it was shown in [31] and in Chapter 1, we define the stationarity period as 1.5 s. To extract first-order statistics of time-delay fading, the whole delay range is first partitioned into bins of τ_b = 10 ns (2 delay chips) each. This leads to a total number of B = 1024 bins per time instant and link. Next, 40×1024 blocks of 150×2 realizations (corresponding to $T_{av} = 1.5$ s or 20 wavelength) can be used to extract statistics.

It turns out that complex channel impulse responses fade out to the noise level for delays larger than 250 ns (50 delay chips) so that we can use only first 40×25 blocks for each measured link j. Note that we can normalize fading so that $\mathbb{E}\{g^2\} = 1$, the expectation being taken over time or delay.

First-Order Fading Statistics

As shown in Chapter 3, we can expect small-scale fading within a bin to be Rician or Rayleigh distributed for single mobile scenarios. The time-delay varying K-factor can be estimated from experimental time-delay fading realizations $g(t, \tau, j)$ by fitting the Rice probability density function. 40×25 realization blocks have been used. Extracted probabilities of the subsets (Rician and Rayleigh) and transition probabilities are shown in Table 5.3.

Temporal transitions between different fading states can be modeled by means of a hidden Markov model (HMM) [79]. Usually, the system being modeled by a HMM is assumed to be a Markov process with unobserved (*hidden*) states. Since only two distributions of small-scale fading are observed, we model the transitions between the subsets using a simple two-state HMM: (i) Rican fading and (ii) Rayleigh fading. Consequently, the HMM is parameterized from the measurements.

To simplify the usage of first- and second- order statistics derived in [43], let us denote:

$$\omega_0 = \sqrt{\frac{K}{1+K}}, \tag{5.5}$$

$$\omega_1 = \sqrt{1 - \frac{K}{1+K}}, \tag{5.6}$$

where K is the estimated K-factor (in dB); ω_0 and ω_1 describe the impact of the LOS term and Rayleigh component respectively.

The distribution of the K-factor for the Rician subset can be modeled by Extreme Value distribution, when the K-factor expressed in decibels (see Figure 5.5). The

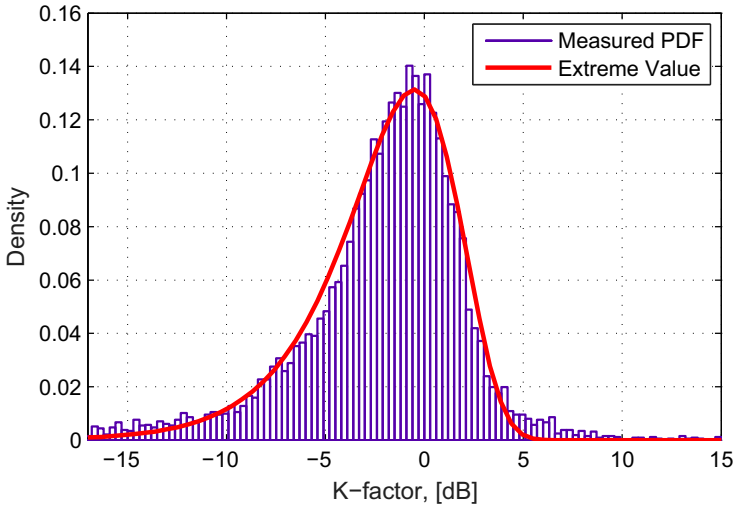

Figure 5.5: Distribution of the Rician K-factor

Table 5.4: Measured Parameters

Parameter	Value
ω_{DB}	$\frac{2\omega_1}{3}$
$\omega_{SBT} = \omega_{SBR}$	$\frac{\omega_1}{6}$
R	3 m
f_m	13.8 MHz

temporal autocorrelations of the measured K-factor is a decreasing exponential function . Hence, the model presented in Chapters 3 and 4 (i.e. an autoregressive process) can be used to generate autocorrelated values of the K-factor over time samples $(t = [1, \cdots, T])$:

$$K(t)|_{dB} = e^{-\triangle t/\tau_K} K(t - \triangle\, t)|_{dB} + \sqrt{1 - e^{-2\triangle t/\tau_K}}\, x_K(t), \tag{5.7}$$

where x_K is a time series of length T, whose values are drawn independently from the appropriate distribution and $\triangle\, t$ equals the state duration. The parameter $\tau_K = 2.5[s]$ is extracted from measurements.

It turns out that the first order statistics are not correlated over delay bins, consequently, time-variant fading within a bin can be modeled independently from neighboring bins.

Second-Order Fading Statistics

The room to room environment can be approximated by a double-ring representation [59] as shown in Chapter 3. The correlation functions of the fading can be expressed

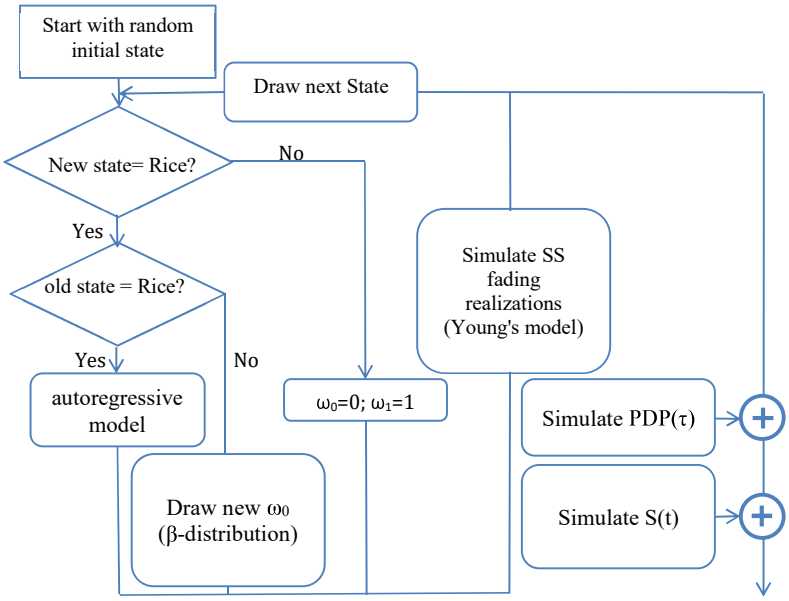

Figure 5.6: Flow diagram of the complete model (Steps A+B)

as

$$\begin{aligned} &R_{G_iG_i}(\tau) = R_{G_qG_q}(\tau) = R_{GG}(\tau) = \mathbb{E}[G_q(t)G_q(t+\tau)] \\ &= \omega_0^2 \cos\left(2\pi\tau\left(f_m \cos\Theta\right)\right) \\ &+ \left(\omega_{DB}^2 + \omega_{SBR}^2\right) \cdot J_0\left(2\pi f_m \tau\right) + \omega_{SBT}^2 \cdot J_0\left(\frac{R^2}{D^2}\pi f_m \tau\right), \end{aligned} \tag{5.8}$$

$$R_{G_iG_q}(\tau) = -R_{G_qG_i}(\tau) = 0, \tag{5.9}$$

where f_m, Θ, R and D denote the Doppler frequency caused by motion of the mobile node, the angle of the motion, radius of the ring which is formed by scatterers located around the static node and the distance between Tx and Rx, respectively.

Small-scale fading realizations used to extract the parameters ω_0 and ω_1 were analyzed to estimate the parameters of second order statistics. First, the Doppler Spectrum was calculated. Next, the Doppler frequency was estimated so that we could calculate the radii using measured Doppler spectrum and the theoretical one. Finally, estimated parameters (R, f_m and the components weights) were averaged over all channels and samples and bins. The summary of the analysis is listed in Table 5.4.

5.2.3 Time-Series Modeling

Summarizing, we propose to model channels with time-variant statistics and a static PDP as shown in Figure 5.6. We start with a random initial state of the HMM. Next, using the corresponding distribution, we draw the weights (ω_0, ω_1). Using a weighted

combination of correlated small-scale fading realizations generated by the model[1] described in [78], we obtain a pre-defined number of correlated complex fading realizations $G(t)$. Next, the $PDP(\tau)$ (modeled as it was shown in Section1.6) corresponding to the considered delay and the large-scale fading are added to the small-scale fading realizations. Next, the state of the HMM is updated. If the state is unchanged, we use the autoregressive model described by (5.7) to generate a new value of ω_0 for the Rician subset or we keep the constant values of the parameters for the Rayleigh subset. If the state is modified, depending on the subset, we generate the weights ω_0 and ω_1 using the corresponding distribution or we set fixed values (for Rayleigh). For the next delay bin the algorithm should be repeated. Note that the duration of one state equals 1.5 s.

5.3 Simulation Results and Validation

5.3.1 Reconstructed Power Delay Profiles

The deterministic modeled PDP do not vary with time. For a given position, the variation in the measured PDP is due to the small-scale fading. The deterministic models are presented in Figures 5.7 a, b. Measured time-variant PDPs are shown in Figures 5.7 c, d. The complete model is the aggregate of the small-scale fading and LS fading levels and the deterministic model for the considered nodes (Rx1,7). Example of the total PDP models in the dynamic scenario are shown in Figures 5.7 e, f.

Given the room dimensions in Figure 5.1, and by applying (1.74), we obtain a reverberation time of about 20.80 ns for the in-room scenario. In this study, Tx and Rx are located in adjacent rooms (see Figure 5.1). Therefore, we apply (1.76) and obtain a theoretical reverberation time of about 24.80 ns for the adjacent room scenario.

Table 5.5: Experimental values of the reverberation time for the different nodes

Node	Rx1	Rx2	Rx3	Rx4	Rx5
$\tau_{r,a}$ (ns)	21.85	21.45	25.10	28.20	22.80
Node	Rx6	Rx7	Rx8	Rx9	Rx10
$\tau_{r,a}$ (ns)	19.90	20.55	20.75	20.55	22.10

Experimental values of the reverberation time at different nodes are shown in Table 5.5. On average, an experimental reverberation time of 22.30 ns and a standard deviation of 2.50 ns are obtained. The relative difference between the experimental and theoretical reverberation time is about 11.20%, indicating good agreement between the predicted and measured reverberation time [75]. The formula overestimates the reverberation time value because of the presence of furniture in the room. Only walls, floor and ceiling are indeed considered; hence, this will lower the experimental reverberation time value compared to the predicted one.

[1]Filter coefficients used in the model are specified by appropriate first- and second-order statistics derived in Chapter 3.

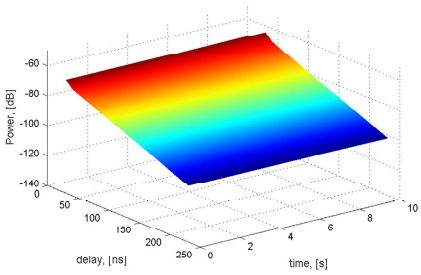

(a) Deterministic PDP, node Rx1

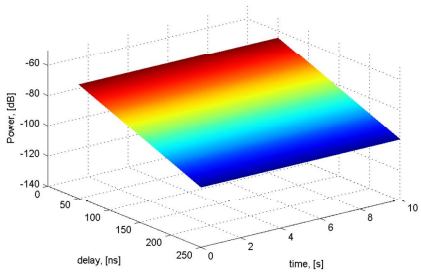

(b) Deterministic PDP, node Rx7

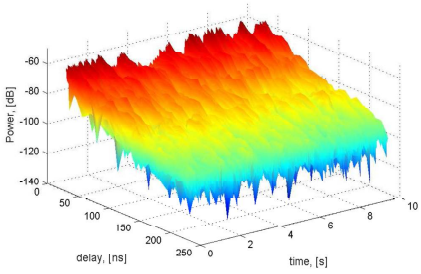

(c) Measured time-variant PDP, node Rx1

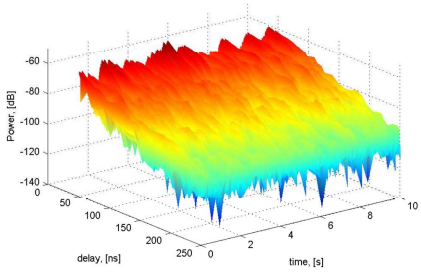

(d) Measured time-variant PDP, node Rx7

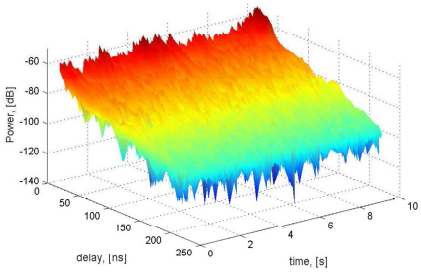

(e) Simulated time-variant PDP, node Rx1

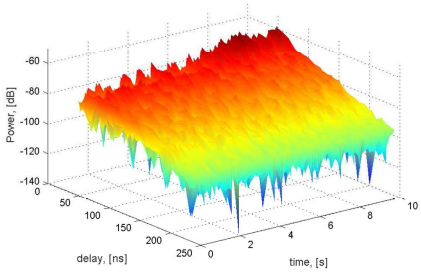

(f) Simulated time-variant PDP, node Rx7

Figure 5.7: Deterministic, small-scale fading level, and the total reconstructed PDP.

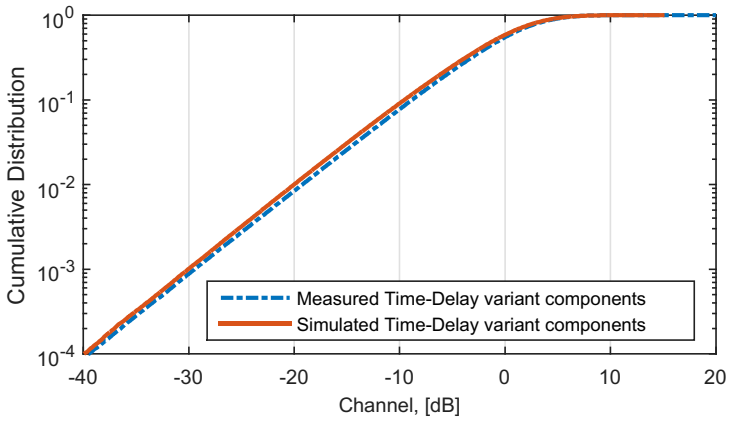

Figure 5.8: CDFs of measured and simulated stochastic components (combined large- and small-scale fading)

5.3.2 Validation

The validation is an important step in any model development. To validate the model, we use a two-step approach: i) we check if the model reproduces correctly the measured statistics of the time-delay variant components, ii) we show that parameters derived from the model (but not directly used to parameterize it) agree well with the equivalent measured parameters of the channel.

Statistics of Time-Delay Variant Components

Figure 5.8 compares the statistics of measured channels and generated channels using the model described in Section 5.2. To verify the model for different distances, we simulated links between nodes separated by the same distances as we had for measured channels. Next, we compared the cumulative distribution function (CDF) of the generated combination of large- and small-scale fading with the CDF of the same components of the measured set of channels. It is obvious that statistics of simulated channels are in good agreement with the simulated ones.

Instantaneous Delay Spread

We define here the *instantaneous* root-mean-square (rms) delay spread as

$$\tau_{rms}(t) = \sqrt{\frac{\int_0^\infty (\tau - \bar{\tau}(t))^2 \cdot |h(t,\tau)|^2 d\tau}{\int_0^\infty |h(t,\tau)|^2 d\tau}}, \tag{5.10}$$

where $\bar{\tau}(t)$ is the mean delay of the instantaneous channel $h(t,\tau)$. The objective of defining the instantaneous rms delay spread is to produce cumulative distribution functions (CDF) of the rms delay values obtained in the dynamic scenario (time domain) for both the measured and predicted PDPs. The comparison of the mean rms values

from the measurements and model is listed in Table 5.6. Parameter $\Delta\tau_{rms}$ is the difference between the mean predicted and measured rms delay spread values. Relative errors $\Delta\tau_{rms} = 100 \cdot (\tau_{rms}^{exp} - \tau_{rms}^{meas}) \,/\, \min(\tau_{rms}^{exp}, \tau_{rms}^{meas})$ are also listed in the table. Averaged value of $\Delta\tau_{rms}$ for all the nodes equals 0.24 ns (or 1.04 %). This asymptotic value of the error $\Delta\tau_{rms}^{avg}$ is achieved after 20 simulation trials.

Table 5.6: Experimental and predicted average values of the rms delay spread for the different nodes

Node	Rx1	Rx2	Rx3	Rx4	Rx5
Distance (m)	4.9	6.5	4.6	5.6	7.4
$\tau_{rms}^{exp.}$ (ns)	20.67	23.11	19.82	23.12	22.63
$\tau_{rms}^{mod.}$ (ns)	20.43	22.7	20.01	22.57	22.61
$\Delta\tau_{rms}$ (ns)	0.24	0.41	0.19	0.55	0.02
$\Delta\tau_{rms}$ (%)	1.17	1.81	0.96	2.4	0.09
Node	Rx6	Rx7	Rx8	Rx9	Rx10
Distance (m)	9.7	12	12.1	9.2	7.6
$\tau_{rms}^{exp.}$ (ns)	24.12	24.14	24.07	23.51	21.63
$\tau_{rms}^{mod.}$ (ns)	24	24.04	24.01	23.87	22
$\Delta\tau_{rms}$ (ns)	0.12	0.11	0.06	0.36	0.37
$\Delta\tau_{rms}$ (%)	0.5	0.46	0.25	1.56	1.71

The CDFs of rms delay spread values of two nodes are shown in Figures 5.9 a and b. Two cases are demonstrated: Figures 5.9 a shows CDFs with the largest error $\Delta\tau_{rms}$, whereas Figure 5.9 b shows CDFs with $\Delta\tau_{rms} = 0.24$ ns, which equals the asymptotic value of the error $\Delta\tau_{rms}^{avg}$.

On the one hand, we observe that the rms delay spread value approaches the theoretical reverberation time for the room-to-room scenario, i.e., $\tau = 24.80$ ns, for increasing Tx-Rx distances (e.g. Rx7,8). This shows that the influence of the primary components decreases when the Tx-Rx distance increases and the diffuse fields become prominent. Therefore, the shape of the PDP approaches an exponential decay ($\tau_0 \longrightarrow \tau_l$). For node Rx4, we observe the largest error (see Table 5.6). The possible explanation is that this channel is highly affected by two large metallic cupboards (Figure 5.1).

On the other hand, when we compare the cumulative distribution function of the experimental and modeled rms delay spread, we can conclude that the propose methodology estimates well the PDP in room-to-room scenarios. Measured and simulated CDFs do not agree completely but a reasonably good match in terms of sample mean and sample variance is achieved for all the nodes (except node 4, see Figure 5.9 a) with the asymptotic error $\Delta\tau_{rms}^{avg} = 0.24$ ns. As mentioned above, this large error for node 4 is due to the proximity of this node to large metallic cupboards (see Figure 5.1).

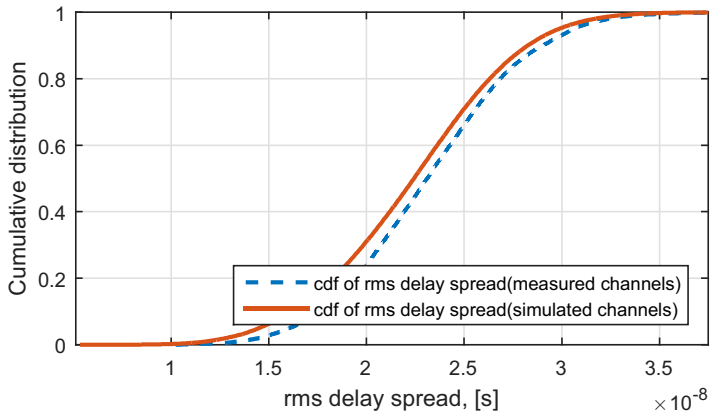

(a) CDFs of the rms delay spread, node Rx4 (distance = 5.6 m)

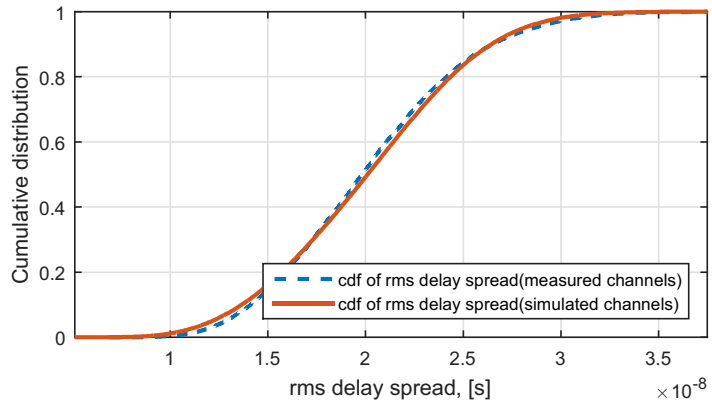

(b) CDFs of the rms delay spread, node Rx1 (distance = 4.9 m)

Figure 5.9: Cumulative distribution function of τ_{rms}: measurement versus model

5.4 Summary

We have designed a methodology for the prediction of power delay profiles in room-to-room dynamic scenarios. The success of the method is guaranteed by the predominance of the diffuse scattered fields in the considered environment. Basically, the deterministic part of the method is based on the reverberation time of the environment, which fully describes the diffuse fields and predict the average power level. Moreover, we have proposed models for time-delay large- and small-scale fading. A Hidden Markov model has been used to describe the evolution of the small scale fading statistics and then time-delay fading realizations have been generated using the Young's model [78].

This model enables to describe of the evolution (or change) of the power delay profile in the time domain. The method has been validated against the measurements and good agreement is obtained. Note that the model can be easily extended to double

mobility cases by using the five-state HMM described in Chapter 3. Moreover, it has been showed that the distribution of Rician K-factor can be modeled by Extreme Value Distribution as it was done in previous Chapters and in [43].

Chapter 6

Conclusions

Research Contribution

Despite the fact that distributed, peer-to-peer and MIMO indoor systems have been designed and used for various applications for some years now, there is still a room for improvements. Channel modeling is one of the aspects where researchers and engineers face many challenges.

To enable the successful design of communication systems, such an important issue as non-stationarity must be taken into account. The assumption of stationarity is still used in the majority of the algorithms at the Tx and Rx. One could say that an indoor environment cannot change as fast as in the case of car-to-car communication, for example. However, published papers [15, 38, 16] report that statistics of indoor channels are varying over time. Consequently, the classical approach is no longer valid. Hence, this opens the door to new radio propagation channel models, that would describe this specific feature. New models can infuse new life into already existing algorithms which could be improved by taking into account the non-stationary description of radio propagation channel statistics.

That was the reason why our research was focused on the modeling of non-stationary SISO and MIMO multipath fading narrow- and wideband channels. Three measurement campaigns were conducted in 2009, 2014 and 2016. Different scenarios were extensively investigated for indoor environment.

It has been shown that measured indoor small-scale fading channels cannot be considered stationary for the whole measurement duration. However, periods over which the channel is stationary can be defined based on the correlation matrix distance or power delay profiles correlation analysis. The problem of choosing an appropriate window size is addressed in this thesis. When the stationarity is defined using CMD as a metric, it turns out that the time window used for the receive correlation matrix estimation equals $5 \cdot T$, where T is the minimal coherence time. Next, CMDs are calculated and stationarity periods can be estimated. When the correlation of time-variant PDPs is the used metric, it is enough to choose the window long enough to average fading out. In the thesis, the period duration varies between $0.8 - 1.5$ s for different investigated cases depending on the environment.

Let us first concentrate on channel analysis within a stationarity period. It turns

out that small-scale fading rather follows a weighted combination of different known distributions than a single one. This mixed type of fading can be described by a Second Order Scattering Fading (SOSF) distribution which reflects any combination of Rician, Rayleigh, and double-Rayleigh fading.

New double-ring geometry-based reference models including so-called single- and double-bounced components with independent and correlated scattering have been proposed for single- and multi-antenna channels as well as a new sum-of-sinusoids simulation model for MIMO second order scattering fading channels. The models available in literature consider only single- and double-bounced correlated scattering, however it is shown in this thesis that inclusion of the independent scattering significantly changes first and second order statistics of the channel. It turns out that Double Rayleigh fading (observed in 83-93 % of measured fading ensembles) is caused by this scattering mechanism. Summarizing, theoretical analysis of small-scale fading statistics reveals that:

1. In single antenna double-mobile scenarios, the channel is characterized by the SOSF distribution, with statistics ranging from double-Rayleigh to Rician.

2. In single antenna single-mobile scenarios, temporal small-scale fading is Rayleigh or Rician distributed.

3. Frequency small-scale fading follows a SOSF distribution.

4. Multi-antenna channels are described by a SOSF distribution.

From the reference models, correlation functions of both SISO and MIMO fading channels are derived for an isotropic and non-isotropic scattering environment.

It is found out that experimental angles of arrival are rather described by a bimodal Tikhonov-von Mises distribution than a simple one used in [95, 96]. It is shown that two subscenarios must be distinguished: when the communication nodes are located on the same and different sides of the corridor. When the corridor is a part of the propagation channel, the major part of waves arrives over a smaller angular range. Usually, the maximum direction of arriving waves corresponds to a corner of the room where the Rx is located. In the case when the nodes are located in the rooms on the same side of the corridor, AoAs are dispersed over a larger range, mostly concentrated in the direction of the transmitting node. Moreover, a noticeable impact of the backscattering is observed.

The next important question is how to model the temporal changes of statistics from one stationarity period to another. An approach of modeling time-variant channel statistics based on hidden Markov Models has been proposed. It can be parameterized from measurements: empirical estimation and transition matrices were extracted for the three investigated environments. We observed that predominant fading mechanism can be described by a mixture of Rayleigh and Double Rayleigh distributions. Distributions of the parameter α (corresponding to the impact of Double Rayleigh fading) for the Rayleigh-double Rayleigh and Δ (joint impact of the LOS term and Double Rayleigh fading) for the double-Rayleigh-LOS subsets can be well approximated by the Beta distribution; the K-Factor (derived from parameter β of SOSF distribution) of Rician fading is Extreme Value distributed. This approach with some modification (usually inclusion or removal observed/absent types of fading) has been used through

the thesis for SISO and MIMO narrowband channels and in a single-antenna wideband channel modeling. This shows that the proposed approach can be used as a framework for propagation modeling in various indoor environments.

It is necessary to mention that the scale of node's motion also has an impact on the statistics: limited motions ($\approx 1m^2$) result in smaller impact of independent double bouncing and, consequently, of Double Rayleigh fading.

The time-variant behavior of the angular distribution has been studied as well. Distributions of bimodal Tikhonov-von Mises' parameters can be approximated by Gamma (κ_1, κ_2) and Beta (w) distributions. Since, the autocorrelation functions of the parameters is decreasing exponentially, temporal variations of parameters κ_1, κ_2 and w can be modeled by autoregressive functions.

A methodology of time-variant power delay profiles has been designed in the room-to-room dynamic scenario. Basically, the deterministic part of the method is based on the reverberation time of the environment, which fully describes the diffuse fields and predict the average power level. Moreover, the SISO model described above has been extended for modeling of large- and small-scale fading of a fixed tap. This model enables to describe the evolution (or change) of the power delay profile in the time domain. Note that the wideband model can be easily extended to double mobility cases by using the five-state HMM described in Chapter 3. Moreover, it has been shown that the distribution of Rician K-factor can be modeled by Extreme Value Distribution as it was done in Chapters 3-5 and in [43].

In the thesis, the study of large-scale fading was not the main point of interest. However some interesting results have been achieved: the high relevance of the concept of separating large-scale fading into two parts (dynamic and mean) proposed in [3] has been confirmed. Normal distribution with zero-mean and the variance extracted from measurements can be used for mean large-scale fading modeling and dynamic large-scale fading follows a t-location scale distribution. In other words, the dynamic LS fading is assumed to have a Gaussian distribution with an unknown variance distributed as inverse gamma, and then the variance is marginalized out. The t-location scale distribution has longer tails which represents the measured data better. Note, that different mechanisms typical for investigated scenarios lead to variations of the value of the scale parameter $\sigma_{\tilde{s}}$ depending on the type of mobility and the motion scale. We can make a conclusion that the more scatterers and objects interacting with radiated waves are involved in the propagation, the higher $\sigma_{\tilde{S}}$ is: it is obvious that extended motion of both nodes will result in more significant variations of the LS fading levels than in the case of limited motion of the Tx (Rx) while the Rx (Tx) is static.

The presented models have been validated against the measurements and a good agreement is obtained.

Perspective and Future Work

Considering growing demand of multimedia services and the tendency that more and more devices need to provide an access to these services in indoor environments, several probabilities for future researches could be suggested, for example

- There is always a room to improve a channel model. For example, our geometry-based models assume that the scattering objects are stationary, which is an unre-

alistic assumption in certain situations. It could be useful to extend the presented models to a 3D case.

- Measuring indoor channels in many different locations/buildings could provide us more statistics and, consequently, make the model more universal.
- An improved channel model is not a goal in itself, that is why improvement in the system performance that can be expected when taking into account the non-stationary behavior of radio propagation channels has to be determined. Already existing algorithms have to be optimized in order to take advantage of this non-stationary channel behavior. For instance, the adaptive beamforming applications be an answer, due to the ability to transmit information in a way maximizing the experienced radio propagation channel's stationarity.
- Existing channel models are mostly not fully compatible with distributed MIMO, MU-MIMO and cooperative communication networks as originally they have been developed for single link systems. Hence, the next research direction could be to extend the concept of non-stationarity to next generation wireless communication multi-user systems, including relaying applications, cognitive radio, etc. The definition of the non-stationarity in the context of multi-user systems has to be established: the reference, metrics, level (the link level or more from the system point of view) have to be defined.

List of Publications

Journals:

1. E. Vinogradov, W. Joseph and C. Oestges, "Measurement-Based Modeling of Time-Variant Fading Statistics in Indoor Peer-to-Peer Scenarios," *IEEE Transactions on Antennas and Propagation*, vol. 63, no. 5, pp. 2252-2263, May 2015.
2. E. Vinogradov, A. Bamba, W. Joseph and C. Oestges, "Physical-Statistical Modeling of Dynamic Indoor Power Delay Profiles," *under review in IEEE Transactions on Wireless Communications*

Conference proceedings:

1. E. Vinogradov, W. Joseph and C. Oestges, "Modeling and simulation of fast fading channels in indoor peer-to-peer scenarios," *The 8th European Conference on Antennas and Propagation (EuCAP 2014)*, The Hague, 2014, pp. 433-434.
2. O. Font-Bach, N. Bartzoudis, D. Lopez, E. Vinogradov, M. Payar, C. Oestges, T. A. Myrvoll and V. Ringset, "Experimental performance evaluation of a 5G spectrum sharing scenario based on field-measured channels," *IEEE 26th Annual International Symposium on Personal, Indoor, and Mobile Radio Communications (PIMRC)*, Hong Kong, 2015, pp. 856-861.
3. E. Vinogradov, W. Joseph and C. Oestges, "MIMO indoor propagation: A geometry-based model including time-variant fading statistics," *The 10th European Conference on Antennas and Propagation (EuCAP 2016)* , Davos, 2016, pp. 1-4.

COST Actions:

1. E. Vinogradov and C. Oestges, "Modeling time-variant fast fading statistics in indoor peer-to-peer scenarios," *COST IC1004 TD(13)08019,* Ghent Belgium, September 2013
2. E. Vinogradov, A. Bamba, W. Joseph and C. Oestges, "Measurement-Based Modeling of Time-Variant Power Delay Profile," *COST IC1004 TD(15)13022,* Valencia Spain, May 2015

3. E. Vinogradov, A. Bamba, W. Joseph and C. Oestges, "Physical-Statistical Modeling of Dynamic Indoor Power Delay Profiles," *COST Action 15104 (IRACON) TD(16)01017,* Lille France, May-June 2016

Bibliography

[1] Cisco, "Cisco visual networking index: Global mobile data traffic forecast update, 20152020," Tech. Rep. [Online]. Available: http://www.cisco.com/c/en/us/solutions/collateral/service-provider/visual-networking-index-vni/mobile-white-paper-c11-520862.pdf

[2] Elektrobit, "Channel sounder user manual," Electrobit, Tech. Rep., 2006.

[3] C. Oestges, N. Czink, B. Bandemer, P. Castiglione, F. Kaltenberger, and A. Paulraj, "Experimental characterization and modeling of outdoor-to-indoor and indoor-to-indoor distributed channels," *IEEE Transactions on Vehicular Technology*, vol. 59, no. 5, pp. 2253–2265, June 2010.

[4] M. Le Treust and S. Lasaulce, "A repeated game formulation of energy-efficient decentralized power control," *IEEE Transactions on Wireless Communications*, vol. 9, no. 9, pp. 2860–2869, September 2010.

[5] M. Lott, "On the performance of an advanced 3D ray tracing method," in *In Proc. of European Wireless and ITG Mobile Communication*, 1999.

[6] M. F. Iskander and Z. Yun, "Propagation prediction models for wireless communication systems," *IEEE Transactions on Microwave Theory and Techniques*, vol. 50, no. 3, pp. 662–673, March 2002.

[7] Z. Ji, B.-H. Li, H.-X. Wang, H.-Y. Chen, and T. K. Sarkar, "Efficient ray-tracing methods for propagation prediction for indoor wireless communications," *IEEE Antennas and Propagation Magazine*, vol. 43, no. 2, pp. 41–49, April 2001.

[8] F. Mani, F. Quitin, and C. Oestges, "Directional spreads of dense multipath components in indoor environments: Experimental validation of a ray-tracing approach," *IEEE Transactions on Antennas and Propagation*, vol. 60, no. 7, pp. 3389–3396, July 2012.

[9] T. Rautiainen, R. Hoppe, and G. Wolfle, "Measurements and 3D Ray Tracing Propagation Predictions of Channel Characteristics in Indoor Environments," in *IEEE 18th International Symposium on Personal, Indoor and Mobile Radio Communications (PIMRC)*, September 2007, pp. 1–5.

[10] C. A. 2100, *"Pervasive Mobile and Ambient Wireless Communications"*, R. Verdone and A. Zanella, Eds. Springer, 2012.

[11] J. Medbo and J.-E. Berg, "Simple and accurate path loss modeling at 5 GHz in indoor environments with corridors," in *IEEE 52nd Vehicular Technology Conference (VTC Fall)*, vol. 1, 2000, pp. 30–36 vol.1.

[12] J. Kivinen, X. Zhao, and P. Vainikainen, "Empirical characterization of wideband indoor radio channel at 5.3 GHz," *IEEE Transactions on Antennas and Propagation*, vol. 49, no. 8, pp. 1192–1203, August 2001.

[13] K. Tan and S. Denno, "Empirical characterisation of indoor broadband propagation channel," in *IEEE 14th International Symposium on Personal, Indoor and Mobile Radio Communications (PIMRC)*, vol. 1, September 2003, pp. 950–954 Vol.1.

[14] D. Xu, J. Zhang, X. Gao, P. Zhang, and Y. Wu, "Indoor office propagation measurements and path loss models at 5.25 GHz," in *IEEE 66th Vehicular Technology Conference (VTC Fall)*, September 2007, pp. 844–848.

[15] J. Karedal, A. Johansson, F. Tufvesson, and A. Molisch, "A measurement-based fading model for wireless personal area networks," *IEEE Transactions on Wireless Communications*, vol. 7, no. 11, pp. 4575–4585, November 2008.

[16] M. Herdin, "Non-stationary indoor MIMO channels," Ph.D. dissertation, Technischen Universität Wien, 2004.

[17] C. Oestges, D. Vanhoenacker-Janvier, and B. Clerckx, "Channel characterization of indoor wireless personal area networks," *IEEE Transactions on Antennas and Propagation*, vol. 54, no. 11, pp. 3143–3150, November 2006.

[18] C. Oestges, P. Castiglione, and N. Czink, "Empirical modeling of nomadic peer-to-peer networks in office environment," in *IEEE 73rd Vehicular Technology Conference (VTC Spring)*, May 2011, pp. 1–5.

[19] I. Kovacs, P. C. F. Eggers, K. Olesen, and L. Petersen, "Investigations of outdoor-to-indoor mobile-to-mobile radio communication channels," *IEEE 56th Vehicular Technology Conference (VTC Fall)*, vol. 1, pp. 430–434 vol.1, 2002.

[20] I. Cuinas and M. Sanchez, "Measuring, modeling, and characterizing of indoor radio channel at 5.8 GHz," *IEEE Transactions on Vehicular Technology*, vol. 50, no. 2, pp. 526–535, March 2001.

[21] N. Czink, B. Bandemer, G. Vazquez-Vilar, L. Jalloul, C. Oestges, and A. Paulraj, "Spatial separation of multi-user MIMO channels," *IEEE 20th International Symposium on Personal, Indoor and Mobile Radio Communications (PIMRC)*, pp. 1059–1063, September 2009.

[22] J. Nielsen, V. Afanassiev, and J. Andersen, "A dynamic model of the indoor channel," *Wireless Personal Communications*, vol. 19, no. 2, pp. 91–120, 2001.

[23] B. Clerckx and C. Oestges, *MIMO Wireless Networks*. 2nd ed. Elsevier Academic Press.

[24] A. Molisch, *Wireless Communications*, ser. Wiley - IEEE. Wiley, 2011.

[25] P. Bello, "Characterization of randomly time-variant linear channels," *IEEE Transactions on Communications Systems*, vol. 11, no. 4, pp. 360–393, December 1963.

[26] F. Y. Luan, Y. Zhang, X. W. Hu, S. D. Zhou, L. M. Xiao, and X. B. Xu, "Measurement-based delay spread analysis of indoor distributed antenna systems," in *Proceedings of the 5th European Conference on Antennas and Propagation (EUCAP)*, April 2011, pp. 2556–2559.

[27] J. Li, B. Ai, R. He, K. Guan, Q. Wang, D. Fei, Z. Zhong, Z. Zhao, D. Miao, and H. Guan, "Measurement-based characterizations of indoor massive mimo channels at 2 GHz, 4 GHz, and 6 GHz frequency bands," in *IEEE 83rd Vehicular Technology Conference (VTC Spring)*, May 2016, pp. 1–5.

[28] O. H. Koymen, A. Partyka, S. Subramanian, and J. Li, "Indoor mm-wave channel measurements: Comparative study of 2.9 GHz and 29 GHz," in *IEEE Global Communications Conference (GLOBECOM)*, December 2015, pp. 1–6.

[29] Z. Jiang, J. Yu, R. Zhu, K. Yang, and W. Chen, "Experimental multipath delay spread and path loss analysis for the indoor environment at 5.9 GHz," in *2016 International Conference on Wireless Communications, Signal Processing and Networking (WiSPNET)*, March 2016, pp. 1859–1863.

[30] R. He, O. Renaudin, V. M. Kolmonen, K. Haneda, Z. Zhong, B. Ai, and C. Oestges, "A dynamic wideband directional channel model for vehicle-to-vehicle communications," *IEEE Transactions on Industrial Electronics*, vol. 62, no. 12, pp. 7870–7882, December 2015.

[31] A. Gehring, M. Steinbauer, I. Gaspard, and M. Grigat, "Empirical channel stationarity in urban environments," *4th European Personal Mobile Communications Conference (EPMCC)*, February 2001.

[32] G. Matz, "On non-WSSUS wireless fading channels," *IEEE Transactions on Wireless Communications*, vol. 4, no. 5, pp. 2465 – 2478, September 2005.

[33] A. Paier, T. Zemen, L. Bernadó, G. Matz, J. Karedal, N. Czink, C. Dumard, F. Tufvesson, A. F. Molisch, and C. F. Mecklenbräuker, "Non-WSSUS vehicular channel characterization in highway and urban scenarios at 5.2 GHz using the local scattering function," *International ITG Workshop on Smart Antennas (WSA)*, pp. 9 – 15, February 2008.

[34] L. Bernadó, T. Zemen, A. Paier, G. Matz, J. Karedal, N. Czink, C. Dumard, F. Tufvesson, M. Hagenauer, A. F. Molisch, and C. F. Mecklenbräuker, "Non-WSSUS vehicular channel characterization at 5.2 GHz - Spectral divergence and time-variant coherence parameters," *XXIX General Assembly of the International Union of Radio Science (URSI)*, August 2008.

[35] I. Viering, H. Hofstetter, and W. Utschick, "Validity of spatial covariance matrices over time and frequency," in *IEEE Global Communications Conference (GLOBECOM)*, vol. 1, November 2002, pp. 851–855 vol.1.

[36] T. J. Willink, "Wide-sense stationarity of mobile mimo radio channels," *IEEE Transactions on Vehicular Technology*, vol. 57, no. 2, pp. 704–714, March 2008.

[37] D. Umansky and M. Patzold, "Stationarity test for wireless communication channels," in *IEEE Global Communications Conference (GLOBECOM)*, November 2009, pp. 1–6.

[38] M. Herdin and E. Bonek, "A MIMO correlation matrix based for characterizing non-stationarity," *13th IST Mobile and Wireless Communications Summit, Lyon (France)*, June 2004.

[39] M. Herdin, N. Czink, H. Özcelik, and E. Bonek, "Correlation matrix distance, a meaningful measure for evaluation of non-stationary MIMO channels," *IEEE 61st Vehicular Technology Conference (VTC)*, vol. 1, pp. 136 – 140, June 2005.

[40] H. Xiao and A. G. Burr, "Full channel correlation matrix of a time-variant wideband spatial channel model," *IEEE International Symposium on Personal, Indoor and Mobile Radio Communications (PIMRC)*, pp. 1 – 5, September 2006.

[41] A. Ispas, C. Schneider, G. Ascheid, and R. Thom, "Analysis of the local quasi-stationarity of measured dual-polarized mimo channels," *IEEE Transactions on Vehicular Technology*, vol. 64, no. 8, pp. 3481–3493, August 2015.

[42] J. B. Andersen, T. S. Rappaport, and S. Yoshida, "Propagation measurements and models for wireless communications channels," *IEEE Communications Magazine*, vol. 33, no. 1, pp. 42–49, January 1995.

[43] E. Vinogradov, W. Joseph, and C. Oestges, "Measurement-based modeling of time-variant fading statistics in indoor peer-to-peer scenarios," *IEEE Transactions on Antennas and Propagation*, vol. 63, no. 5, pp. 2252–2263, May 2015.

[44] H. Suzuki, "A statistical model for urban radio propogation," *IEEE Transactions on Communications*, vol. 25, no. 7, pp. 673–680, July 1977.

[45] J. Salo, H. El-Sallabi, and P. Vainikainen, "Statistical analysis of the multiple scattering radio channel," *IEEE Transactions on Antennas and Propagation*, vol. 54, no. 11, pp. 3114–3124, November 2006.

[46] I. Gradshtein and I. Ryzhik, *Table of integrals, series, and products*. 7th ed. Academic Press, Inc.

[47] B. Bandemer, C. Oestges, N. Czink, and A. Paulraj, "Physically motivated fast-fading model for indoor peer-to-peer channels," *Electronics Letters*, vol. 45, no. 10, pp. 515–517, May 2009.

[48] M. Gan, N. Czink, P. Castiglione, C. Oestges, F. Tufvesson, and T. Zemen, "Modeling time-variant fast fading statistics of mobile peer-to-peer radio channels," *IEEE 73rd Vehicular Technology Conference (VTC Spring)*, pp. 1–5, May 2011.

[49] R. H. Clarke, "A statistical theory of mobile radio reception," *Bell Systems Technical Journal*, vol. 6, no. 47, p. 9571000, July 1968.

[50] W. C. Jakes, *Microwave Mobile Communications (An IEEE Press Classic Reissue)*. Wiley-IEEE Press, 1994.

[51] D.-S. Shiu, G. J. Foschini, M. J. Gans, and J. M. Kahn, "Fading correlation and its effect on the capacity of multielement antenna systems," *IEEE Transactions on Communications*, vol. 48, no. 3, pp. 502–513, March 2000.

[52] A. Abdi and M. Kaveh, "A space-time correlation model for multielement antenna systems in mobile fading channels," *IEEE Journal on Selected Areas in Communications*, vol. 20, no. 3, pp. 550–560, April 2002.

[53] A. S. Akki and F. Haber, "A statistical model of mobile-to-mobile land communication channel," *IEEE Transactions on Vehicular Technology*, vol. 35, no. 1, pp. 2–7, February 1986.

[54] A. Akki, "Statistical properties of mobile-to-mobile land communication channels," *IEEE Transactions on Vehicular Technology*, vol. 43, no. 4, pp. 826–831, November 1994.

[55] M. Pätzold, B. Hogstad, N. Youssef, and D. Kim, "A MIMO mobile-to-mobile channel model: Part I - The reference model," *IEEE International Symposium on Personal, Indoor and Mobile Radio Communications (PIMRC)*, pp. 573 – 578, September 2005.

[56] B. Hogstad, M. Pätzold, N. Youssef, and D. Kim, "A MIMO mobile-to-mobile channel model: Part II - The simulation model," *IEEE International Symposium on Personal, Indoor and Mobile Radio Communications (PIMRC)*, pp. 562 – 567, September 2005.

[57] G. J. Byers and F. Takawira, "Spatially and temporally correlated mimo channels: modeling and capacity analysis," *IEEE Transactions on Vehicular Technology*, vol. 53, no. 3, pp. 634–643, May 2004.

[58] A. Zajic and G. Stuber, "Space-time correlated mobile-to-mobile channels: Modelling and simulation," *IEEE Transactions on Vehicular Technology*, vol. 57, no. 2, pp. 715–726, March 2008.

[59] C. Patel, G. Stuber, and T. Pratt, "Simulation of Rayleigh-faded mobile-to-mobile communication channels," *IEEE Transactions on Communications*, vol. 53, no. 11, pp. 1876–1884, November 2005.

[60] Y. R. Zheng and C. Xiao, "Simulation models with correct statistical properties for rayleigh fading channels," *IEEE Transactions on Communications*, vol. 51, no. 6, pp. 920–928, June 2003.

[61] Y. Li and X. Huang, "The simulation of independent rayleigh faders," *IEEE Transactions on Communications*, vol. 50, no. 9, pp. 1503–1514, September 2002.

[62] J. Andersen, J. Nielsen, G. Pedersen, G. Bauch, and M. Herdin, "Room electromagnetics," *IEEE Antennas and Propagation Magazine*, vol. 49, no. 2, pp. 27–33, April 2007.

[63] H. Kuttruff, *Room acoustics*. London, New York: Spon Press, 2000. [Online]. Available: http://opac.inria.fr/record=b1097189

[64] J. Poutanen, J. Salmi, K. Haneda, V. Kolmonen, and P. Vainikainen, "Angular and shadowing characteristics of dense multipath components in indoor radio channels," *IEEE Transactions on Antennas and Propagation*, vol. 59, no. 1, pp. 245–253, January 2011.

[65] N. Czink, A. Richter, E. Bonek, J. P. Nuutinen, J. Ylitalo, ""Including Diffuse Multipath Parameters in MIMO Channel Models"," in *IEEE 66th Vehicular Technology Conference (VTC Fall)*, 2007.

[66] H. Kuttruff, *Room Acoustics*. Spon Press, 2000, London.

[67] A. Richter, and R. S. Thoma, "Joint maximum likelihood estimation of specular paths and distributed diffuse scattering," in *IEEE 61st Vehicular Technology Conference (VTC Spring), pages 11-15 vol. 1.*, 2005.

[68] J. B. Andersen, J. O. Nielsen, G. F. Pedersen, G. Bauch, and J. M. Herdin, "Room electromagnetics," *IEEE Antennas and Propagation Magazine*, vol. 49, no. 2, pp. 27–33, April 2007.

[69] J. B. Andersen, K. L. Chee, M. Jacob, G. F. Pedersen, and T. Kurner, "Reverberation and absorption in an aircraft cabin with the impact of passengers," *IEEE Transactions on Antennas and Propagation*, vol. 60, no. 5, pp. 2472–2480, May 2012.

[70] G. Steinbck, T. Pedersen, B. H. Fleury, W. Wang, and R. Raulefs, "Distance dependent model for the delay power spectrum of in-room radio channels," *IEEE Transactions on Antennas and Propagation*, vol. 61, no. 8, pp. 4327–4340, August 2013.

[71] J. Poutanen, J. Salmi, K. Haneda, V. M. Kolmonen, and P. Vainikainen, "Angular and shadowing characteristics of dense multipath components in indoor radio channels," *IEEE Transactions on Antennas and Propagation*, vol. 59, no. 1, pp. 245–253, January 2011.

[72] A. Bamba, W. Joseph, J. B. Andersen, E. Tanghe, G. Vermeeren, D. Plets, J. . Nielsen, and L. Martens, "Experimental assessment of specific absorption rate using room electromagnetics," *IEEE Transactions on Electromagnetic Compatibility*, vol. 54, no. 4, pp. 747–757, August 2012.

[73] O. Franek, J. B. Andersen, and G. F. Pedersen, "Diffuse scattering model of indoor wideband propagation," *IEEE Transactions on Antennas and Propagation*, vol. 59, no. 8, pp. 3006–3012, August 2011.

[74] C. L. Holloway, M. G. Cotton, and P. McKenna, "A model for predicting the power delay profile characteristics inside a room," *IEEE Transactions on Vehicular Technology*, vol. 48, no. 4, pp. 1110–1120, July 1999.

[75] A. Bamba, M. T. Martinez-Ingles, D. P. Gaillot, E. Tanghe, B. Hanssens, J. M. Molina-Garcia-Pardo, M. Lienard, L. Martens, and W. Joseph, "Experimental Investigation of Electromagnetic Reverberation Characteristics as a Function of UWB Frequencies," *IEEE Antennas and Wireless Propagation Letters*, vol. 14, pp. 859–862, 2015.

[76] J. I. Smith, "A computer generated multipath fading simulation for mobile radio," *IEEE Transactions on Vehicular Technology*, vol. 24, no. 3, pp. 39–40, August 1975.

[77] S. A. Fechtel, "A novel approach to modeling and efficient simulation of frequency-selective fading radio channels," *IEEE Journal on Selected Areas in Communications*, vol. 11, no. 3, pp. 422–431, April 1993.

[78] D. Young and N. Beaulieu, "The generation of correlated Rayleigh random variates by inverse discrete fourier transform," *IEEE Transactions on Communications*, vol. 48, no. 7, pp. 1114–1127, July 2000.

[79] Y. Ephraim and N. Merhav, "Hidden Markov processes," *IEEE Transactions on Information Theory*, vol. 48, no. 6, pp. 1518–1569, June 2002.

[80] J. A. Fessler and A. O. Hero, "Space-alternating generalized expectation-maximization algorithm," *IEEE Transactions on Signal Processing*, vol. 42, no. 10, pp. 2664–2677, October 1994.

[81] A. Richter, "Estimation of radio channel parameters: Models and algorithms," Ph.D. dissertation, Technischen Universitt Ilmenau, Ilmenau, Germany, May.

[82] B. Fleury, M. Tschudin, R. Heddergott, D. Dahlhaus, and K. Ingeman Pedersen, "Channel parameter estimation in mobile radio environments using the SAGE algorithm," *IEEE Journal on Selected Areas in Communications*, vol. 17, no. 3, pp. 434–450, March 1999.

[83] B. H. Fleury, P. Jourdan, and A. Stucki, "High-resolution channel parameter estimation for mimo applications using the sage algorithm," in *International Zurich Seminar on Broadband Communications, Access, Transmission, Networking*, 2002, pp. 30–1–30–9.

[84] J. D. Parsons, *The Mobile Radio Propagation Channel*. 2nd ed. London, U.K.:Wiley.

[85] "Propagation data and prediction models for the planning of indoor radiocommunication systems and radio local area networks in the frequency range 900 MHz to 100 GHz," *Recommendation ITU-R P.1238-4*, 2005.

[86] R. Kattenbach, "Statistical modeling of small-scale fading in directional radio channels," *IEEE Journal on Selected Areas in Communications*, vol. 20, no. 3, pp. 584–592, April 2002.

[87] F. Sanchez, A. Stephanides, N. Czink, and C. Oestges, "Fast fading characterization for indoor to indoor and outdoor to indoor channels," *IEEE Vehicular Technology Conference (VTC Fall)*, pp. 1–5, September 2011.

[88] S. Kullback and R. Leibler, "Annals of mathematical statistics," *International ITG Workshop on Smart Antennas (WSA)*, pp. 79 – 86, 1951.

[89] Y. Guo and B. C. Levy, "Robust mse equalizer design for mimo communication systems in the presence of model uncertainties," *IEEE Transactions on Signal Processing*, vol. 54, no. 5, pp. 1840–1852, May 2006.

[90] O. Renaudin, V. M. Kolmonen, P. Vainikainen, and C. Oestges, "Impact of the correlation matrix estimation accuracy on the computation of stationarity intervals," *Proceedings of the 4th European Conference on Antennas and Propagation (EuCAP)*.

[91] L. Nowosielski, M. Wnuk, J. M. Kelner, and C. Ziolkowski, "Modelling of the angle of arrival scattering using the von mises function for compatibility analysis," *Progress In Electromagnetics Research Symposium*, 2015.

[92] A. Zajic, G. Stuber, T. Pratt, and S. Nguyen, "Wideband MIMO Mobile-to-Mobile Channels: Geometry-Based Statistical Modeling With Experimental Verification," *IEEE Transactions on Vehicular Technology*, vol. 58, no. 2, pp. 517–534, February 2009.

[93] C. Fang, B. Allen, E. Liu, P. Karadimas, J. Zhang, A. A. Glazunov, and F. Tufvesson, "Indoor-indoor and indoor-outdoor propagation trial results at 2.6 ghz," in *Antennas and Propagation Conference (LAPC), 2012 Loughborough*, November 2012, pp. 1–4.

[94] J. Medbo and J. E. Berg, "Simple and accurate path loss modeling at 5 ghz in indoor environments with corridors," in *IEEE 52nd Vehicular Technology Conference (VTC Fall)*, vol. 1, 2000, pp. 30–36 vol.1.

[95] A. Abdi, J. A. Barger, and M. Kaveh, "A parametric model for the distribution of the angle of arrival and the associated correlation function and power spectrum at the mobile station," *IEEE Transactions on Vehicular Technology*, vol. 51, no. 3, pp. 425–434, May 2002.

[96] C. Zikowski, "Statistical model of the angular power distribution for wireless multipath environments," *IET Microwaves, Antennas Propagation*, vol. 9, no. 3, pp. 281–289, 2015.